THESIS FOR THE DEGREE OF DOCTOR OF PHILOSOPHY

High-Temperature Corrosion Properties of Chromia- and Alumina-Forming Alloys

TOMMY SAND

Department of Chemistry and Chemical Engineering

CHALMERS UNIVERSITY OF TECHNOLOGY

Gothenburg, Sweden 2022

High-temperature corrosion properties of chromia- and alumina-forming alloys

TOMMY SAND

ISBN 978-91-7905-662-9

Doktorsavhandlingar vid Chalmers Tekniska Högskola

Ny serie nr 5128

ISSN 0346-718X

Department of Chemistry and Chemical Engineering

Chalmers University of Technology

SE-412 96 Gothenburg

Sweden

Telephone + 46 (0)31-772 1000

Cover: Illustration of how different oxide scale microstructures are able to withstand: 1) evaporation of chromium-oxy-hydroxide; and 2) nitrogen permeability.

Printed by Chalmers Digitaltryck

Gothenburg, Sweden 2022

High-Temperature Corrosion Properties of Chromia- and Alumina-Forming Alloys

TOMMY SAND

Department of Chemistry and Chemical Engineering

Chalmers University of Technology

Abstract

Electricity production, transportation, and manufacturing industry are some of the largest sources of greenhouse gas emissions. In many cases, these processes are carried out at high temperature and energy efficiency is limited by material degradation, so-called 'high-temperature corrosion'. Understanding material degradation at high temperature is therefore crucial for making these processes more energy-efficient, thereby reducing greenhouse gas emissions. For an alloy to resist high-temperature corrosion, it must form a protective, slow-growing and adherent oxide scale on the metal surface. The type of oxide scale formed and how it evolves depend on the composition of the alloy and the operating conditions. Two common oxide scales formed on high-temperature alloys are chromia (Cr_2O_3) and alumina (Al_2O_3) scales. In this thesis, the formation and behaviour of these scales were studied. Focus was on two corrosion mechanisms: (i) how different scale microstructures are able to withstand the formation of volatile chromium-oxy-hydroxide; and (ii) how permeable the scales are to nitrogen. The study involved exposures of a wide variety of high-temperature alloys in environments with either high oxygen and water concentrations or high nitrogen concentration and low oxygen activity.

In environments with high concentrations of oxygen and water, chromia-forming Ni-base alloys suffered extensive volatilization of chromium-oxy-hydroxide. The resulting chromium depletion of the alloy triggered nickel oxidation which, in turn, caused a NiO layer to form on top of the chromia scale. The NiO 'cap-layer' reduced chromium evaporation rate, resulting in a secondary chromia scale being established at the oxide/metal interface. Cr-containing alloys forming alumina scales, showed a very limited evaporation rate of chromium-oxy-hydroxide. In the nitriding environment, the ability of the scale to prevent nitridation was studied. Gravimetric and GD-OES analyses showed that the presence of a chromia scale decreased the nitridation by 50-95%. A beneficial effect was observed for a two-layered scale that contained both chromia and silica, as this gave a nitridation reduction at the higher limit of the interval, i.e., 83-95%. Furthermore, the study showed that alumina scales without macro defects completely block the ingress of nitrogen.

Keywords: High-temperature corrosion, Oxidation, Nitridation, Cr-evaporation, Chromia scale, Alumina scale

LIST OF PUBLICATIONS

This thesis is based on the work contained in the following papers:

Paper I

T. Sand, C. Geers, Y. Cao, J.E. Svensson, L.G. Johansson. Effective reduction of chromium-oxy-hydroxide evaporation from Ni-base Alloy 690, Oxidation of Metals, Volume 92, Pages 259-279, 2019, https://doi.org/10.1007/s11085-019-09935-9

Paper II

T. Sand, A. Edgren, C. Geers, V. Asokan, J. Eklund, T. Helander, J.E. Svensson, L.G. Johansson. Exploring the effect of silicon on the high temperature corrosion of lean FeCrAl alloys in humid air, Oxidation of Metals, Volume 95, Pages 221-238, 2021, https://doi.org/10.1007/s11085-020-10019-2

Paper III

T. Sand, S. Bigdeli, M. Sattari, J. Andersson, M. Hättestrand, T. Helander, J. Eklund, J.E. Svensson, M. Halvarsson, L.G. Johansson. Efficacy of an external chromia layer in reducing nitridation of high temperature alloys. Corrosion Science, Volume 197, 2022, https://doi.org/10.1016/j.corsci.2021.110050

Paper IV

T. Sand, A. Rajagopal, M. Sattari, S. Bigdeli, M. Hättestrand, J.E. Svensson, M. Halvarsson, L.G. Johansson. Nitridation of austenitic alloys at 1100 °C. *Manuscript*

Paper V

T. Sand, J. Liske, T. Helander, J.E. Svensson, L.G. Johansson. A Comparison of the oxidation and nitridation properties of selected chromia- and alumina-forming alloys at 800 °C. *Accepted for publication in Oxidation of Metals*

Statement of authors' contributions

Paper I: I am the principal author. I performed all the experimental exposures and analyses using SEM and GIXRD. Yu Cao performed the XPS analyses.

Paper II: I am the principal author. I performed some of the experimental exposures and analyses using SEM and GIXRD. Aina Edgren performed most the experimental exposures and analyses using SEM and GIXRD. Vijayshankar Asokan performed the STEM analysis.

Paper III: I am the principal author. I performed all the experimental exposures and some analyses using SEM and XRD. Mohammad Sattari performed the STEM analysis, Jan Andersson performed the GD-OES analysis, Sedi Bigdeli performed the thermodynamic calculations, and Johan Eklund performed some of the XRD analysis.

Paper IV: I am the principal author. I performed all the experimental exposures and SEM analysis. Mohammad Sattari performed the STEM analysis, Anand Rajagopal performed EPMA analysis, and Sedi Bigdeli performed the thermodynamic calculations.

Paper V: I am the principal author. I performed all the experimental exposures and analyses using SEM and XRD.

ACKNOWLEDGEMENTS

I would like to express my sincere gratitude to everyone who made this thesis possible and helped me during this work.

I would like to thank my supervisors, Professor Lars-Gunnar Johansson and Professor Jan-Erik Svensson, for the opportunity to carry out the work of this thesis at Chalmers University of Technology and for all their help and guidance along the way. My sincere gratitude to Dr. Christine Geers for her support and help during this work. Thanks also to HTC, Vinnova, and Jernkontoret for support and funding and Kanthal AB, Sandvik AB, and Powercell AB for industrial collaborations. Many thanks to Dr. Mats Hättestrand, Bo Jönsson, Professor Mats Halvarsson and Dr. Thomas Helander for good cooperation and support.

Furthermore, I would like to thank the CMAL group for support with the microscopes, Yu Cao for the XPS measurements, Vijayshankar Asokan and Mohammad Sattari for the STEM examinations, Vratislav Langer and Michal Strach for help with the XRD, Sedi Bigdeli for the computer simulations, Andrea Fazi and Mattias Thuvander for the APT examination, Jan Andersson and Lennart Eriksson for GD-OES measurements, Anand Rajagopal for EPMA examinations, Esa Väänänen and Torbjörn Jönsson for all their technical support, and the administration staff at OOMK.

I am deeply grateful to everyone who helped me in the lab, to my Master's degree student Aina Edgren for all her great work, and to Johan Eklund for nice times while sharing the office.

I also want to thank everyone at the Department of Environmental Inorganic Chemistry for creating and fostering a fun and open working environment.

Finally, I would like to thank my family and friends for their support.

CONTENTS

1 INTRODUCTION

The global mean temperature started to increase in a non-normal behavioural pattern beginning in the 1960s, see Figure 1. The most recent report on climate change from the Intergovernmental panel on climate change (IPCC) states that this deviation and increase in mean temperature is due to human activities generating emissions of greenhouse gases (GHG) to the environment [1]. Since the industrial revolution in the middle of the 18th century, the atmospheric concentration of CO_2 has increased dramatically from the pre-historical maximum of 300 ppm to a level today that is above 410 ppm [2]. The change in mean temperature influences the climate on earth and increases the likelihood of extreme weather conditions, including droughts, floods, heat waves and hurricanes. The warmer temperature also leads to melting of arctic sea ice and glaciers, thereby raising sea levels. In order to limit the impact of climate change, dramatic reductions in CO_2 emissions levels are needed.

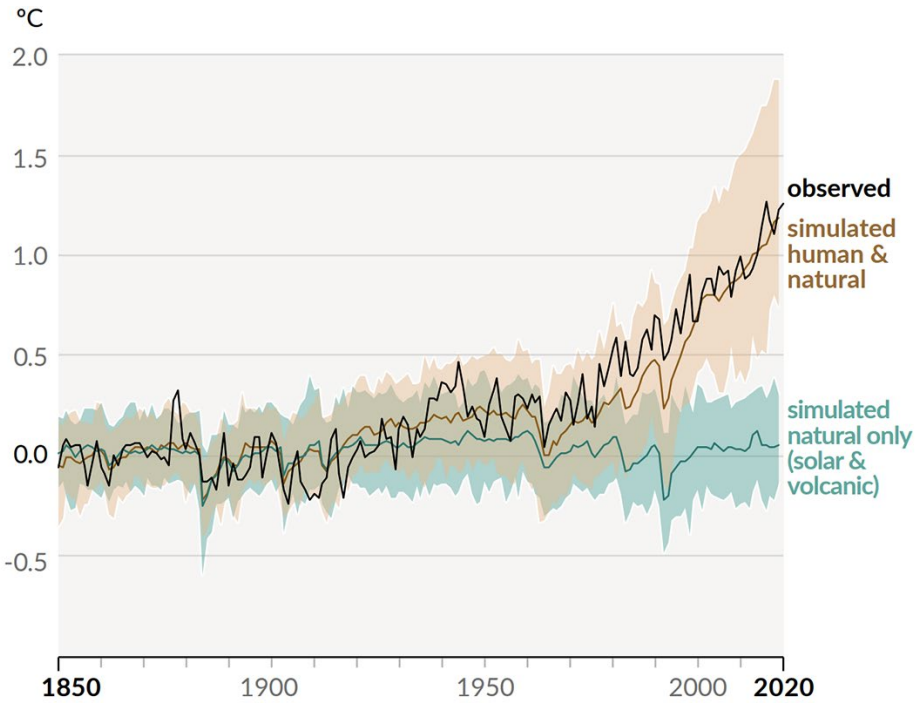

Figure 1 Deviation from normal global mean temperature from Year 1850 to Year 2020, with the observed deviation and a comparison of simulated scenarios with natural influences and human and natural influences [1].

The largest sources of CO_2 emissions are electricity and heat generation, transportation, and industrial and manufacturing processes [3]. The emissions from these sectors need to be significantly reduced to decelerate climate change. How this reduction is going to be achieved is not currently clear. Most likely it will involve changes in human behaviour, new political policies, and technological developments. In many cases, the technology is already available but market introduction is hampered by the high costs and limited efficiency of the technology. One example is the production of 'green' hydrogen to phase out 'grey' hydrogen

or coal in the production of fertilisers and steel. Another example is concentrated solar power (CSP), which converts thermal solar energy to electricity, for which the cost needs to be reduced to enable large-scale adoption by the market. Furthermore, technologies that have been around for a long time need to be improved and made more-efficient. In heat treatment, for example, more-efficient electrical heating could be developed in order to replace heating using fossil fuels. In biomass boilers the efficiency can be improved by increasing steam temperatures. The above-mentioned applications have one feature in common: they all rely on the use of heat-resistant alloys as components in for example, heating elements and heat exchangers. In many cases, the efficiencies of these processes are limited by the alloys available today, so the development of new improved materials could help to increase the efficiencies of these processes, thereby reducing the carbon foot-print. The most-important degradation mechanism affecting the life-time of these alloys is high-temperature corrosion.

For alloys to be able to resist high-temperature corrosion, it is crucial that a protective, slow-growing, and adherent oxide scale is formed on the metal surface. The type of oxide scale formed and the way in which it evolves depend on the composition of the alloy and the operating conditions, e.g., temperature and gas composition. Furthermore, the oxide scale is dynamic and can be subject to break-down by changes in the process conditions or depletion of the alloying elements in the metal.

Stainless steels and Ni-base alloys are alloyed with chromium in order to form a protective Cr-rich oxide scale. However, chromia (Cr_2O_3) is not a perfect barrier, as species such as nitrogen and carbon have been shown to penetrate the scale [4-6]. When these species enter the alloy and form precipitates with chromium it can reduce the life-time of the component, as the material becomes brittle and depleted in chromium. The chromia scale can also undergo degradation mechanisms like the formation of volatile chromium-oxy-hydroxide, $CrO_2(OH)_2$, when water is present together with oxygen in the environment [7-12]. Loss of chromium by evaporation can have detrimental effects on the alloy (owing to the depletion of chromium) and on the process (through the poisoning of critical components, such as catalysts [13]).

Another material group that is commonly used in high-temperature environments is the ferritic FeCrAl alloys, which rely on the formation of an alumina (Al_2O_3) surface oxide. The alumina scale is highly protective and superior to the chromia scale in many ways. For these alloys, the evaporation rate of $CrO_2(OH)_2$ is expected to be low due to the low content of chromium in the outer part of the scale. It is also known that alumina is highly protective against carbon and nitrogen ingress [14-16]. However, the slow formation of the alumina scale makes it difficult for the alloys to form protective alumina scales at relatively low temperatures, i.e., about 600 °C. The ability to form a protective scale can be improved by increasing the concentrations of aluminium and/or chromium in the alloy. However, this leads

to impairments related to weldability, formability, and structural stability. Recently, it has been reported that the addition of relatively small amounts of silicon (1-2 wt.%) improves the ability to form protective oxide scales, with fewer detrimental effects on the aforementioned properties of the material [17].

The purpose of this thesis is to increase our current understanding of oxide scale formation, evolution, and behaviours in environments that are relevant for high-temperature applications. A wide range of alloys has been studied, ranging from Fe-based stainless steels to chromia-forming Ni-base alloys to ferritic FeCrAl alloys with different concentrations of chromium, aluminium, and silicon. The thesis focuses primarily on the behaviours of these material groups in two different environments: 1) oxygen- and water- containing environments for which the formation of volatile $CrO_2(OH)_2$ is a concern; and 2) low oxygen activity, nitrogen-containing environments, for which nitridation is a concern.

Papers I and II are focused on the alloy behaviours in air with high concentrations of water vapour. Both papers provide new insights into how protective oxide scales form and evolve in these environments. **Papers III and IV** focus on the behaviours of different alloys in nitriding environments. **Paper III** explores, by changing the oxygen activity slightly, how effective chromia and alumina scales are at preventing nitrogen ingress into the alloys. In **Paper V**, alloys from all the material groups are compared directly at the same temperature and for the same time in different environments (including water-containing air and a nitriding environment).

2 APPLICATIONS

While there is no strict definition of the term 'high-temperature applications', in most cases it implies that the temperatures exceed 500 °C [18], (although exceptions to this exist, e.g., water walls in boilers). Above this temperature, reactions with the process environment can result in detrimental high-temperature corrosion and reduction of the life-times of the components. In the following sections, some of the most-relevant applications for the studied corrosion mechanisms, i.e., oxidation, Cr-evaporation and nitridation, are described.

2.1 COMBUSTION

Combustion of hydrocarbons to generate heat that is transferred to steam so as to drive a turbine is currently one of the most common ways to produce electricity, see Figure 2. The combustion of any matter that comprises hydrocarbons, such as coal, natural gas or biomass, generates H_2O and CO_2 according to Reaction 1, resulting in an oxygen- and water vapour-containing environment. The efficiency of the boiler depends on the temperature and pressure of the steam [19]. The most-advanced coal-fired power plants operate with steam temperatures of about 700 °C [20]. However, in the case of biomass-fired boilers, the corrosiveness of the biomass reduces the steam temperature to about 570 °C [21].

$$C_xH_y + zO_2 \rightarrow xCO_2 + \frac{y}{2}H_2O \qquad \text{Reaction 1}$$

To increase the efficiency of boilers, it is necessary to increase the steam temperature and pressure, thereby reducing the carbon footprint of the process. Increasing the steam temperature results in more corrosion of metallic components, such as the superheaters. During coal combustion, SO_2/SO_3 in the flue gas can result in hot corrosion [22] and during the combustion of biomass the higher concentration of H_2O and the presence of alkali chlorides increase the corrosion rates, mainly through chromate formation [23, 24], with the corrosion becoming more severe with increasing temperature. Another way to reduce the carbon footprint of combustion is to utilise carbon capture and storage (CCS), which involves collecting the CO_2 in the flue gas storing it underground. However, implementing CCS is associated with a high cost and reduced efficiency. By applying CCS to the combustion of biomass, negative CO_2-emissions can be achieved.

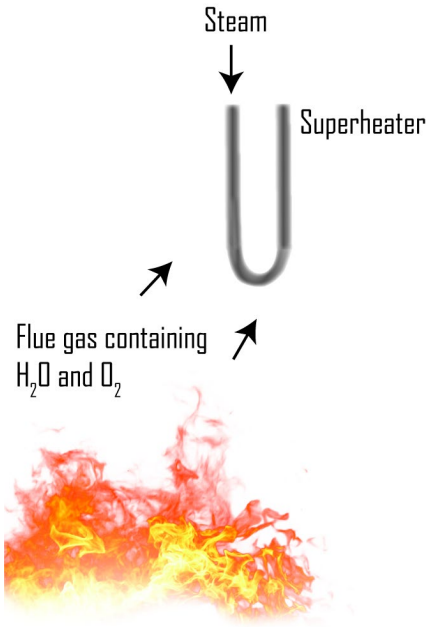

Figure 2 The underlying principle of the combustion of hydrocarbons, to generate superheated steam for electricity generation.

2.2 Reforming

Reforming is a chemical process in which hydrocarbons such as methane or diesel are converted to synthesis gas (or syngas), which comprises mainly CO and H_2, see Figure 3. Syngas has a high value because it can be combusted to generate heat and electricity or converted to almost-pure H_2 by applying the water-gas shift reaction (WGSR), see Reaction 2 [25]. Steam reforming, in which the methane is mixed with steam, is currently the most frequently used method for the production of hydrogen gas (grey hydrogen), which is used in the production of ammonia and for petroleum refining. Steam reforming is an endothermic reaction, requiring heat input from burners located inside a firebox. If reforming is performed with a mixture of oxygen and steam the reaction will instead be exothermal and the reformer can be built in a more compact design; this technology is termed autothermal reforming (ATR), see Reaction 3 for the reformation of methane [25]. The major draw-back of this process is that the H_2:CO ratio is lower than for steam reforming [25]. Following reformation, the reformate gas, which is at a temperature >800 °C, needs to be cooled to <300 °C for the WGSR to take place. Heat exchange to recover the heat from the reformate gas is usually carried out to make the process more energy-efficient. This heat can be used to warm up the steam or steam/air mixture before it is mixed with the hydrocarbon and fed into the reformer. A gas mixture that consists of H_2O and O_2 in the heat exchanger generates an environment that can cause the formation of $CrO_2(OH)_2$. If $CrO_2(OH)_2$ enters the reformer it can inhibit the catalysts used in the reformation process.

$$CO + H_2O \rightarrow H_2 + CO_2 \qquad \text{Reaction 2}$$

$$4CH_4 + 2H_2O + O_2 \rightarrow 10H_2 + 4CO \qquad \text{Reaction 3}$$

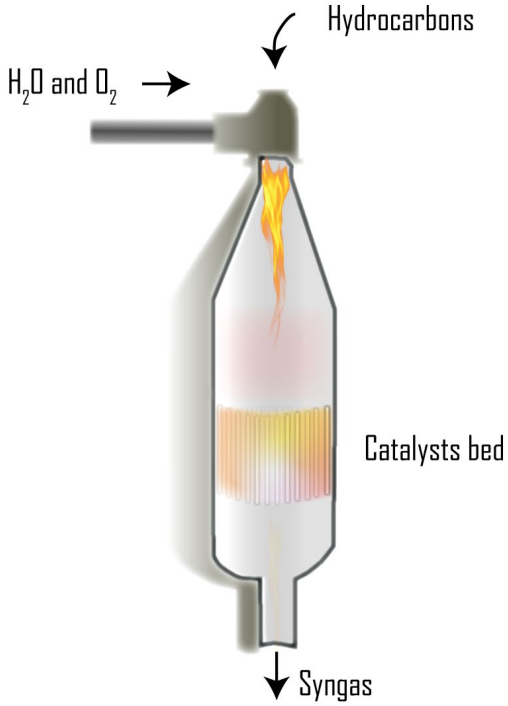

Figure 3 The principle of autothermal reforming of hydrocarbons to generate syngas.

2.3 FUEL CELLS

Fuel cells are electro-chemical devices that convert chemical energy to electricity and heat. The underlying principle of a fuel cell is that a fuel such as H_2 is fed into one side of an electrolyte and air is fed into the other side, see Figure 4. Ion movement through the electrolyte then leads to the transport of electrons through an external circuit, thereby creating an electrical current. The overall reaction results in the formation of water, see Reaction 4. There are different types of fuel cells, including proton exchange membrane fuel cells (PEMFCs) and solid oxide fuel cells (SOFCs). In PEMFCs, hydrogen is required as the fuel and the operating temperature is usually <100 °C [26]. In SOFCs, different fuels such as hydrogen or methane, can be used owing to their higher operating temperatures, in the range of 600-1000 °C [27]. The air side of an SOFC contains air at ambient humidity (up to 3 vol.% H_2O), which is an environment that promotes the formation of $CrO_2(OH)_2$ from stainless steel components, such as the interconnects in the fuel cells [28]. The formation of $CrO_2(OH)_2$ can result in so-called 'cathode poisoning' [29], as well as excessive degradation of the metallic components. SOFCs can also be operated in reverse mode, splitting water into H_2 and O_2 using electricity. This type of cell is called a solid oxide electrolyser cell (SOEC), and it can be used to

store energy chemically when electricity prices are low or to produce 'green' hydrogen if the source of electricity is renewable.

Fuel cells require surrounding components, i.e., heat exchangers, tubing, etc. These balance-of-plant (BoP) components may also be exposed to environments that contain high concentrations of H_2O and O_2, resulting in severe volatilisation of $CrO_2(OH)_2$ [30].

$$\frac{1}{2}O_2 + H_2 \rightarrow H_2O \qquad \text{Reaction 4}$$

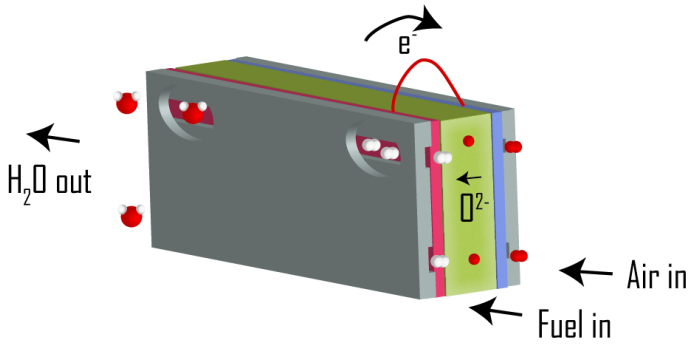

Figure 4 The principles of a fuel cell in which oxygen diffuses through an electrolyte reacting with hydrogen, resulting in an electrical current.

2.4 GASIFICATION

Gasification is the thermal conversion of hydrocarbons such as biomass into syngas, see Figure 5. The thermal conversion is carried out at high temperatures with a limited supply of oxygen/steam/CO_2 to avoid full oxidation, see Reaction 5. If syngas is produced with biomass as the feedstock, it can be converted into renewable fuels, such as Fischer-Tropsch diesel or other useful chemicals [31].

$$C_xH_y + xH_2O \rightarrow xCO + \frac{y+2x}{2}H_2 \qquad \text{Reaction 5}$$

Gasification is carried out at high temperature in a gasifier where the reaction occurs. The produced syngas can then be combusted in a boiler to generate electricity, or it can be cooled and be used as the raw material in chemical processes. It is also possible to convert the syngas to almost-pure hydrogen through the WGSR (see Reaction 2). In this case, the CO_2 can be captured and stored using CCS. Metallic components are usually used in equipment used for heat exchange, for example in a syngas cooler to recover the heat from the syngas during cooling. The harsh conditions with low activity of oxygen can result in high-temperature corrosion [32].

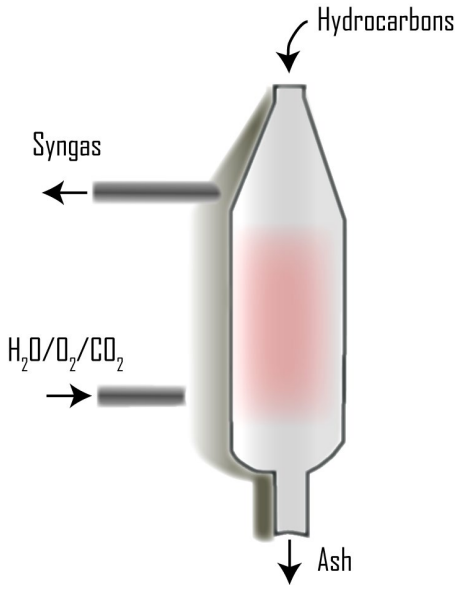

Figure 5 The principles of gasification. Hydrocarbons react with a limited supply of an oxidation medium to generate syngas.

2.5 HEAT TREATMENT

Heat treatment is a widely used process in order to influence the chemical and/or physical properties of materials. Examples of heat treatment include solution annealing of alloys, sintering of materials such as ceramics, and stress relieving of components. During heat treatment, the work piece is heated up in some way, for example by electric heating elements, see Figure 6. In many cases, heat treatment is performed in a low-oxygen atmosphere to avoid oxidation of the work piece. Heat treatment can be performed in vacuum, although this option is relatively expensive, slow and complicated. A more cost-efficient way is to use mixtures of N_2 and H_2, resulting in a low activity of O_2. In this environment, H_2 reacts with impurities of O_2 to form H_2O (according to Reaction 4), while N_2 is used as a balance owing to its low cost and relatively low reactivity. A mixture of 95% N_2 and 5% H_2 is favourable in terms-of safety, since leakage into the environment results in a H_2 concentration below 4%, which is the lower limit to sustain combustion in an oxygen containing gas mixture [33]. Measurement of the dew-point is a common method to monitor the moisture content in the heat treatment furnace, with a too-high dew-point leading to oxidation and too-low dew-point promoting nitridation [34]. Some examples of metallic components used as construction materials in heat treatment furnaces are: mesh belts, muffle tubes for wire annealing, furnace rollers, and heating elements.

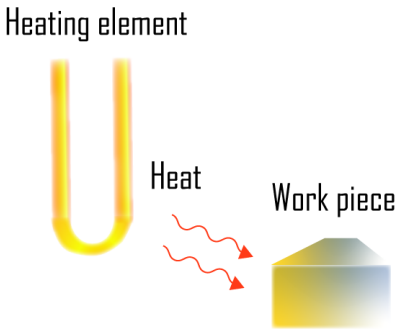

Figure 6 The principle of heat treatment whereby a work piece is heated using electrical heated heating elements.

3 HIGH-TEMPERATURE RESISTANT ALLOYS

Steels are alloys of iron and carbon. For steel to become a stainless steel, a chromium content >10.5 wt.% is needed [35]. Stainless steels are often used at high temperature because they can form a Cr-rich oxide scale. Another type of alloys commonly used for high-temperature applications are Ni-base alloys, in which the main component is nickel instead of iron. Stainless steels and Ni-base alloys are used at high temperatures for various purposes, such as heat exchange, transportation of media, or separation of media. The desired properties of these metallic alloys include: formability, weldability, good heat transfer, high strength, ductility, corrosion resistance, and relatively low prices. High-temperature alloys can be classified according to: alloy composition; properties; and structures; in different groups, such as:

- (Austenitic, ferritic, martensitic) stainless steels
- Ni-base alloys
- Co-base alloys
- Alumina-forming ferritic alloys
- Alumina-forming austenitic alloys

The alloy classes studied in this thesis are described below.

3.1 AUSTENITIC STAINLESS STEELS

Austenitic stainless steels are Fe-based alloys that are stabilised mainly with nickel, so as to make them austenitic. Sometimes, other austenite stabilising elements such as manganese and nitrogen, are added. Resistance to high-temperature corrosion is improved by increasing the chromium content and/or by adding silicon or reactive elements (REs). Some common austenitic stainless steels used for high-temperature applications are presented in Figure 7 (using the ASTM nomenclature). It should be noted that most of these alloys exist in different versions, which differ with respect to carbon concentration and grain size. For example, 304L is a low-carbon content version of 304, that is more resistant to certain corrosion mechanisms. The high-temperature version of 304, which is termed 304H, has large grains that increase creep strength. The two grades, 347 and 321, are stabilised with niobium and titanium, respectively, to avoid Cr-carbide precipitation, making them more resistant against intergranular corrosion. Characteristic properties of austenitic stainless steels are good ductility and good weldability.

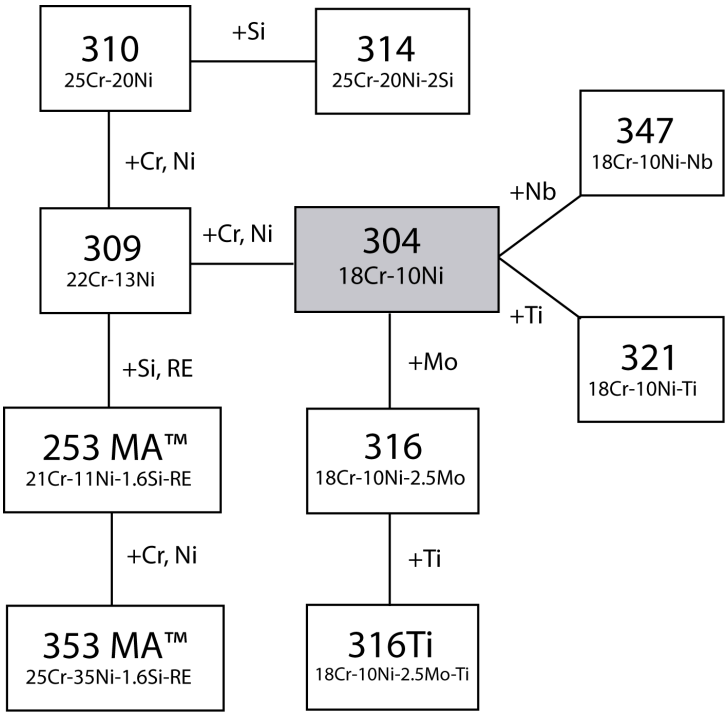

Figure 7 Map of some austenitic stainless steels commonly used for high-temperature applications, including their nominal chemical compositions. All the steels have iron as the base. 253 MA™ and 353 MA™ are trademarks owned by Outokumpu OY.

3.2 Ni-base alloys

Ni-base alloys are balanced by nickel, in contrast to the austenitic stainless steels in which iron is the main component. The nickel content is commonly >50 wt.%, however, some alloys with lower nickel content are still considered to belong to the Ni-base family, for example Alloy 800HT [36]. The base structure of Ni-base alloys is fully austenitic, and owing to the high nickel content good structure stability is maintained even with high concentrations of elements (e.g. molybdenum) that would otherwise impair structural stability. Ni-base alloys are alloyed with chromium, and in some cases aluminium, to improve their high-temperature corrosion resistance. At high temperatures, most Ni-base alloys form chromia scales, while a few (e.g. Alloy 214) have sufficient aluminium content to form an alumina scale. Most Ni-base alloys have high mechanical strength, which is achieved by precipitation hardening through the addition of titanium and aluminium to form secondary phases such as the γ'-phase ($Ni_3(Ti,Al)$), or by solution hardening using molybdenum, cobalt and tungsten [37, 38]. Ni-base alloys are used in various high-temperature applications, including turbine components and superheaters in power boilers. The high nickel content and the often advanced manufacturing route make these alloys relatively expensive to produce compared to austenitic stainless steels. Figure 8 shows a map of the most common Ni-base alloys used for corrosion protection, together with their nominal compositions.

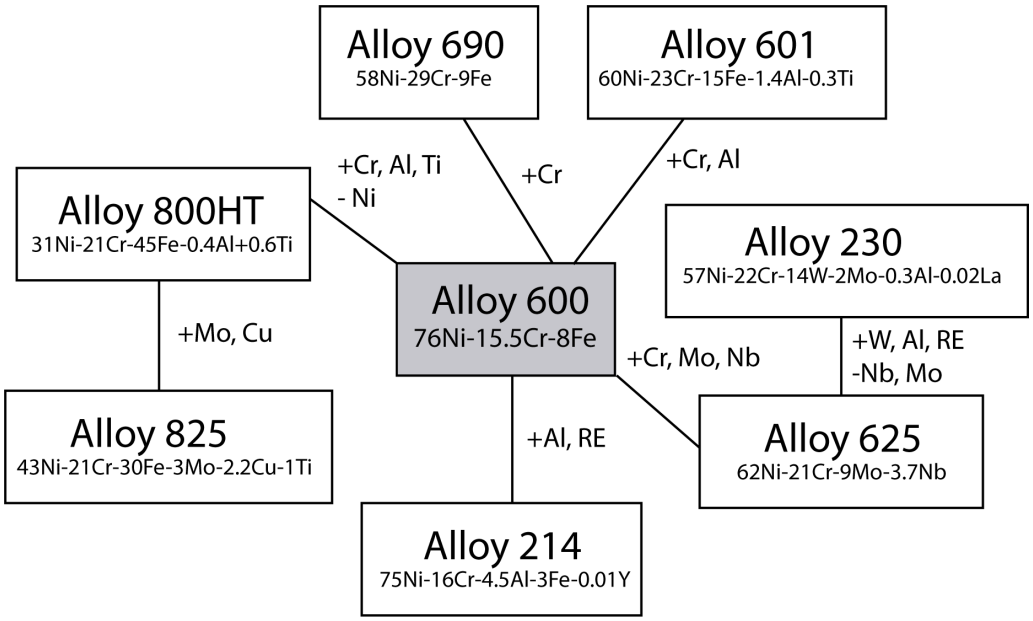

Figure 8 Map of some of the most common Ni-base alloys used for high-temperature service.

3.3 ALUMINA-FORMING FERRITIC ALLOYS

Alumina-forming ferritic alloys are Fe-based alloys that contain aluminium and chromium. The characteristic properties of these alloys are: very good oxidation resistance, low thermal expansion, high thermal conductivity, relatively poor weldability, low ductility at room temperature, and poor structural stability. The aluminium is added so that the alloys can form an external alumina scale. In the binary Al-Fe system, the aluminium content needs to be approximately 7 wt.% for the alloy to form an external alumina scale [39]. As this would make the alloy very brittle, a third element in form of chromium is added so that the aluminium content can be reduced to about 3-4 wt.% Al for a Fe-14% Cr alloy [40]. This beneficial effect of chromium is called the third-element effect (TEE). It implies that the chromium facilitates the formation of an initial Cr-rich oxide with protective properties before a continuous alumina scale can be established. Since a rather high chromium content is needed for the TEE, alumina-forming ferritic alloys are sometimes susceptible for precipitation of secondary phases, such as α', Cr-carbonitrides, and σ-phase at intermediate temperatures of 500-800 °C [41, 42]. The formation of α', so-called '475 °C-embrittlement' involves the separation of the ferritic phase into one Cr-rich phase and one Fe-rich phase due to a miscibility gap in the Fe-Cr system. To avoid this, the chromium content should be below 10-15 wt.% in a FeCrAl alloy that contains 4 wt.% aluminium, see Figure 9 [43]. However, a composition of 10-15 wt.% chromium and 4 wt.% aluminium is considered to be at the limit for alumina scale formation at relatively low temperatures, i.e., 600 °C [44]. One way to retain the ability to form a protective alumina with a lower chromium content is to add small amounts of silicon [17]. This idea is not new: using silicon to increase the corrosion resistance of an Fe-Al alloy in dry air

has been described previously [45]. Silicon is reported to influence the diffusion properties of aluminium and iron and, thereby, increase the ability to form a protective alumina scale [46].

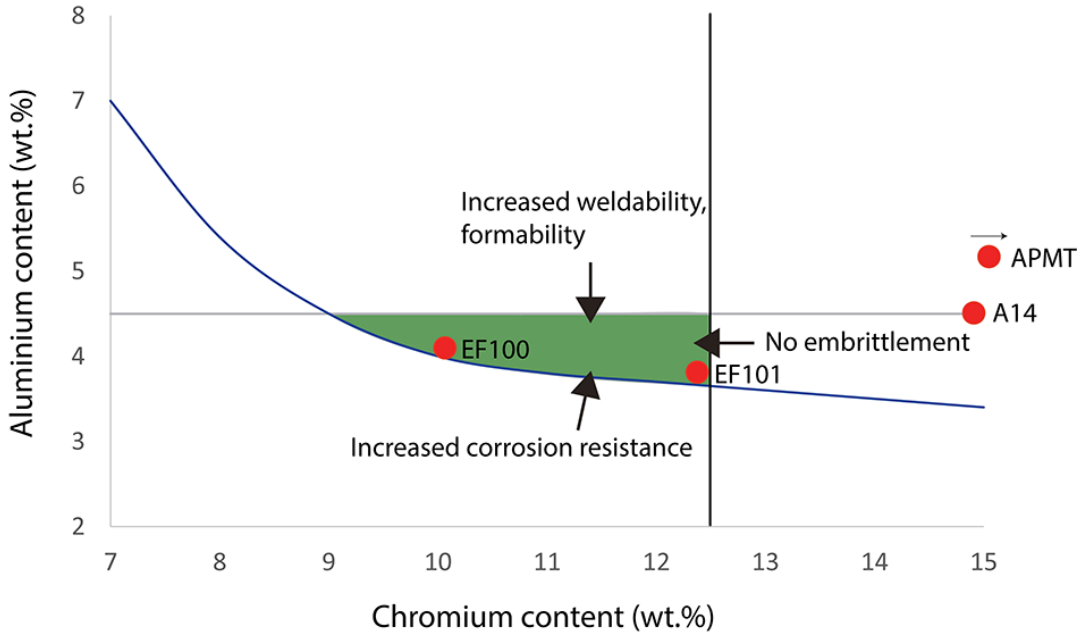

Figure 9 Schematic diagram showing how the properties of FeCrAl alloys are influenced by their chromium and aluminium content at intermediate temperatures of about 600 °C. The green area indicates where corrosion resistance is sufficient with maintained weldability and without the formation of brittle phases. The alloys tested in this thesis are marked with red circles.

Another group of elements typically used in alumina-forming alloys are the REs. Similar to chromia-forming alloys an increased oxide adherence and reduced oxidation rate is observed with even small additions of RE, see Section 3.4 below for a more detailed description of the RE-effect.

When the aluminium and/or chromium levels are borderline (in terms of the formation of a continuous alumina scale) Fe-oxide rich nodules can form, especially in conjunction with RE-particles [47-49]. These Fe-oxide nodules do not grow over time, due to the establishment of an alumina scale at the nodule/metal interface [50].

3.4 The reactive element effect

REs such as cerium, yttrium, zirconium, tantalum, hafnium, and lanthanum are known to increase the oxidation resistance at high temperature of both chromia- and alumina-forming alloys [51-53]. Thus, additions in the 10-1000 ppm range have been shown to improve the adherence and reduce the growth rate of the formed scales. The mechanisms behind the RE effect are not fully understood, although several hypotheses have been proposed, some of which are presented below.

- Altered ion diffusivity through the scale, whereby the outward diffusion of cations is reduced while the inward diffusion of oxide ions is unaffected, leading to a more-inward growing oxide [54].
- Oxidation results in RE-rich oxide nodules, which are incorporated into the scale. The nodules create a pegging-effect of the oxide to the substrate and increase adherence [51].
- The REs act as getters of detrimental elements, e.g., sulphur, thereby reducing the levels of contamination elements in the metal, which would otherwise interact and reduce the adherence of the scale [55, 56].

In a recent study performed with a FeCrAl alloy at low activity of O_2 with traces of H_2O as the only oxidant, it was shown that OH^- was transported through the alumina scale in Y-oxide decorated grain boundaries. The Y-oxide decoration helped to keep the inward transportation pathway open, resulting in the rapid formation of a protective alumina layer [57]. The same study also reported that the oxidation properties of FeCrAl alloys are harmed by the presence of large RE-rich particles in the alloy.

3.5 ALLOYS INVESTIGATED

In this thesis, alloys from the three alloy groups: austenitic stainless steels, Ni-base alloys, and alumina-forming ferritic alloys, were investigated, for the chemical compositions of all the alloys, see Table 1. Three different austenitic stainless steels were included, 310H, 253 MA and 353 MA, the main difference between these alloys is related to the chromium and nickel contents. In addition, the two 'MA'-steels contain silicon, nitrogen, and REs. Three different Ni-base alloys, Alloy 800HT, Alloy 600 and Alloy 690, were studied, Alloy 690 has a high concentration of chromium and Alloy 800HT has a relatively low concentration of nickel. Four different ferritic alumina-forming FeCrAl alloys were included. APMT contains high concentrations of chromium and aluminium, while EF100 and EF101 have lower concentrations of both and are considered to be resistant to the formation of phases that cause embrittlement, with 'EF' standing for 'Embrittlement Free'. Alkrothal 14 (A14) is an intermediate case.

Table 1 Chemical compositions (in wt.%) of the alloys investigated. The balance is iron in all cases.

Alloy	*Cr*	*Al*	*Ni*	*C*	*Si*	*Mn*	*Other*
310H	24.3		20.2	0.05	0.34	1.24	
253 MA	21.0		10.8	0.07	1.52	0.67	N=0.16, Ce
353 MA	25.7		34.9	0.07	1.39	1.68	N=0.17, Ce
A800HT	20.3	0.46	30.3	0.06	0.44	0.50	Ti=0.51
A600	16.7	0.14	72.6	0.01	0.31	0.19	Ti=0.33
A690	29.6		60.1	0.02	0.19	0.29	Ti=0.28
A14	14.8	4.4		0.03	0.33	0.22	RE
EF101 (A197)	12.4	3.7		0.02	1.25	0.10	RE
EF100 (A198)	10.1	4.0		0.02	0.3	0.2	RE
APMT	21.3	4.9		0.03	0.4	0.2	Mo, RE

4 Basic theory of metal oxidation

4.1 Metal oxidation

Metals that are subjected to a non-inert environment will interact with that environment, resulting in chemical reactions that can interfere with the intended application of the metal. In air, all metals (with the exception of gold) react with oxygen, forming metal oxides according to Reaction 6 [58]. The structure and properties of the oxide depend on different factors, such as the type of metal, environment, temperature, pressure, and time. Since the oxide is formed on the metal surface, it tends to form a barrier between the metal and the environment, such that further reactions require the transport of reactants across this barrier. In many cases, the oxide forms a continuous and adherent layer on the metal. At high temperatures, this oxide is commonly referred to as an 'oxide scale'. The initial formation of the oxide scale can, in simplistic terms, be described as involving three steps [58], as illustrated in Figure 10. The first step involves the adsorption of O_2 to the metal, the second step entails nucleation and growth of the oxide, and the third and final step is scale growth.

$$xM + \frac{y}{2}O_2 \rightleftarrows M_xO_y \qquad \text{Reaction 6}$$

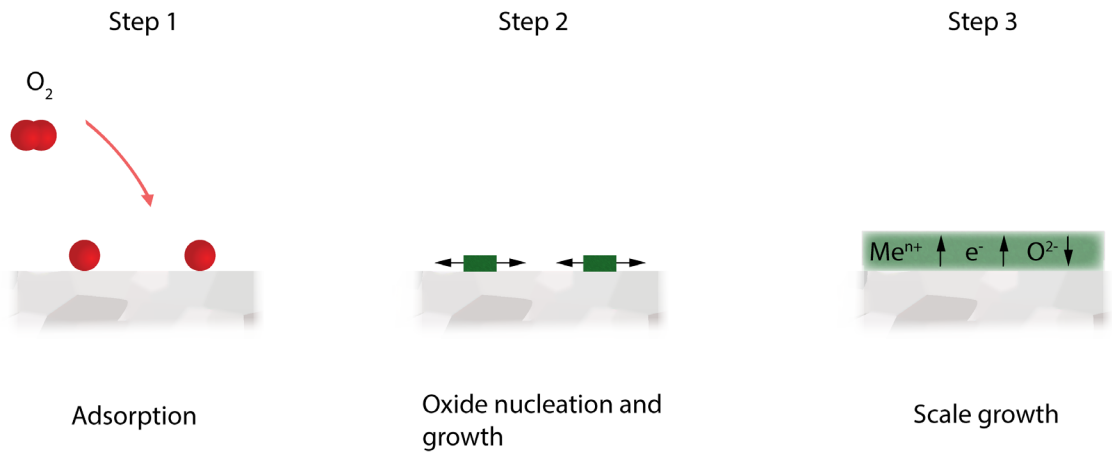

Figure 10 Schematic showing the formation of an oxide scale. Step 1, adsorption of oxygen; Step 2 oxide nucleation and growth; and Step 3, scale growth. Adapted from [58].

4.2 Thermodynamics

Whether or not the formation of a metal oxide is spontaneous depends on the temperature and oxygen activity in the environment. From the reaction for the formation of the metal oxide (Reaction 6), it is clear that the metal oxide can form and that the metal oxide can dissociate to a metal depending on the oxygen activity. The Gibbs free energy of a system at constant temperature and pressure is defined according to Equation 1:

$$G = H - T \cdot S \qquad \text{Equation 1}$$

where G is the Gibbs free energy, H is enthalpy, T is temperature and S is entropy [59].

The Gibbs free energy can be used to determine whether or not a reaction is spontaneous. In order for the reaction to be spontaneous, the change in Gibbs free energy has to be <0. The Gibbs free energy for Reaction 6 is expressed by Equation 2:

$$\Delta G = \Delta G^0 + RTlnK_{eq} = \Delta G^0 + RTln\frac{a_{(M_xO_y)(s)}}{a_{M(s)}^{x} a_{O_2(g)}^{\frac{y}{2}}} \qquad \text{Equation 2}$$

where ΔG^0 is the standard Gibbs free energy, R is the universal gas constant, K_{eq} is the equilibrium constant for the reaction; and a represents the activities of the corresponding reactants.

Since the activity a of a pure substance (M(s) and M_xO_y(s)) is 1, the only two variables are the temperature and the activity of oxygen, which can be conveniently presented in a so-called Ellingham/Richardson-diagram, see Figure 11. From this diagram, it is possible to determine the oxygen partial pressure above which a metal oxide is thermodynamically stable, the so-called 'dissociation pressure'. Below the dissociation pressure, the metal oxide is thermodynamically unstable and any metal oxide will tend to decompose to the pure metal and oxygen with time.

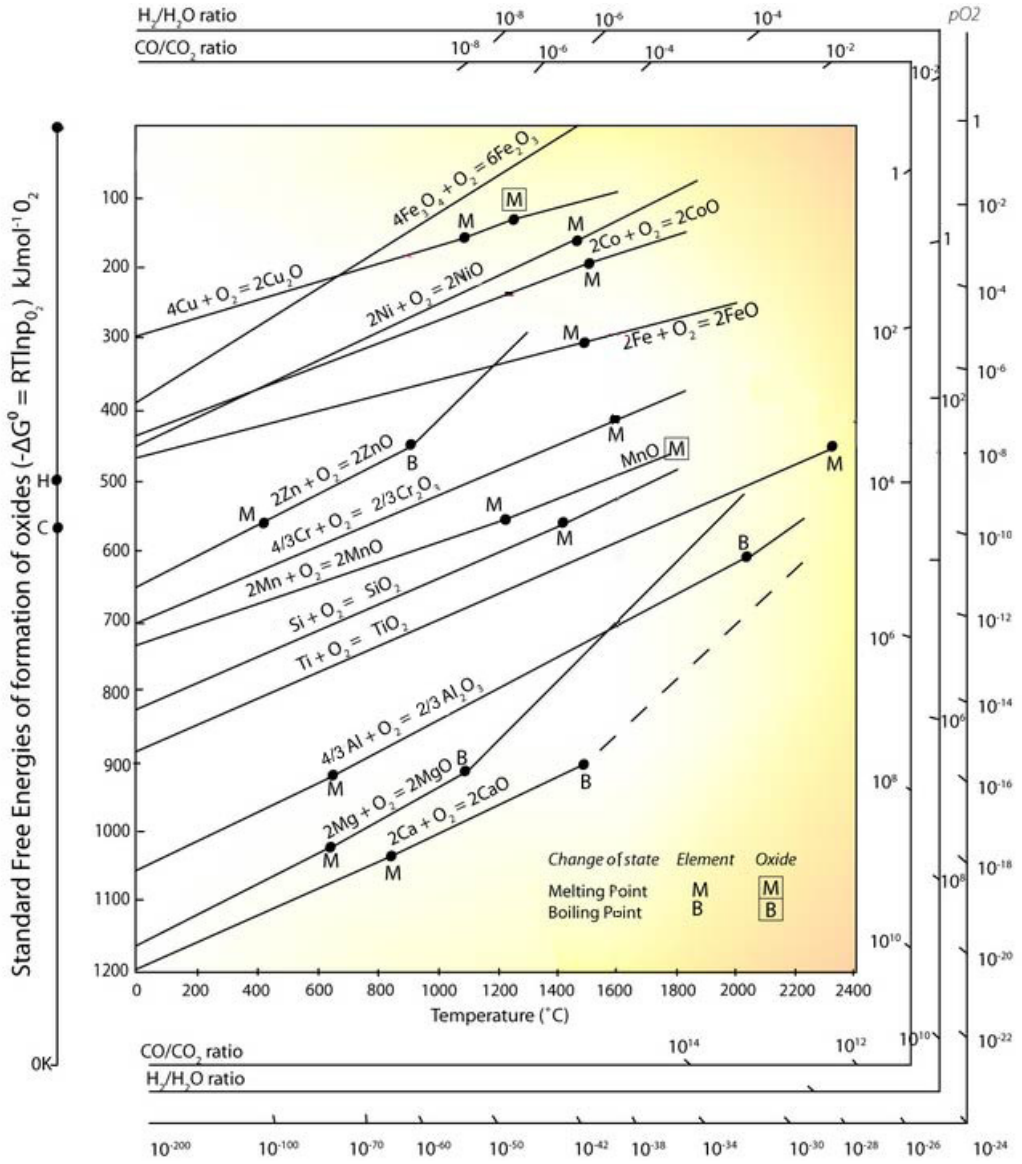

Figure 11 Ellingham/Richardson diagram for some of the most common metals/metal oxides [60].

4.3 KINETICS

The rate at which an oxide scale grows depends on various processes, such as solid-state diffusion through the scale, redox-reactions of the reactants at the scale/gas and scale/metal interfaces, and the properties of the scale. When diffusion through the scale is rapid, the growth rate is dictated by the slowest redox-reaction in the system, which usually is the reaction at the scale/gas interface [18]. In this case, the scale grows at a linear rate and can be described by Equation 3:

$$x = k_l t \qquad \text{Equation 3}$$

where x is the scale thickness, t is time, and k_l is the linear rate constant. This phenomenon is typically observed in cases with extremely thin scales, as well as in cases with porous and defect-rich scales.

If scale growth is governed by solid-state diffusion through the scale, the flux of ions/molecules/electrons needs to be considered. A model that describe this phenomenon was first presented by Wagner [61], who used Fick's first law together with electron diffusion mechanisms to explain how an oxide scale grows at a parabolic rate. In principle, the model describes how gradients of the oxygen partial pressure across the scale, together with the change in free energy for the metal oxide formation, generate a driving energy for the ions to "jump" between defects in the lattice, to allow metal oxide formation. As the scale grows, the driving energy declines and the growth rate decreases. This is an idealised model that requires that certain criteria are met, such as thermodynamic equilibrium at the interfaces and inside the scale, steady-state conditions at the interfaces, and homogeneity of the phases. These criteria are, in fact, often not fulfilled in practical instances of high-temperature corrosion. Nevertheless, the model is widely used to describe the diffusion-controlled growth of an oxide scale. The parabolic growth rate is described by Equation 4:

$$x^2 = K_p t + C \qquad \text{Equation 4}$$

where K_p is the parabolic rate constant and C is the integration constant.

In reality, an oxide scale is complex and dynamic. This means that the diffusion mechanisms change over time, and this is especially true for complex alloy systems that contain several alloying elements that can form oxides. The oxygen activity changes locally within the scale and the activity of the alloying element in the alloy changes with time.

'Break-away' oxidation describes a case where oxide growth is initially parabolic but following break-down of the oxide scale, a linear oxidation behaviour emerges. In the case of Cr-rich oxide scales, this behaviour is often due to chromium depletion of the oxide and/or the metal, leading to break-down of the protective Cr-rich oxide scale [62, 63]. At this stage, rapid growth of Fe-oxides occurs, leading to a dramatic increase in the oxidation rate. Depletion of chromium can also occur in Ni-base alloys, with the consequence that the nickel starts to oxidise. However, this does not trigger linear oxidation kinetics and it is not defined as 'break-away' oxidation. Huczkowski et al. [64] have instead labelled this as 'critical Cr-depletion'.

4.4 Oxide microstructure and properties

The bonds in oxide crystals can range from being highly covalent (SiO_2) to highly ionic (Cr_2O_3). The nature of the bonds and the defect morphology of the oxide influence the properties of the scale, e.g., the transport of ion/atoms through the scale, which determines how protective the scale is. Transport through a covalent oxide such as SiO_2 mainly involves the transport of oxygen atoms through the covalent network [65, 66]. In an oxidising environment, the growth of SiO_2 occurs mainly through inward oxygen diffusion.

In ionic oxides, diffusion occurs by defects in the lattice. The defects can be either stoichiometric or non-stoichiometric. Stoichiometric defects do not influence the chemical composition of the oxide, and are called Schottky or Frenkel defect. A Schottky defect entails the incorporation of vacancies into the lattice, where both a cation and an anion are missing. A Frenkel defect involves the incorporation of a cation interstitial ion, which is balanced by a cation vacancy. The presence of these defects enables vacancy and interstitial movements within the lattice, while the stoichiometry and electron neutrality are maintained. In contrast, a non-stoichiometric defect generates oxides that deviate from the stoichiometry through either oxygen excess/deficiency or metal excess/deficiency, e.g., $Fe_{1-x}O$ [67].

Oxide scales are generally polycrystalline, which means that a significant number of defect-rich grain boundaries exists in the oxide scale. In fact, the main diffusion pathways at temperatures <900 °C are considered to be along these grain boundaries, which are referred to as short-circuit diffusion paths through the scale [68]. In amorphous oxides such as SiO_2, there are no grain boundaries that allow short-circuit diffusion paths.

Oxide scales can also contain macro defects, such as pores, void and cracks, which means that rapid molecular transportation is possible. [18]. Factors that induce these defects include: stresses in the oxide; contaminants in the metal; and a scale that is growing too rapidly.

Alloys can form different types of oxide structures depending on the alloy composition, temperature, etc. The main oxide structures observed in this thesis are summarised below. The oxidation rates for some of these oxides are presented in Figure 12.

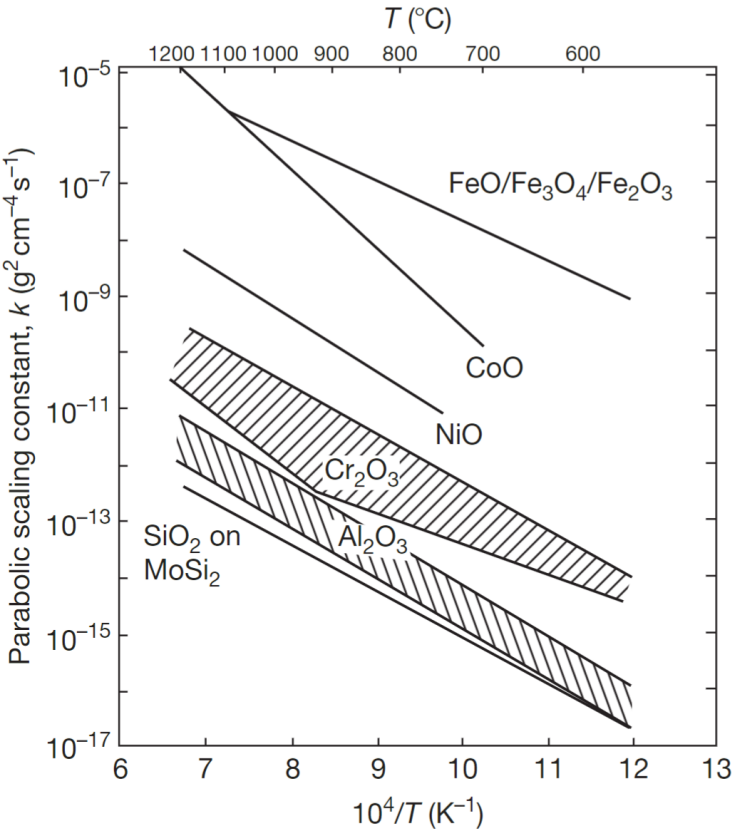

Figure 12 Parabolic oxidation rate plotted as k_p as a function of temperature for some of the most common oxide scales. Reproduced with permission from Gleeson, B. Corrosion and Environmental Degradation, V. II: Materials Science and Technology Series 19, p. 174-228, 2000, Copyright Wiley-VCH Gmbh [69].

4.4.1 Iron oxide scales

Steel, being an alloy of iron and carbon, forms Fe-oxides when exposed to high temperatures. These Fe-oxides can also form if chromium and aluminium are depleted in an alloy. There are three different types of Fe-oxides formed under normal conditions: wüstite $Fe_{1-x}O$; magnetite Fe_3O_4; and hematite Fe_2O_3. Wüstite has the rock-salt structure with a low degree of stoichiometry, leading to fast diffusion through the oxide and high growth rates. The formation of wüstite is spontaneous at temperatures >570 °C. Magnetite has the inverse spinel structure and is slower-growing compared to wüstite. The Fe-oxide with the lowest growth rate is hematite, which has the corundum structure. Hematite can be considered to be semi-protective due to its slower growth rate compared to the other iron oxides.

If iron is oxidised at temperatures >570 °C, all three iron oxides are stable and the oxide will consist of three layers. According to the Ellingham diagram in Figure 11, the oxide that is stable at the lowest oxygen partial pressure (wüstite) forms the layer closest to the interface and the oxide that is stable at the highest oxygen partial pressure (hematite) forms a layer closest to the environment, which means that magnetite forms the middle layer in the Fe-oxide scale.

Examinations of the proportions of the different layers reveal that the oxide consists mainly of wüstite, and magnetite with only a thin outer layer of hematite [70, 71].

4.4.2 CHROMIA SCALES

If the alloy contains a sufficient amount of chromium, it can form a chromia (Cr_2O_3) scale. Chromia has the hexagonal corundum structure, with the chromium ions occupying octahedral holes in the oxide lattice [72]. Chromia is close to stoichiometric, and chromia scales grow much more slowly than iron oxide scales. Chromia is iso-structural with hematite (Fe_2O_3) and the two oxides are mutually soluble. Therefore, Cr-containing Fe-base alloys often form scales that consist of a solid solution of Fe^{3+} in chromia, $Cr_{2-x}Fe_xO_3$, rather than pure Cr_2O_3 [73]. It has been observed that the oxygen partial pressure influences the defect structure of a Cr_2O_3-oxide. At low oxygen partial pressure, the oxide behaves as an n-type semi-conductor, whereas at high oxygen partial pressure it behaves as a p-type semi-conductor [74-76].

4.4.3 M_3O_4 (SPINEL) SCALES

Spinel oxides consist of cations ions, such as $Fe^{2+,3+}$, $Mn^{2+,3+}$, Ni^{2+} and Cr^{3+}, which occupy the tetrahedral and octahedral sites in a cubic closed-packed array of oxide ions. There are two types of spinel oxide: (i) the 'normal' spinel, in which M^{3+} occupies half of the octahedral sites and M^{2+} occupies every eighth tetrahedral site ($FeCr_2O_4$); and (ii) the 'inverse' spinel structure, in which every eighth tetrahedral site is occupied by an M^{3+} and the octahedral sites are split between M^{2+} and M^{3+}, e.g., Fe_3O_4 [58]. In general, spinel oxides have rather poorly protective properties compared to chromia, although the diffusion rate in a spinel depends on its elemental composition.

4.4.4 NICKEL OXIDE SCALES

NiO has the rock salt structure, in which the oxide ions form a cubic close-packed array with the Ni-ions in octahedral interstitials [58]. Oxidation of nickel is slower than oxidation of iron, which is an advantage that Ni-base alloys have over Fe-base alloys [77]. It should also be noted that the reaction between NiO and Cr_2O_3 to form $NiCr_2O_4$ is spontaneous [78].

4.4.5 SILICA SCALES

Silica scales, SiO_2, can form on Si-containing alloys and on Si-containing ceramics such as $MoSi_2$ [79]. The silica scale exhibits a low growth rate as seen in Figure 12. However, at low aO_2, silica forms SiO(g), which makes silica-forming materials unsuitable for use in environments with low O_2 activity [18]. In chromia-forming alloys, silicon is usually added at a relatively low concentration, to avoid making the alloy brittle. Silica forms a layer beneath the chromia layer and is usually amorphous [80-82]. However, the formation of a continuous silica layer is sluggish, taking 300-1200 hours at 825 °C [83, 84]. At a temperatures of 1100 °C crystalline, silica has been observed in the forms of cristobalite and tridymite [85].

4.4.6 ALUMINA SCALES

Similar to Cr_2O_3, α-Al_2O_3 has a corundum structure. However, α-Al_2O_3 is more stoichiometric and generally contains fewer defects, resulting in a lower growth rate compared to chromia. Inward diffusion of oxygen through short-circuit grain boundaries is the main contribution of ion diffusion across an α-alumina [86, 87]. Since the nucleation of α-alumina is rather slow, different transient Al_2O_3 phases are normally formed at temperatures <1000 °C [88]. These 'transient aluminas' transform to α-Al_2O_3 given sufficient time and sufficiently high temperature. The transient alumina phases, γ-alumina, θ-alumina, δ-alumina and κ-alumina, exhibit much faster ion diffusion than α-alumina and, consequently exhibit faster growth rates. It has been observed in previous studies that these transient alumina phases grow outwards by metallic cation diffusion [89].

5 Corrosion by water vapour

Water vapour is a corrosive species at high temperatures. The effects of water vapour have been studied extensively, and water has been reported to accelerate corrosion both at high oxygen activity and in environments where oxygen activity is low [7, 8, 63, 90-106]. The review presented by Saunders et al. [107] provides good coverage of this topic. Since water vapour is present in many industrial processes, increased understanding of how water vapour influences the growth of oxide layers on alloys is of the utmost importance.

5.1 Chromium evaporation

When a Cr-rich oxide scale is exposed to an environment that contains O_2 or O_2/H_2O at high temperatures, chemical reactions occur, that result in the formation of gaseous species containing hexavalent chromium, see Figure 13, and Reactions 7 and 8. This is commonly referred to as 'chromium evaporation' and it depends on several factors, including temperature, the partial pressures of O_2 and H_2O, gas velocity and scale structure. Extensive theoretical and experimental investigations have been conducted to determine the equilibrium partial pressure of CrO_3 and $CrO_2(OH)_2$ over Cr_2O_3 at different temperatures and for different gas compositions [9, 10]. In ambient air (about 1% H_2O (g)) at temperatures <900 °C, the main volatile compound is $CrO_2(OH)_2$. CrO_3 can be neglected at temperatures <800 °C.

$$Cr_2O_3(s) + 1.5\,O_2 \leftrightarrows 2CrO_3(g) \qquad \text{Reaction 7}$$

$$Cr_2O_3(s) + 2H_2O + 1.5\,O_2 \leftrightarrows 2CrO_2(OH)_2(g) \qquad \text{Reaction 8}$$

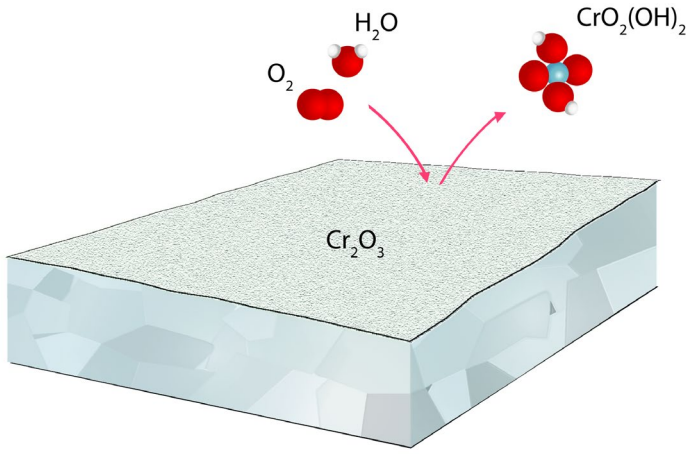

Figure 13 Schematic illustration of chromium evaporation from a chromia scale. Water vapour and oxygen react with the chromia scale, forming $CrO_2(OH)_2$.

The formation of $CrO_2(OH)_2$ from a chromia scale involves the oxidation of Cr^{3+} to the hexavalent state by O_2, followed by hydrolysis of the Cr(III)-O-Cr(VI) bonds by H_2O [108].

Increasing the partial pressures of H_2O and O_2 increases the evaporation rate, since the equilibrium of Reaction 8 is pushed towards $CrO_2(OH)_2$. In an environment that contains H_2O and O_2, the maximum equilibrium vapour pressure occurs when the fraction of H_2O is 0.57 and the fraction of O_2 is 0.43 as depicted by Reaction 8. It is likely that the maximum evaporation rate also occurs close to this value.

The saturation partial pressure of $CrO_2(OH)_2$ is low, and it appears that equilibrium is quickly reached in a stagnant gas at constant temperature. Consequently, the rate of volatilisation is proportional to the gas flow velocity at a low gas velocity. In contrast, the rate of volatilisation at a very high flow rate becomes independent of the gas flow rate. This corresponds to a situation in which the reverse direction of Reaction 8 is negligible. Froitzheim et al. [109] have described an experiment in which the rate of chromium volatilisation became independent of the gas velocity at about 0.25 m/s in air with 3 vol.% H_2O at 850 °C. In contrast, when working at 900 °C in air with 6 vol.% H_2O [64], report that the rate of chromium volatilisation continued to increase when the gas velocity was increased from 0.7 m/s to 6 m/s.

In most applications, the gas flow velocity is high and the reverse direction in Reaction 8 can be neglected. Considering the forward reaction, the theoretical values (44 kJ/mol [108]) and experimental values (60 kJ/mol [28]) show good agreement for the endothermic formation of $CrO_2(OH)_2$. Increasing the temperature of 100 °C within the interval 650-850 °C increases the evaporation rate by a factor of 2-3 [28].

5.1.1 TEDMON KINETICS

Chromium evaporation and oxide growth occur simultaneously when chromia-forming alloys are exposed at high temperatures in O_2/H_2O-environments. Tedmon [110] has proposed a kinetic model for the situation in which a surface layer growing according to parabolic kinetics is simultaneously subjected to volatilisation that is occurring at a constant rate. This is described by Equation 5, where K_d is the parabolic rate constant for oxide growth and k_s is the rate of volatilisation, measured in terms of the reduction of oxide layer thickness. According to Equation 5, at some elapsed exposure time, the rate of oxide growth must be equal to the rate of evaporation. When this happens a constant oxide thickness is obtained. By setting the scale growth to zero, the critical scale thickness can be calculated using Equation 6. This model can also be applied to gravimetric data, resulting in a net mass change that is described as paralinear due to the parabolic oxide growth and the linear evaporation rate, as illustrated in Figure 14 [104].

$$\frac{dx}{dt} = \frac{K_d}{x} - k_s \qquad \text{Equation 5}$$

$$x = \frac{K_d}{K_s} \qquad \text{Equation 6}$$

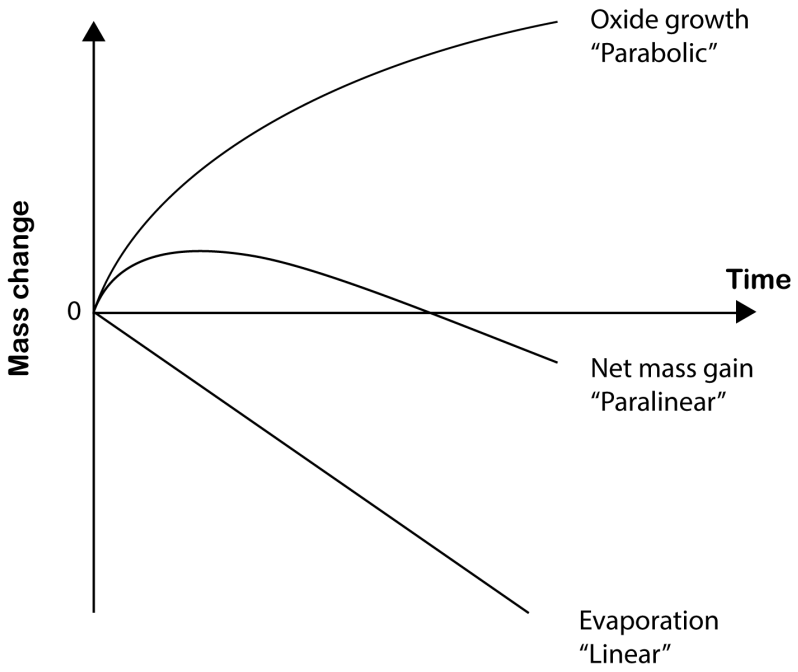

Figure 14 Schematic illustration showing paralinear behaviour of the mass change due to parabolic oxide growth and linear evaporation.

5.1.2 MITIGATING CHROMIUM EVAPORATION

As discussed above, chromium volatilisation can trigger breakaway oxidation of alloys. Moreover, when $CrO_2(OH)_2(g)$ is condensed it can cause chromium contamination of downstream processes, e.g., catalyst poisoning. The volatilisation of chromium-oxy-hydroxide can be reduced by different measures. One way to mitigate evaporation is to alloy with elements that form oxide scales with reduced levels of Cr^{3+} in the outer layer. An alloying element that has been used extensively for this purpose is manganese [28] [105]. Manganese promotes the formation of an outer layer of $(Cr,Mn)_3O_4$, which decreases the amount of chromium that is in contact with the environment, such that the evaporation rate is reduced 2-3 fold [111]. Adding a sufficient amount of aluminium to allow an alumina scale to form is a much more-efficient way to reduce chromium evaporation. However, the alumina scale is an insulator and cannot be used in applications where the metal is used as a current collector, as in the case for interconnects in fuel cells. A common approach to mitigating Cr-evaporation is to apply coatings on the steel surfaces separating the Cr-rich oxide scale from the environment. Examination of substrates coated with sub-micron thick cobalt layers that form $(Co,Mn,Fe)_3O_4$ has revealed a significant reduction of chromium evaporation [112, 113]. In addition, nickel and copper have been tested as coating materials [114-117].

5.2 WATER VAPOUR AT LOW OXYGEN PARTIAL PRESSURE

In environments where H_2O is present but O_2 is absent, the water provides the oxygen needed for oxide scale growth. Due to the lack of O_2, chromium-oxy-hydroxide cannot form. However, the rate of corrosion in such environments is higher than that seen when O_2 is present [98-100, 118, 119]. The reasons for this are poorly understood, even though many explanations have been put forward. Henry et al. [98] observed that water vapour caused faster oxidation at 900 °C, and they suggested that this was because the smaller OH^- (radius, 96 pm) diffused more rapidly through the oxide scale than the larger O^{2-} (radius, 140 pm). It has also been proposed that faster dissociation of the H_2O molecule on the oxide scale surface, as compared to O_2, influences the oxidation rate [120]. Essuman et al. [97] have observed that alloys have an increased tendency to become internally oxidised when H_2O is the single oxidant, and they have proposed that increased diffusivity/solubility of oxygen in the metal is the reason for the faster oxidation rate.

It has been observed in many cases that hydrogen is picked-up by the metal when it is oxidised by H_2O [100, 121]. The influence of such dissolved hydrogen on oxidation is not fully known. One example of the influence of dissolved hydrogen on oxidation is the so-called 'Dual atmosphere effect', which has mainly been observed for ferritic stainless steel that has steam/hydrogen on one side and air on the other side. It has been reported that under these circumstances, the oxidation rate is increased on the air side compared to when air is present on both sides of the alloy sample [122-124]. Recently, it has been proposed that the reason for the dual atmosphere effect is that the dissolved hydrogen in the metal reacts with chromium and slow down the diffusion of chromium along the alloy grain boundaries, thereby impairing the ability to form an external Cr-rich oxide [125].

5.3 WATER VAPOUR EFFECTS ON ALUMINA SCALES

Water vapour also influences the formation and growth of alumina scales. Evaporation of Al_2O_3 by water vapour is considered to be negligible at temperatures below 1300 °C and, consequently, evaporation is not considered important at normal operating temperatures [126].

FeCrAl alloys form transient oxides that contain chromium during the initial stages of oxidation. The chromium in this oxide could be subject to the formation of chromium-oxy-hydroxides. Previous studies have shown that evaporation from FeCrAl alloys is about 1-3 magnitudes lower than that from chromia scales at temperatures in the range of 800-1000 °C [94] [106]. With a prolonged exposure at high temperature, the amount of chromium in the outer part of the oxide scale should be very low and evaporation of chromium-oxy-hydroxide should be minimal.

Water vapour influences the structure of the alumina scale. It has been observed that the oxidation rate is higher in wet air than in dry air [127]. This has been attributed to that water vapour stabilises γ-alumina, which grows faster than α-alumina [89]. Recently, it has been observed that in environments with water vapour as the single oxidant, water molecules are transported across the alumina scale *via* the oxide grain boundaries [57].

6 CORROSION BY NITROGEN

The nitrogen molecule, N_2, is less reactive than the oxygen molecule, O_2. However, at high temperatures, N_2 can adsorb to and dissociate on metal surfaces and subsequently dissolve into the metal, resulting in nitridation. Nitridation can reduce the life-times of components due to nitride precipitation with alloying elements such as chromium, aluminium and titanium. Nitridation is often observed in environments with high nitrogen activity and low oxygen activity, e.g., in bright annealing. The stability of the metal nitrides and oxides can be illustrated in phase stability diagrams, which plot the activity of nitrogen on one axis and the activity of oxygen on the other axis, see Figure 15.

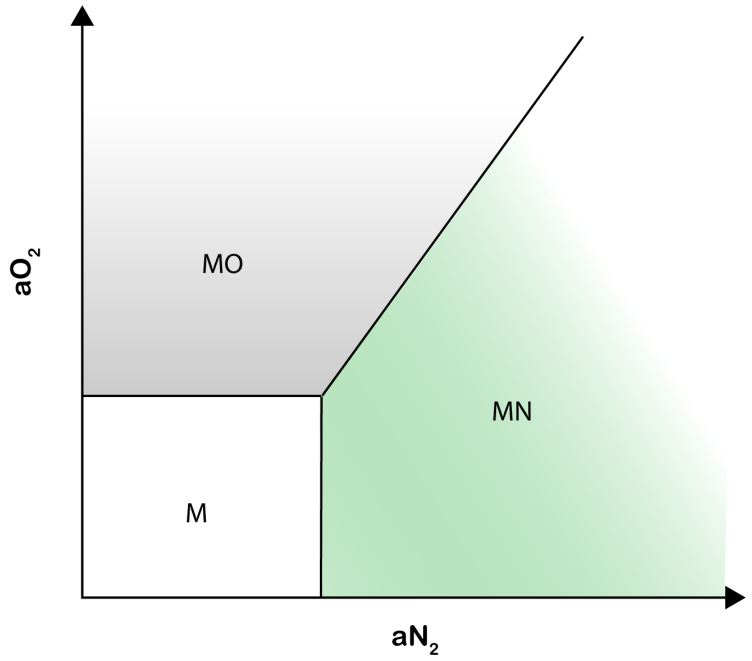

Figure 15 Phase stability diagram between a metal (M) and its oxides (MO) and nitrides (MN).

The solubility of nitrogen in an alloy depends on both its structure (e.g., austenitic or ferritic) and chemical composition. The amount of nitrogen that can be dissolved in austenite is higher than in ferrite [128]. In the austenitic phase, the solubility decreases with nickel concentration; at 1000 °C, the nitrogen solubility is about 0.02-0.03 wt.% in pure iron (γ-Fe) and decreases to <0.0001 wt.% with a nickel concentration of 80 wt.% (20 wt.% Fe) [128]. The lower solubility of nitrogen in Ni-base alloys may explain why the ability of austenitic alloys to resist nitridation increases with the nickel concentrations [129]. When the alloy becomes super-saturated with nitrogen, nitrides may nucleate and grow. Among the most-stable nitrides in high-temperature resistant alloys are TiN and AlN [130]. However, since the concentration of chromium in the alloy is often much higher than the concentrations of titanium and aluminium, chromium nitrides usually predominate (FeCrAl alloys often being exceptions to

this). Chromium can form two stable nitrides, Cr_2N and CrN, with the activities of nitrogen and chromium determining which phase is the most stable according to Reactions 9 and 10.

$$Cr_2N(s) + \frac{1}{2}N_2(g) \leftrightarrows 2CrN(s) \qquad \text{Reaction 9}$$

$$Cr_2N(s) \leftrightarrows 2CrN(s) + Cr(ss) \qquad \text{Reaction 10}$$

Cr_2N is the nitride that forms first [131, 132], and CrN has only been observed on alloy surfaces after lengthy exposures [129]. At temperatures >1049 °C (pN_2 = 1 atm.), CrN is no longer stable and Cr_2N is the only stable chromium nitride [133, 134]. Pure chromium and alloys that contain very high concentrations of chromium are reported to form a continuous chromium nitride sub-scale [131, 135]. In contrast, in Cr-containing Fe-base and Ni-base alloys, Cr_2N forms dispersed precipitations in the alloy bulk, which often appear as needles [132]. If the alloy contains titanium and/or aluminium, the Cr_2N precipitates can grow on existing TiN and/or AlN [129]. Nitridation follows a parabolic rate law similar to that for oxidation, although the rate of nitridation tends to be much faster than the rate of oxidation [136].

Since N_2 is relatively stable, it is important to consider its dissociation on metal surfaces, and it is noteworthy that N_2 dissociation is catalysed by some surfaces. It has been reported that N_2 dissociates more easily on metallic iron than on nickel [137]. This may be another reason why Ni-base alloys show better resistance to nitridation than Fe-base alloys.

6.1 Nitridation in the presence of oxide scales

When the oxygen activity in the environment is sufficient to form a surface oxide, there is an impact on the nitridation behaviour of the alloy. The presence of a surface oxide affects nitridation in two ways. First, the surface oxide influences the dissociation of N_2. Second, the surface oxide acts as a barrier to the ingress of nitrogen into the alloy. The layer-forming oxides that are in focus in this thesis are chromia, alumina and silica.

6.1.1 Chromia scales

It has been reported that chromia scales are both good substrates for N_2 dissociation and are permeable to nitrogen [14, 138, 139]. However, little is known about how nitrogen is transported through the chromia scale. It has been proposed that molecular nitrogen penetrates the scale through pores and defects [5, 140]. Another mechanism, which has been suggested but never observed, involves nitrogen penetrating the chromia scale through oxide grain boundaries in a manner similar to that observed for carbon [6]. It has also been reported that the presence of water vapour slows the ingress of nitrogen through a chromia scale [141].

6.1.2 ALUMINA SCALES

Alumina scales have been reported to protect against nitridation [14, 142, 143]. Earlier work has shown that nitridation of alumina-forming alloys occurs at defects in the alumina scale, while the alumina scale itself appears to be impermeable [14, 144]. Furthermore, First-principle calculations have indicated that α-Al_2O_3 surfaces are poor catalysts for N_2 dissociation [14]. However, due to the strong affinity of aluminium for nitrogen, severe nitridation may result if nitrogen is able to enter the alloy through defects in the alumina scale [144-147].

6.1.3 SILICA SCALES

Little is known about the permeability of nitrogen through silica on alloy surfaces. While silica glass is known to be permeable to gases [148, 149], it remains unclear as to how this permeability would manifest itself in a situation where silica forms a barrier between a metal and an N_2-rich environment.

7 EXPERIMENTAL PROCEDURE

The exposures of the different alloys to high-temperature environments were performed in the laboratories of Chalmers University of Technology. Details of the experimental techniques are described in the following sections.

7.1 SAMPLE PREPARATION

Prior to exposure, the corrosion coupons were prepared in order to achieve a homogeneous and smooth surface. The purposes of the sample preparation are to reduce any influence that different surface structures would have on the results, and facilitate easier microscopy examinations. The coupons were prepared by grinding the edges with 1000 grit SiC-paper. The faces of the coupons were first ground to 4000 grit coarseness, followed by polishing with a diamond paste in successive steps to obtain a mirror-bright appearance with a surface roughness of 1 µm. After polishing, cleaning of coupons was performed in two steps in an ultrasonic bath. In the first step, the coupons were submerged in acetone for 10 minutes, and in the second step they were placed in ethanol for 10 minutes. The coupons were then sized using a 3-decimal digital calliper and weighed using a 6-decimal scale of Mettler Toledo.

7.2 FURNACE EXPOSURES

High-temperature exposures were performed in electrically heated, horizontal tube furnaces. Two different set-ups were used, either the ‘high oxygen activity’ set-up or the ‘low oxygen activity’ set-up. The exposure parameters in the different exposures are summarised in Table 2 and the set-ups are described in the following sections.

Table 2 Exposure parameters for the different set-ups.

Gas composition	Temperature (°C)	Flow velocity (cm/s)	Dew-point (°C)	Water content	Calculated αO_2
High oxygen activity					
Air	600	9.8	-59	11.9 ppm	0.21
Air	800	23.7, 11.8	-59	11.9 ppm	0.21
Air + 20% H_2O	500	2.8	60	20%	0.17
Air + 20% H_2O	600	3.2	60	20%	0.17
Air + 40% H_2O	600	9.8	76	40%	0.13
Air + 20% H_2O	700	3.6	60	20%	0.17
Air + 20% H_2O	800	4.0	60	20%	0.17
Air + 20% H_2O	800	11.8	60	20%	0.17
Air + 20% H_2O	800	23.7	60	20%	0.17
Air + 20% H_2O	800	31.6	60	20%	0.17
Air + 40% H_2O	800	11.8	76	40%	0.13
Low oxygen activity					
20% H_2 + 20% H_2O + Ar	800	1.0	60	20%	$4.4*10^{-19}$
95% N_2 + 5% H_2 + ~ 3 ppm O_2	800	0.6	-64	6.5 ppm	$7.7*10^{-27}$
95% N_2 + 5% H_2 + ~ 22 ppm O_2	900	0.6	-49	45 ppm	$1.7*10^{-22}$
95% N_2 + 5% H_2+ ~ 7 ppm O_2	900	0.6	-58	14 ppm	$1.6*10^{-23}$
95% N_2 + 5% H_2 + ~ 5 ppm O_2	1100	0.7	-61	10 ppm	$4.0*10^{-21}$

7.2.1 HIGH OXYGEN ACTIVITY SET-UP

The set-ups of the furnaces are schematically shown in Figure 16. The inlet air consisted of dried ambient air that was purified by passing the gas through several filters, including one with potassium permanganate to reduce the water content. The flow rate was set at between 1000 ml/min and 8000 ml/min depending on the exposure, and the gas flow was calibrated using a MesaLabs Defender 530+ flow meter. Fused silica reactor tubes with an inner diameter of 55 mm were used. Exposures were performed in both dry air and in air that contained 20-40 vol.% H_2O. The air was moistened by bubbling the inlet air in a heated water bath so that it became saturated with water. The saturated air was then passed through a reflux condenser to obtain the desired dew-point: either 60.4 °C for 20 vol.% water content or 76.3 °C for 40 vol.% water content. Calibration of the dew-point was performed with a Michell Instruments Optidew Vision chilled mirror humidity sensor. In the horizontal tube furnace, the gas was heated to the exposure temperature, which was in the range of 500-800 °C depending on the exposure. The samples were positioned parallel to the gas flow direction, using Al_2O_3 sample holders. For all the exposures, triplicate samples were used. In the reaction tube, the gas first passed through a flow restrictor to create a more-homogenous gas flow. Downstream of the samples, the gas was led into a so-called 'denuder' tube. The denuder tube was coated with Na_2CO_3 to promote a reaction with the gaseous $CrO_2(OH)_2$ present in the gas stream according to Reaction 11.

$$CrO_2(OH)_2(g) + Na_2CO_3(s) \rightarrow Na_2CrO_4(s) + H_2O(g) + CO_2(g)$$ Reaction 11

The denuder tube was replaced during the exposure so that a time-resolved picture of the chromium evaporation rate could be obtained. When the denuder tube had been replaced it was leached with Milli-Q water and the concentration of chromate in the solution was determined by a Fischer Scientific evolution 60s UV/Vis spectrophotometry. The end of the denuder tube was connected to a wash bottle, to collect any Na_2CrO_4 that may have followed the gas stream, being lost from the denuder tube. The solution in the wash bottle was subsequently evaporated down to 20-50 ml and analysed for chromate in the same way as the leached solution from the denuder tube. To avoid condensation, the humid gas stream was heated using heating cords located between the reflux condenser and the inlet to the furnace, as well as downstream of the furnace to the end of the denuder tube.

At the start of the exposure, the samples were inserted into the furnace, which was already at the operating temperature, resulting in the samples reaching the exposure temperature after only about 5 minutes. Humidification was switched on about 2 minutes after the samples were inserted into the furnace.

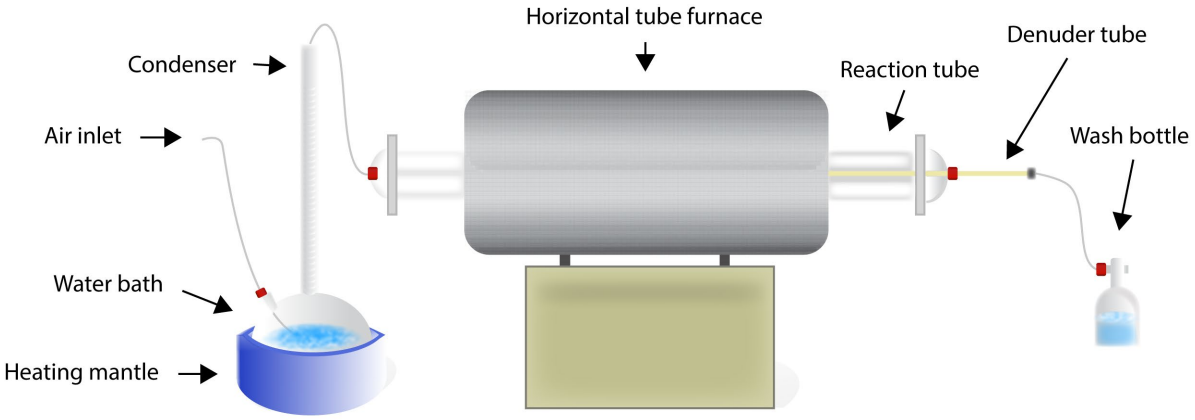

Figure 16 Schematic illustration of the set-up for the high-temperature exposures.

7.2.2 Low oxygen activity set-up

The set-up for the low oxygen activity exposures consisted of horizontal tube furnaces equipped with sintered alumina tubes for all exposures, with the exceptions of the exposures at 800 °C with 95% N_2 + 5% H_2 for which a fused quartz reaction tube was used. For the exposures with 95% N_2 and 5% H_2, the gases were injected directly into the reaction tube at a flow rate of 100 ml/min. The O_2 impurities originate both from the nitrogen gas used and from leakage from the fittings in the set-up. The concentration of O_2 impurities in the gas was measured in pure N_2 using a Rapidox 2100ZF oxygen analyser, and was also determined in the real exposure gas by measuring the dew-point downstream of the furnace where O_2 had reacted with H_2 to form H_2O. The dew-point of the gas was measured using a Michelle

Instruments S8000 high-precision chilled mirror hygrometer. The oxygen activity at the experimental temperature was then calculated using the Thermo-Calc software and the SSUB6 database. In the set-up with 20% H_2O + 20% H_2 + Ar, the gas mixture was bubbled through a water bath in a manner similar to that shown in Figure 16, with the only differences being that stainless steel tubing was used instead of PTFE tubing and a flow rate of 200 ml/min was used.

As in the high oxygen activity set-up, triplicate samples were used for all the exposures, placed in Al_2O_3 sample holders. For the low oxygen activity exposures, the samples were placed inside the furnace at room temperature and the system was then purged with either nitrogen or argon for 24 hours. After purging, the furnace was turned on and the operating temperature was reached after 1-2 hours. In the case in which the environment contained 20% water, this was added to the gas mixture after the furnace reached about 150 °C. After the exposure, the furnace was turned off, reaching ambient temperature after about 8-10 hours. The water was turned off at about 150 °C in order to avoid condensation.

8 Analysis techniques

The corrosion products formed were examined using a wide range of analytic techniques. The different techniques provide complementary information such that a more comprehensive understanding of the corrosion mechanism can be obtained. For instance, X-ray diffraction (XRD) gives information about the crystallographic structure, energy-dispersive X-ray spectroscopy (EDS) provides chemical information, and SEM provides information about the morphology. The resolution and detection limits of the different techniques applied in this thesis are presented in Figure 17. The principles of these techniques are described briefly in the following sections.

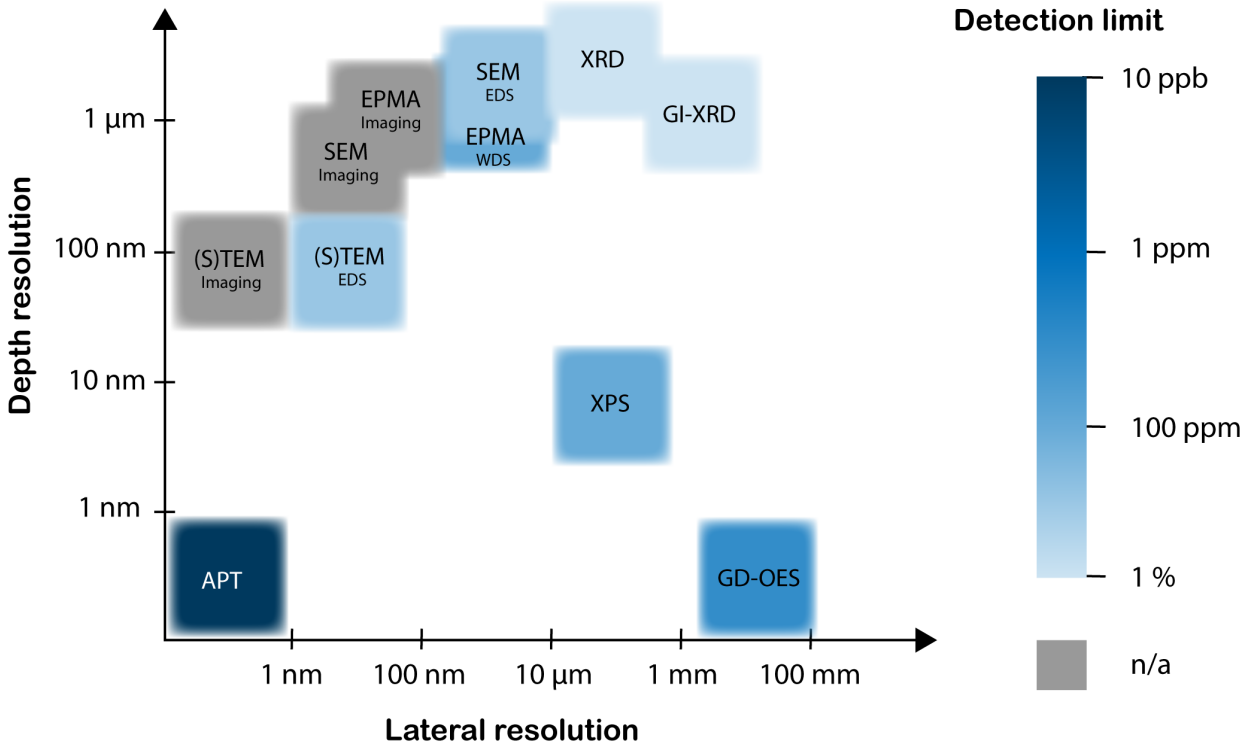

Figure 17 Typical resolution and detection limits of the different analytic techniques applied in this thesis.

8.1 Sample preparation techniques

Exposed coupons were subjected to different preparation techniques, i.e., broad ion beam (BIB) milling and focused ion beam (FIB) milling, depending on which kind of analysis that was going to be employed in the subsequent studies. Analyses using X-ray techniques, glow discharge optical emission spectroscopy (GD-OES), and plan-view examination by SEM were carried out on the samples in the as-exposed condition.

8.1.1 Broad ion beam milling

A BIB was used to mill cross-sections of areas of interest. This technique has the advantage that it removes material without mechanically affecting the sample, thereby avoiding

artefacts associated with cutting, grinding and polishing. A BIB consists of multiple ion guns that bombard the metal with Ar^+ ions, gently removing material. The BIB used in this work was a Leica TIC3X with three argon guns, which are fixed in a vacuum chamber and directed towards the sample stage where the samples are mounted. A mask was used to select an area of interest and the ion guns milled away material from the unmasked area. The BIB allows milling to a depth of about 1 mm in a few hours, making it a relatively fast and easy tool to generate cross-sections. Prior to BIB milling, the samples were sputtered with a thin gold layer for better conductivity, and a silicon wafer was glued onto the samples to reduce curtain effects [150]. A low-speed cutting saw was used to cut the sample in half before it was placed in the BIB. For the milling process, an applied voltage of 6.5 kV and a current of 2.4 mA were applied.

8.1.2 Focused ion beam milling

FIB milling was used to prepare samples for analysis by scanning transmission electron microscopy (STEM) and atom probe tomography (APT). The principle of this technique is the use of an electron microscope equipped with an ion-gun that employs Ga^+ ions to perform site-specific, in-situ sample preparation. By applying this technique, thin foils of the area of interest can be prepared for further examination in what is termed the 'lift-out' technique. The process steps in the lift-out technique consist of: deposition of platinum onto the area of interest; the milling of trenches; performance of a U-cut; and transfer to a sample-holding grid. Further examination of the sample is then performed by STEM or APT.

In this work a FEI Versa 3D FIB-SEM was used to mill out areas of interest. FIB milling was performed by Vijayshankar Asokan, Mohammad Sattari and Andrea Fazi.

8.2 X-Ray diffraction

X-ray diffraction was used to identify the crystalline phases in the oxide scales and corrosion products formed after the exposures. This is a very useful technique as most of the formed compounds are in crystalline form. In X-ray diffraction, a monochromatic X-ray source is used to shine X-rays onto a target sample. In this work, an X-ray source emitting CuKα-radition with a wavelength (λ) of 1.5418 Å was used. The X-ray beam is diffracted by the crystal lattice according to Bragg's Law, see Equation 7. The underlying principle is illustrated in Figure 18. In Bragg's Law, d is the lattice parameter, λ is the wavelength, θ is the incidence/diffracted angle, and n is an integer. By comparing the d-values and intensities of the measured peaks of the reflected X-rays with a collection of powder diffraction files (PDFs), it is possible to determine the phase structures present in the examined sample.

$$n\lambda = 2d_{hkl}sin\theta \qquad \text{Equation 7}$$

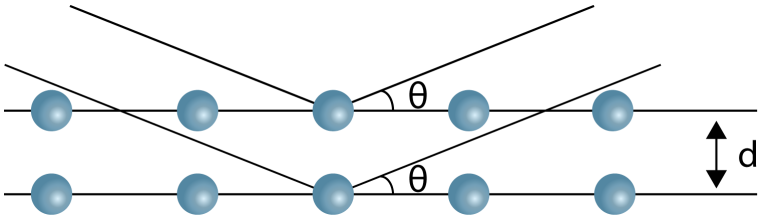

Figure 18 Illustration of Bragg´s Law whereby diffraction of an X-ray beam by an atom lattice can be used to determine the lattice parameter d.

Two different X-ray diffraction set-ups were used in this thesis: (i) the traditional Bragg-Brentano (BB) geometry; and (ii) grazing-incidence X-ray diffraction (GI-XRD). In the BB set-up, scanning is performed by having the angle, θ, for both for the incident beam and reflecting beam, as illustrated in Figure 19a. In GI-XRD, the X-ray beam has a fixed incidence angle (1°, and 0.2° in this work) and a moving detector, see Figure 19b. Due to the low angle of incidence, the penetration depth is shallow, making GI-XRD a suitable method for analysing thin oxide scales on metal surfaces. The draw-back of this technique is the lower intensity of diffraction obtained, which means that long measuring times are needed. In this work, a Siemens D5000 diffractometer equipped with a Göbel mirror was used for the GI-XRD measurements, and a Bruker D8 Advance Diffractometer was used for the BB-XRD measurements.

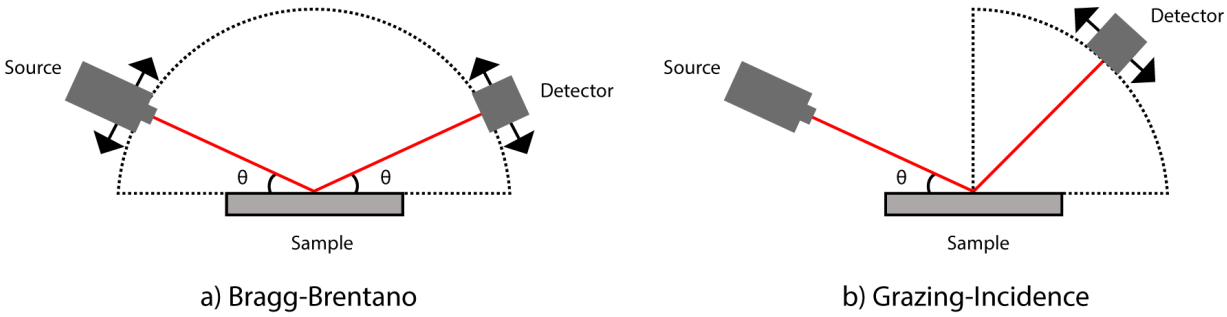

Figure 19 Illustration of the set-up for the: a) Bragg-Brentano XRD and b) Grazing-Incidence XRD.

8.3 Scanning electron microscopy

Scanning electron microscopy was the main tool used to characterise the microstructures of the corrosion products. SEM resembles an optical microscope but instead of visible light, electrons are used to create images of the sample microstructure. This makes it a useful technique for examinations of surface topography, as well as chemical composition.

In SEM, electrons are emitted from an electron gun, accelerated by a high voltage and focused by electron lenses before interacting with the sample surface. The electrons can be focused so that the SEM can achieve a lateral resolution of about 1 nm [151]. The focused electrons are scanned in the *x-y* directions, generating a 2-dimensional image of the surface.

The interaction of electrons with the sample results in various signals, such as secondary electrons (SE), backscattered electrons (BSE), and characteristic X-ray radiation [151]. SE are electrons that are emitted from sample atoms due to inelastic scattering of primary electrons, see Figure 20a. If these secondary electrons attain sufficient kinetic energy, they can leave the surface and be detected. Typically, this can only happen for the outermost part of the sample, resulting in a topographic image of the sample.

BSE are electrons originating from the electron beam that have entered the material and which, as a result of inelastic and elastic scattering, change trajectory in the material due to interactions with the atoms in the material, see Figure 20b. As BSE have higher energy than SE, they can be distinguished from each other. Atoms with a higher atomic number (Z) generate a higher number of BSE, creating contrast differences in the final image that provide information about atom numbers. The interaction volume from BSE is significantly larger than that from SE, so the information obtained comes from an area deeper inside the material.

Characteristic X-rays are generated when an electron knocks out an electron from an orbital in one of the sample atoms. This causes electrons from the outer orbitals to fill the place vacated by the knocked-out electron, and X-ray photons are emitted. Since the energy of the emitted X-ray photons is characteristic for a specific element, it is possible to determine this element from the detected photon energy. This mechanism can occur relatively deep inside the material, and might not be identical to the images generated by secondary and backscattered electrons. The technique to determine elemental composition using characteristic X-rays is called energy-dispersive X-ray spectroscopy (EDS).

In this work, a Quanta 200 SEM equipped with a field emission gun (FEG) was used. An acceleration voltage of 10-20 kV was used for imaging and 20 kV were used for the EDS analysis. For high magnification imaging, a Zeiss Ultra 55 FEG-SEM with an acceleration voltage of 2 kV was used.

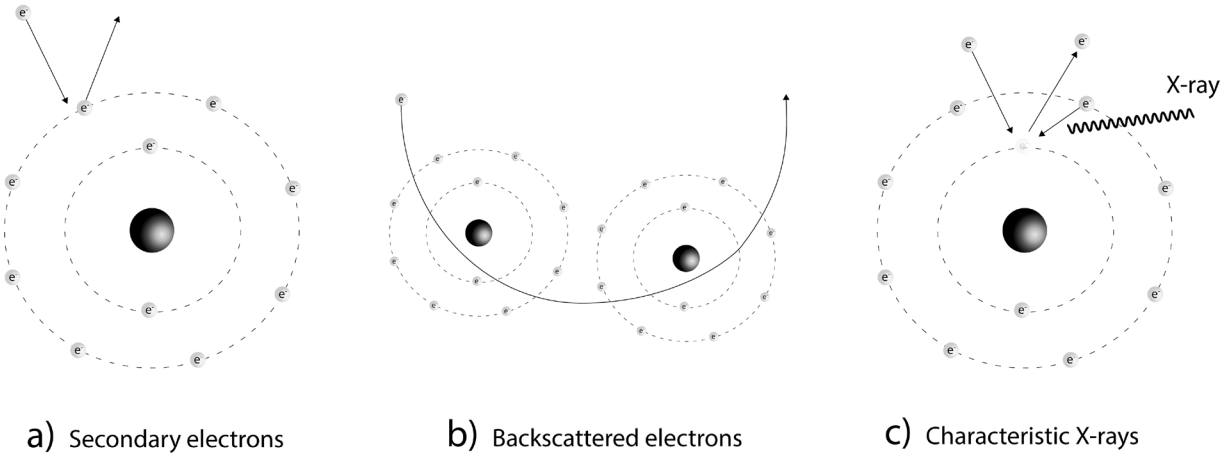

Figure 20 Illustration showing how (a) secondary electrons, (b) backscattered electrons, and (c) characteristic X-rays can be generated in the SEM.

8.4 TRANSMISSION ELECTRON MICROSCOPY

TEM was used for detailed investigations of the corrosion products. In TEM, electrons are accelerated to a specimen in a similar way as for SEM, with the difference that in TEM the electrons are transmitted through the specimens and apertures and detectors are used to collect signals on the other side of the specimen. This gives less interference of the beam, as compared to when the electrons are backscattered from a bulk specimen, and consequently generates a better resolution. Scanning transmission electron microscopy (STEM) is a mode where the electron probe is scanning over the area of interest. In STEM mode, different detectors can be used, such as annular dark-field (ADF), high-angle ADF (HAADF), and bright field (BF) [152]. The BF detector is positioned to be aligned towards the direct beam and detects forward-scattered and un-scattered electrons, while the HAADF detector is positioned around the BF detector so that scattered electrons can be detected. The different detectors complement each other; HAADF provide Z-contrast for instance. In addition, in TEM, convergent beam electron diffraction (CBED) can be used to obtain crystallographic information from specimen regions.

The specimens for TEM need to be thin, typically <100 nm but in some cases even <50 nm in thickness, so that the electron beam can be transmitted through the specimen [152].

The STEM analyses in this work were performed by Vijayshankar Asokan and Mohammad Sattari.

8.5 X-RAY PHOTOELECTRON SPECTROSCOPY

X-Ray photoelectron spectroscopy (XPS) was used in this work to analyse the chemical gradients in the formed oxide scales. In XPS, the area of interest is subjected to monochromatic X-ray radiation. In this work, a beam size of 100 µm was used, representing

the lateral resolution. The electrons emitted from the surface are collected by an electrostatic lens. The binding energy can be calculated from the kinetic energy from the electrons, which is converted to chemical information by an energy analyser. The acquired information includes the chemical composition but also the oxidation states of the different atoms. The depth resolution is a few nanometres, making it a suitable analytical tool for surface characterization [153]. Depth profiling was accomplished by etching the area of interest by Ar-sputtering. The nominal etching rate is 58.5 Å/min in a reference sample of Ta_2O_5.

The XPS analysis in this work was performed by Yu Cao using a PHI5500™ equipped with an AlKα-source.

8.6 GLOW DISCHARGE OPTICAL EMISSION SPECTROSCOPY

GD-OES was used to obtain nitrogen depth profiles from samples that were exposed to a nitriding environment. This technique is fast to perform, has good depth resolution, and is commonly used to characterise thin films. The principle of the technique is that a plasma is created using a hollow anode and letting the sample act as the cathode. In the plasma, argon atoms are ionised and accelerated towards the samples. Upon impact, the argon ions eject the atoms from the surface layer of the sample. The ejected atoms create an optical emission due to the transition back from the excited ground state. The optical spectrum is then analysed with regard to the chemical composition. Due to the continuous sputtering, a depth profile is obtained.

The GD-OES analysis in this work was performed by Jan Andersson and Lennart Eriksson using a Spectruma GDA750 HR operating in DC mode at 800 V and 15 mA. The anode was ring-shaped with a diameter of 2.5 mm, which determined the lateral resolution. The maximum measuring depth is about 50-100 µm due to the fact that a crater is formed in the analysed area, as shown in Figure 21, whereby the ridges of the crater build up and eventually cause a short-circuit with the anode. In this thesis, multiple measurements were performed on the same area and where the crater was mechanically removed by grinding between measurements. By repeating this procedure multiple times, depth profiles of about 350 µm were obtained.

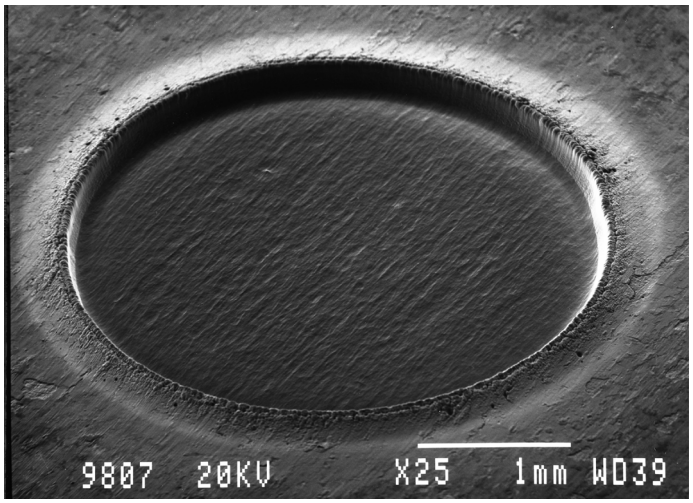

Figure 21 An approximately 100 µm deep crater formed after GD-OES measurement. Image courtesy of Jan Andersson, Sandvik Materials Technology.

8.7 Atom probe tomography

APT was used in this thesis to detect nitrogen inside an oxide scale. APT provides near-atomic resolution in combination with chemical information about the detected atoms. In APT, the sample is in the form of very sharp tips that are prepared by the lift-out technique using FIB milling as described in Section 8.1.2. In the atom probe instrument, the specimen is kept at cryogenic temperature and subjected to a high DC current which, combined with the very small radius (tens of nanometres), results in a localised strong electrostatic field. Under these conditions, atoms on the surface of the tip are brought close to field evaporation and can be ionised by a laser pulse or a voltage pulse. The ionised species (atomic ions or complex ions) are accelerated by the standing DC voltage onto a 2D position-sensitive detector. The time that elapses between the laser or voltage pulse and the hit event on the 2D position-sensitive detector provides the time-of-flight of each individual ion, which is used to calculate the specific mass-to-charge ratios and allows one to obtain chemical information. Using continuous measurements, millions to billions of atoms can be evaporated and detected from each specimen [154], the data from all the ions are then re-constructed inside a 3D virtual space so that a 3D model can be rendered.

The APT analysis in this thesis was performed by Andrea Fazi using a LEAP 3000X HR operating in pulsed laser mode with laser pulse frequency of 200 kHz, specimen temperature of 45 K, laser pulse energy of 0.5 nJ, and evaporation rate of 0.20%. The CAMECA IVAS 3.6.14 software was used for data reconstruction and data evaluation.

8.8 Electron probe micro analyser

An electron probe micro analyser (EPMA) was used in this thesis to analyse the chemical profiles of chromium and nitrogen over the cross-sections of the samples. The EPMA is similar

to the SEM in principle, in that electrons are emitted from an electron source and accelerated by a voltage and focused by electron lenses before hitting the specimen. As in SEM, secondary electrons, backscattered electrons and characteristic X-rays are obtained in the EPMA. The main difference between SEM and EPMA is that the EPMA uses a technique called wavelength dispersive X-ray spectrometry (WDS). In WDS, the wavelength of the emitted X-rays is used to detect elements by using crystals with known lattice spacing that diffract X-rays that fulfil Bragg's Law, see Equation 8. Multiple crystals are used so that many different elements can be detected. The use of WDS gives EPMA the advantage that light elements, such as carbon and nitrogen, can be detected, with high accuracy and at low concentrations, which is difficult to accomplish with SEM-EDS.

The analyses with the EPMA were performed by Anand Rajagopal using a JEOL 8530 F Plus equipped with five WDS spectrometers. The measurements were performed at an accelerating voltage of 15 kV with a current of 20 nA.

8.9 SPECTROPHOTOMETRY

Spectrophotometry was used to measure the concentrations of CrO_4^{2-} in aqueous solutions. The volatilised chromium was collected by the denuder technique described in Section 7.2.1. Solutions that contain CrO_4^{2-} are yellow in colour, with the maximum absorption of light occurring at a wavelength of 370 nm. Spectrophotometry is a technique whereby monochromatic light is transmitted through a cuvette containing the solution. The intensity of the transmitted light is measured by a photometer. The Lambert-Beers Law, Equation 8, expresses the relationship between the absorbance and concentration of the solution, where A is the absorbance, ε is the wave-length dependent molar absorptivity, and l is the path length.

$$A = \epsilon * l * c \qquad \text{Equation 8}$$

Before measuring the sample solution, a calibration curve is prepared by using solutions with precisely known concentrations and measuring their absorbance. The standard curve used in this work is presented in Figure 22, in which a Merck chromate standard solution was diluted with 0.1 M NaOH to obtain various concentrations. The spectrophotometer used was a Fischer Scientific evolution 60s UV/Vis. The solutions measured were in all cases controlled to have a pH >9, in order to ensure that the ions in the solutions were in the state of CrO_4^{2-}(aq) rather than $HCrO_4^-$ (aq) [155].

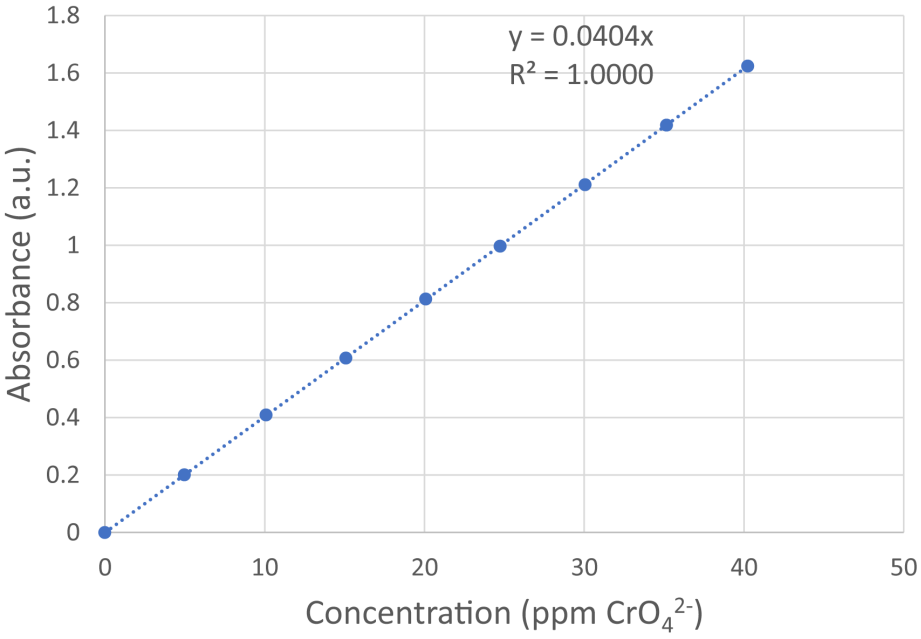

Figure 22 Calibration curve showing the absorbance values of the solutions as a function of the concentration of chromate.

9 RESULTS AND DISCUSSION

This section presents the main results of the research and the corresponding discussion, and is divided into two parts. In the first part, the results from the exposures performed in air with water vapour are presented for both chromia-forming and alumina-forming alloys, focusing on the oxide morphology and chromium evaporation. The second part presents the results obtained from exposures conducted in environments at low oxygen activity, with either high water content or high nitrogen content. In the high nitrogen environment, the main focus was on how effective chromia and alumina scales are at protecting against the ingress of nitrogen into the alloy at 900 °C. Furthermore, results are presented that reveal the extent of nitridation in a time-resolved manner of some austenitic alloys at 1100 °C.

9.1 HIGH OXYGEN AND WATER VAPOUR CONCENTRATIONS

In the environment with a high concentration of oxygen, all the metallic alloy components spontaneously form solid oxides. If water is present together with the oxygen, volatile species can also be formed, as described in Section 5.1.

9.1.1 CHROMIA-FORMING ALLOYS

The stainless steels and Ni-base alloys studied in this thesis all form chromia scales. The chromia scale forms more readily as an external oxide scale in alloys that contain higher concentrations of chromium, (*cf*. Alloy 690 with 30 wt.% chromium and Alloy 600 with only 17 wt.% chromium). However, when oxygen and water are present in the environment, the highly protective chromia scale formed on Alloy 690 could be compromised by evaporation of chromium-oxy-hydroxide. Thus, if the supply of chromium is insufficient, the nickel and iron can start to oxidise. To study the process of chromia scale break-down, exposures were performed at 800 °C in environments that induced chromium evaporation to different extents. Increasing the gas flow velocity resulted in more-effective removal of $CrO_2(OH)_2$ from the sample surface, and this was expected to push the reaction towards the formation of more $CrO_2(OH)_2$. The rates of chromium evaporation observed at different gas flow velocities at 800 °C are presented in Figure 23. It can be seen in Figure 23 that the evaporation rate increases with increasing gas flow velocity, as expected. Interestingly, the slope of the evaporation rate decreases faster with time for the highest gas flow velocity. After about 180 hours, the evaporation rate for the exposure conducted at 31.6 cm/s was even lower than that seen for the exposure at 23.7 cm/s.

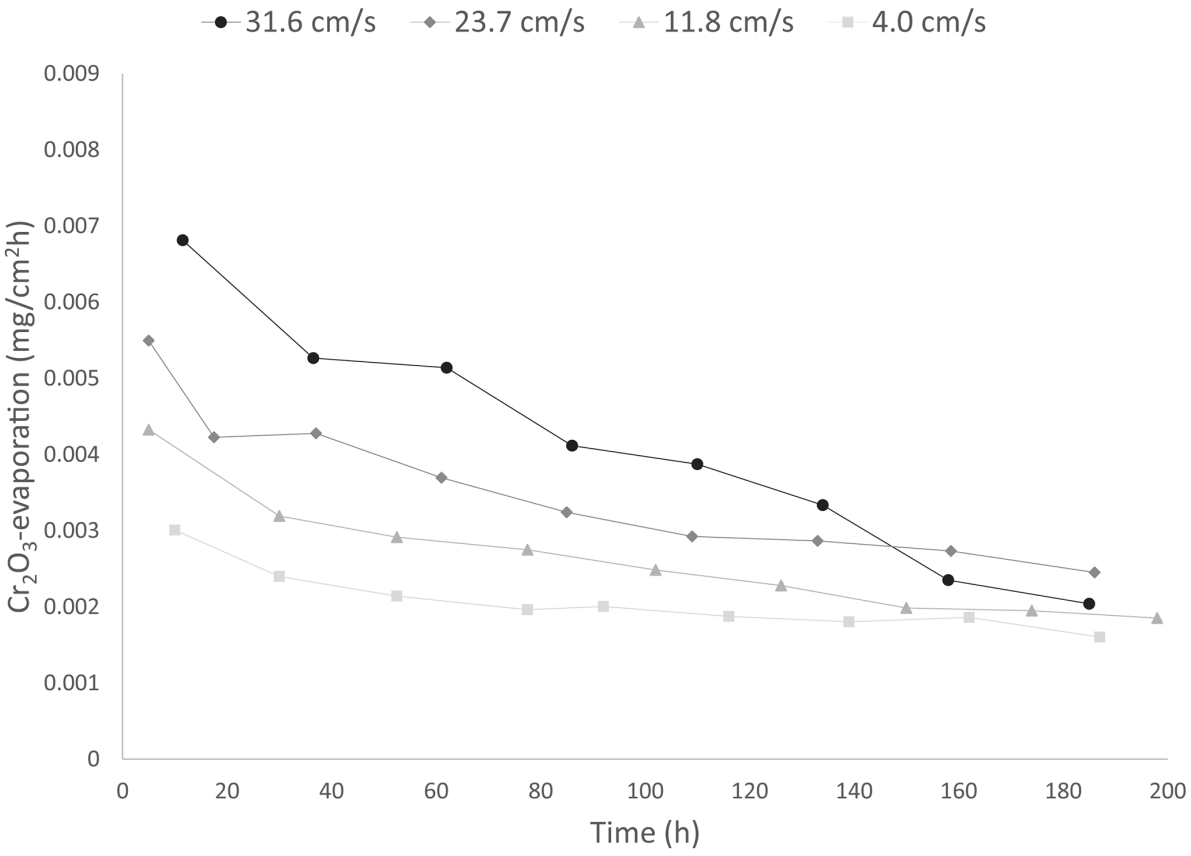

Figure 23 Evaporation rate of $CrO_2(OH)_2$ as a function of exposure time in air + 20% H_2O at 800 °C at different gas velocities.

After 200 hours, when the exposures presented in Figure 23 were terminated, the oxide scales formed on the samples were examined, see Figure 24. The exposed coupons showed different oxide morphologies. The samples exposed at the lowest flow velocity, i.e., 4.0 cm/s, exhibited a homogeneous dark oxide scale. At higher gas flow velocities, a brighter oxide scale was observed with more extensive area coverage as the gas flow velocity increased. These different areas are hereinafter referred to as the 'dark area' and 'bright area', respectively. The interface between the bright area and the dark area is represented by the red box in Figure 24, together with the corresponding top-view SEM-SE image. At the interface, it can be observed that the bright area has oxide islands covering the alloy grains, while the dark area completely lacks this feature. In the area that is more in the middle of the bright area, i.e., the blue box in Figure 24, the alloy grain boundaries also exhibit the bright oxide morphology.

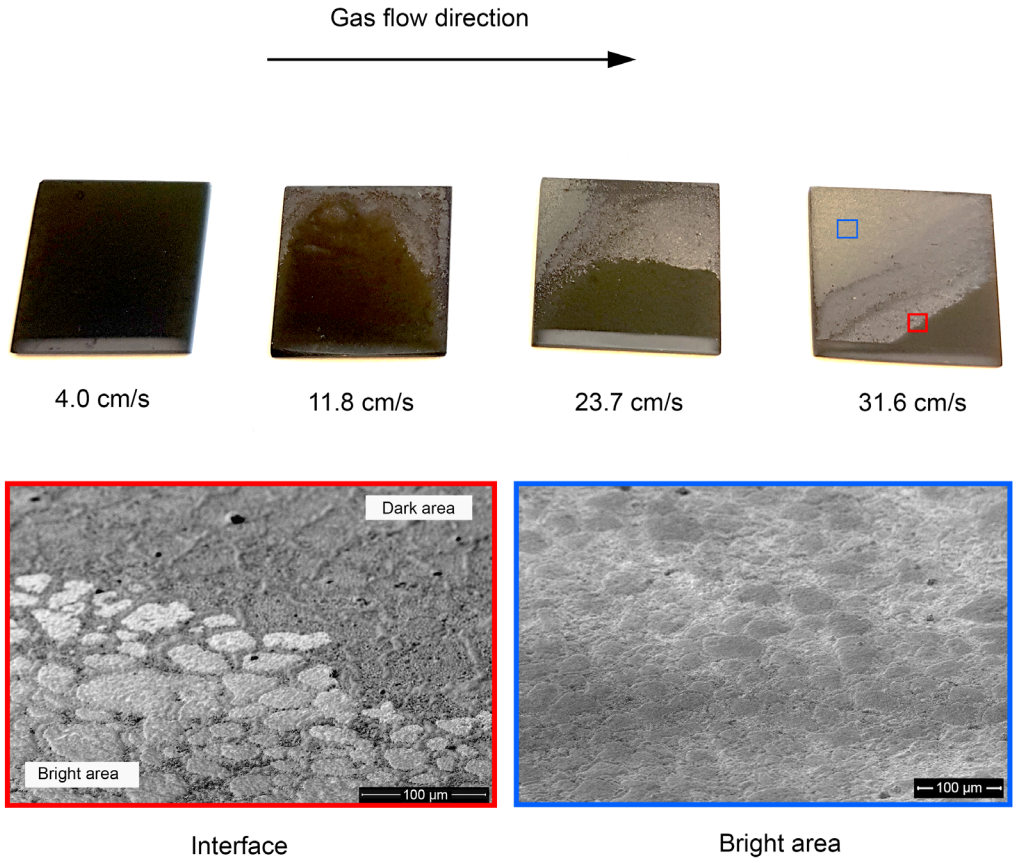

Figure 24 Top, Photographic images of samples after exposure for 200 hours in air + 20 vol.% H_2O at 800 °C and with different gas flow velocities. The direction of the gas flow during the exposures is indicated. Bottom**,** SEM-SE top-view images of the red-boxed and blue-boxed areas from samples exposed to a gas flow velocity of 31.6 cm/s.

A cross-sectional SEM-BSE image of a coupon that was exposed to a flow velocity of 4.0 cm/s is presented in Figure 25. An approximately 0.8 µm thick, continuous, dense, and adherent oxide scale is observed. The dominant cation in the oxide is Cr^{3+}, with low levels of other metallic elements, such as iron and nickel. This scale is expected to suffer rapid Cr-evaporation due to the large amount of Cr^{3+} that is in contact with the environment. Some depletion of chromium from the alloy substrate, beneath the oxide scale, is also evident.

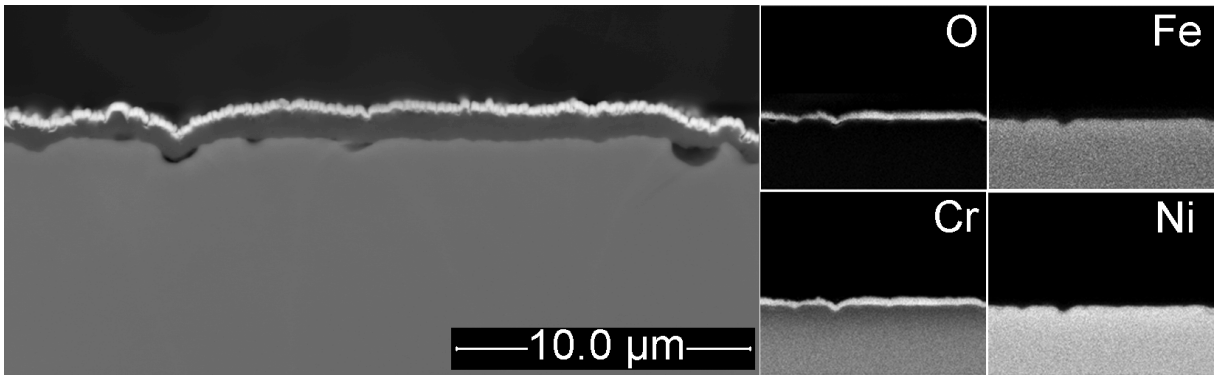

Figure 25 Cross-sectional SEM-BSE image and EDS-mappings showing the oxide scale formed after 200 hours of exposure in air + 20 vol.% H_2O and a gas flow velocity of 4.0 cm/s.

The dark area on the samples from exposure at the highest gas flow velocity, i.e., 31.6 cm/s, also shows the presence of a relatively pure chromia scale with low levels of iron and nickel, see Figure 26. The oxide has a thickness of approximately 0.5 µm, being slightly thicker at the alloy grain boundaries. Furthermore, extensive Cr-depletion is evident in the alloy substrate, especially at the alloy grain boundaries. This scale is thinner than the scale formed at the low flow velocity, see Figure 25. The extent of Cr-depletion is also greater, implying that this area has been subjected to more-extensive evaporation of $CrO_2(OH)_2$. Furthermore, the low levels of other metallic elements in the scale indicate that this scale remains susceptible to Cr-evaporation. The Cr content of the alloy was found to be in the range of 12-20 wt.% in the near-oxide region (for more details, see **Paper I**).

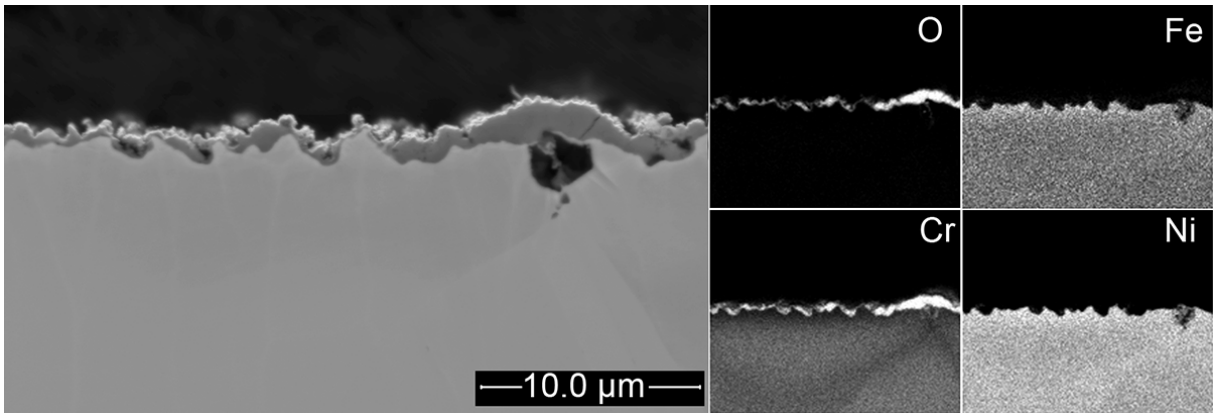

Figure 26 SEM cross-sectional image showing the oxide scale in the dark area after exposure for 200 hours in air + 20% H_2O at 800 °C and a gas flow velocity of 31.6 cm/s.

The scale microstructure in the bright area that emerged after exposure at a gas flow velocity of 31.6 cm/s is presented in Figure 27. In this bright area, the scale consists of three layers, with the top layer showing an atomic ratio of close to 1/1 for nickel to oxygen, indicating almost pure NiO. The middle layer consists of a mixture of Cr-, Ni-, and Fe-oxides, which are proposed to correspond to different spinel (M_3O_4) phases. The third layer, which is the one closest to the metal interface, is rich in chromium and is assumed to comprise rather pure

Cr_2O_3. At the alloy grain boundaries, a slightly different oxide scale is formed, consisting mainly of an outer layer of NiO and an inner layer of chromia. Since the amount of chromium in the outer part is very low, this oxide is expected to experience a low level of evaporation of $CrO_2(OH)_2$. The scale microstructure in the bright area likely explains the dramatic drop in evaporation rate seen for the exposures at high gas flow velocities, see Figure 23. The approximately 1 µm thick chromia scale at the oxide/metal interface is also noteworthy. This chromia scale is dense and is suggested to act as a robust barrier to diffusion.

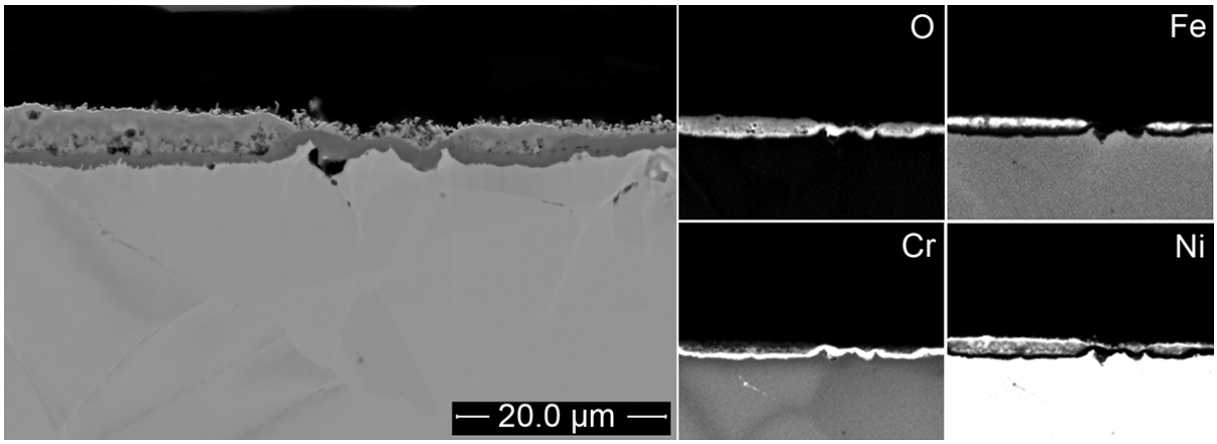

Figure 27 SEM cross-sectional image showing the oxide scale in the bright area after exposure for 200 hours in air + 20% H_2O at 800 °C and a gas flow velocity of 31.6 cm/s.

A comparison of the microstructures of the dark and bright areas highlights dramatic differences. The higher degree of surface coverage of the bright surface seen at high flow velocities where Cr-evaporation has been more extensive indicates that the bright area formation is triggered by Cr-depletion of the metal. When the chromium content of the alloy reaches a critical value, in the range 12-20 wt.%, the Cr-rich oxide scale breaks down and oxidation of nickel and iron occurs. The enrichment of nickel in the outer part of the scale eventually leads to the formation of a rather pure NiO at the oxide/gas interface. This 'cap-layer' dramatically reduces the evaporation of $CrO_2(OH)_2$. When Cr-evaporation ceases, and chromium is no longer being consumed, the chromium content of the metal near the oxide/metal can be recuperated through diffusion and thereby form a secondary chromia layer. This secondary chromia layer acts as a diffusion barrier and reduces the oxidation rate (for an illustration of the proposed mechanism, see Figure 28). In less-aggressive environments, as in the case with the lowest gas flow velocity, chromium is continuously supplied to the scale by diffusion, and since the evaporation rates are lower, a critical level of Cr-depletion is not reached.

The final scale created in the bright area is considered to act as protection against both the evaporation of $CrO_2(OH)_2$ and excessive oxidation (see **Paper I** for a proof-of-concept study). This is attributed to the high chromium content of 30 wt.% in Alloy 690.

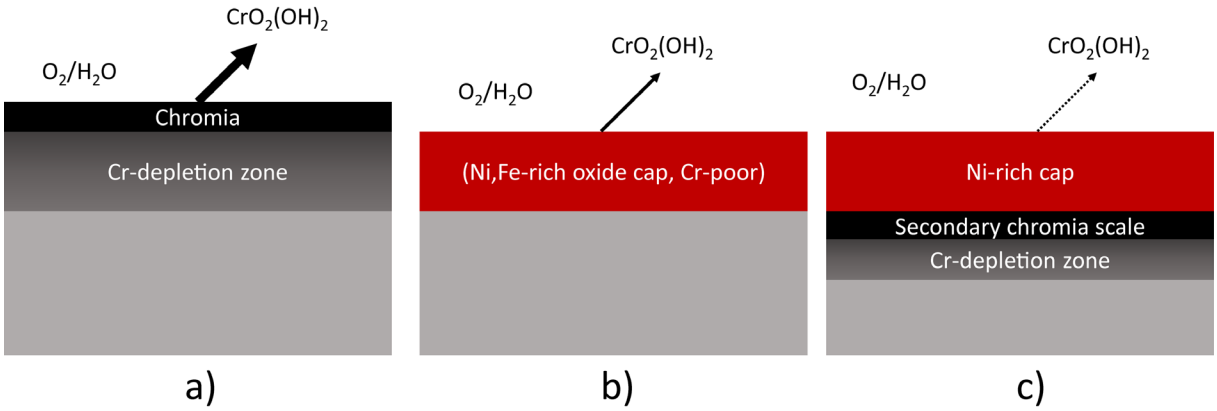

Figure 28 Illustration of the proposed oxidation and evaporation mechanisms. a) The initial chromia is evaporated, with Cr-depletion of the alloy substrate as a consequence. b) The chromia layer breaks down, leading to the oxidation of Ni and Fe, thereby reducing Cr-evaporation. c) The Ni-rich cap-layer is established, minimising Cr evaporation so that a secondary chromia scale can form.

The evolution of the oxide microstructure of Alloy 690 can be compared to that of Alloy 600, which contains significantly less chromium, i.e., about 17 wt.% compared to 30 wt.%. The microstructures of Alloy 600 after exposure in dry air and air + 20% H_2O are shown in Figure 29. In the case of Alloy 600, the initial chromium concentration is too low for a continuous chromia scale to form, and nickel oxidises even in the absence of evaporation of $CrO_2(OH)_2$. This can be seen by observing the oxide scale after exposure in dry air in Figure 29. It is only at the alloy grain boundaries, which provide fast diffusion paths for chromium, that iron and nickel are not oxidised. Since Alloy 600 forms a NiO cap-layer early during the exposure, the rate of evaporation of $CrO_2(OH)_2$ is low (described in **Paper V**). After 168 hours of exposure, a continuous chromia layer is observed at the oxide/metal interface. However, this chromia layer is not considered to be as-protective as the chromia layer formed on Alloy 690 after the triggering of nickel oxidation (as shown in Figure 27).

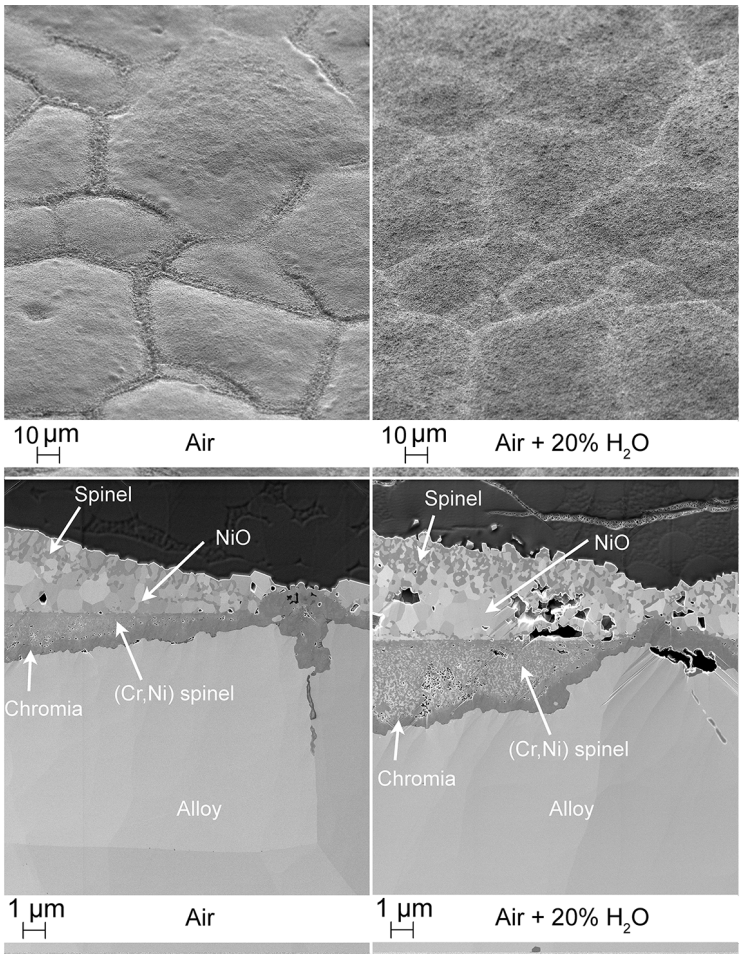

Figure 29 Microstructural SEM-SE images showing Alloy 600 exposed in air and air + 20% H_2O for 168 hours at 800 °C.

9.1.2 ALUMINA-FORMING ALLOYS

Alumina scales often have superior protective properties than chromia scales. However, temperatures higher than 700-800 °C are required for different 'transient' (metastable) alumina phases in the oxide scale to transform into the highly protective α-alumina. At temperatures ≤700 °C, it is unlikely that the transient aluminas will transform into α-alumina. In the present study, the protective properties of different FeCrAl alloys was studied at the temperatures of 600 °C and 800 °C in an oxidising environment, with and without H_2O. The main focus has been on how the 'lean' FeCrAl alloy EF101, which is alloyed with silicon behaves in oxidising environments. This has been compared to the behaviour of Alkrothal 14, which is richer in chromium and aluminium but is not alloyed with silicon.

9.1.2.1 OXIDE SCALE FORMATION AT 800 °C

The oxide microstructures of EF101 after exposures in dry and wet (40 vol.% H_2O) air at 800 °C are presented in Figure 30. In all the cases, the oxide scale consisted of a dense inner layer and a more porous outer layer. The interface between the inner and outer layer is represented by dashed lines in the images. The duplex nature of the alumina scale is in accordance with

the findings of previous studies regarding the oxidative behaviours of FeCrAl alloys in similar environments [89, 156]. In those studies, the inner layer was suggested to be inward-growing α-alumina, and the outer layer was proposed to be outward-growing γ-alumina. Furthermore, in the present work, a slightly thicker oxide is observed after exposure in wet air compared to dry air, which is in accordance with an earlier study that attributed this effect to the stabilisation of γ-alumina by water, with the latter phase growing faster than the α-alumina [156].

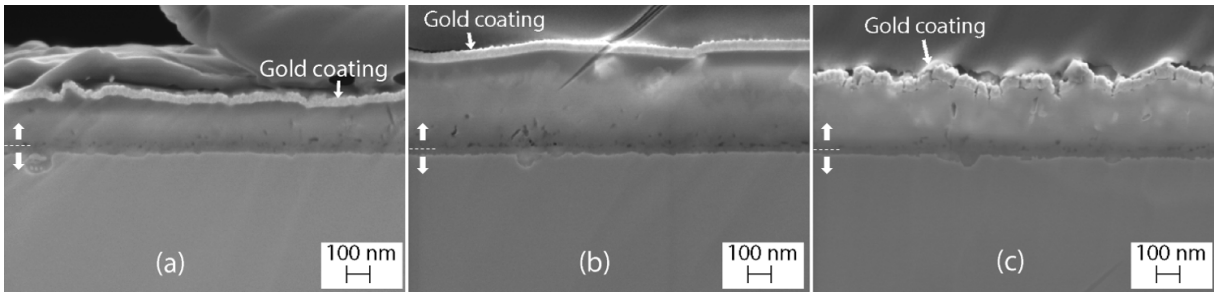

Figure 30 Cross-sectional images of EF101 after exposure at 800 °C in: a) wet air for 20 hours b) wet air for 200 hours; and c) dry air for 200 hours. Dashed lines indicate the interface between the inner layer and the outer layer of the oxide scale.

More detailed microscopy was performed to elucidate the role of silicon in scale formation. Figure 31 shows STEM images and line-scans of the oxide scales formed on EF101 after 1, 20 and 200 hours. It is clear that the oxide scales contain high levels of silicon, together with aluminium. Silicon is enriched in the outer part of the scale, while aluminium dominates in the inner part of the scale. The tendency for silicon and aluminium to segregate into the upper and lower parts of the scale, respectively, becomes more marked with time. After 200 hours, relatively pure silica is observed in the outer part, while the inner part of the scale consists of pure alumina. This evolution is reasonable as there is very little mutual solubility between SiO_2 and Al_2O_3, and because Al_2O_3 is stable at lower oxygen activity than silica, as shown in Figure 11. In the image of the cross-section obtained after 20 hours (Figure 31), a needle-shaped feature rich in iron can be observed. This is attributed to an unidentified crystalline oxide phase.

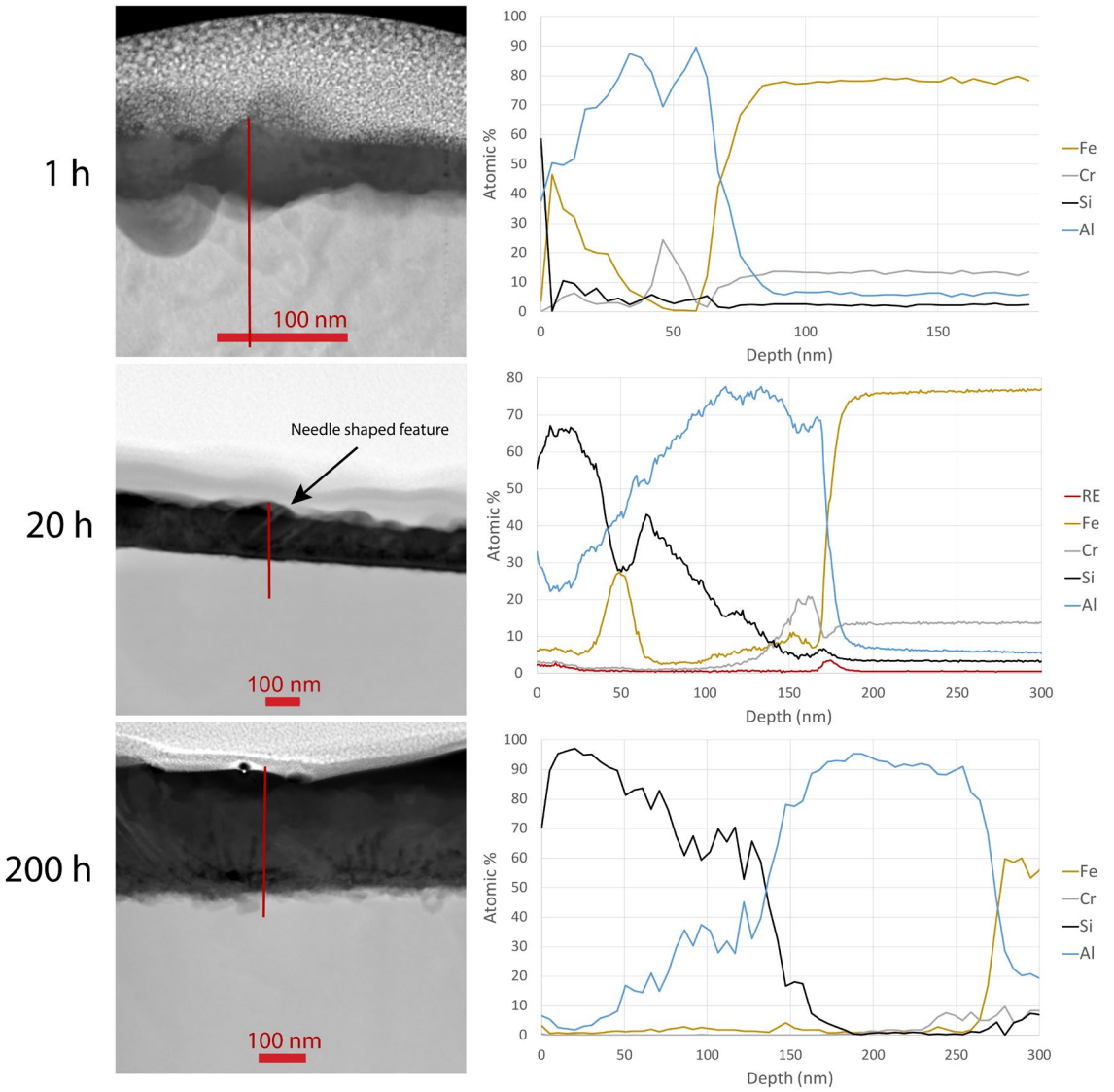

Figure 31 STEM images and line-scans of EF101 samples exposed to wet air for 1, 20 and 200 hours at 800 °C. The line-scans show the cation concentrations through the oxide, indicating a high level of aluminium, together with silicon.

To verify that the high level of silicon observed in the scale by STEM is representative of the entire scale, approximately 0.15 mm^2 areas were subjected to plan-view SEM-EDS analysis. By lowering the acceleration voltage, and thereby decreasing the interaction depth, it was possible to identify a strong signal for silicon at the lowest acceleration voltage of 5 kV, see Figure 32. This confirms the presence of a high concentration of silicon in the scale. Interestingly, silicon was only observed after exposure in wet air, and not after exposure in dry air. Moreover, silicon was not detected in the scale formed on Alkrothal 14 that was exposed in wet air. The latter alloy contains much less silicon than EF101 (see Table 1). This confirms that the silicon detected in the scale of EF101 originates from the alloy itself and do not arise from contamination from the quartz reactor tube used for the exposure.

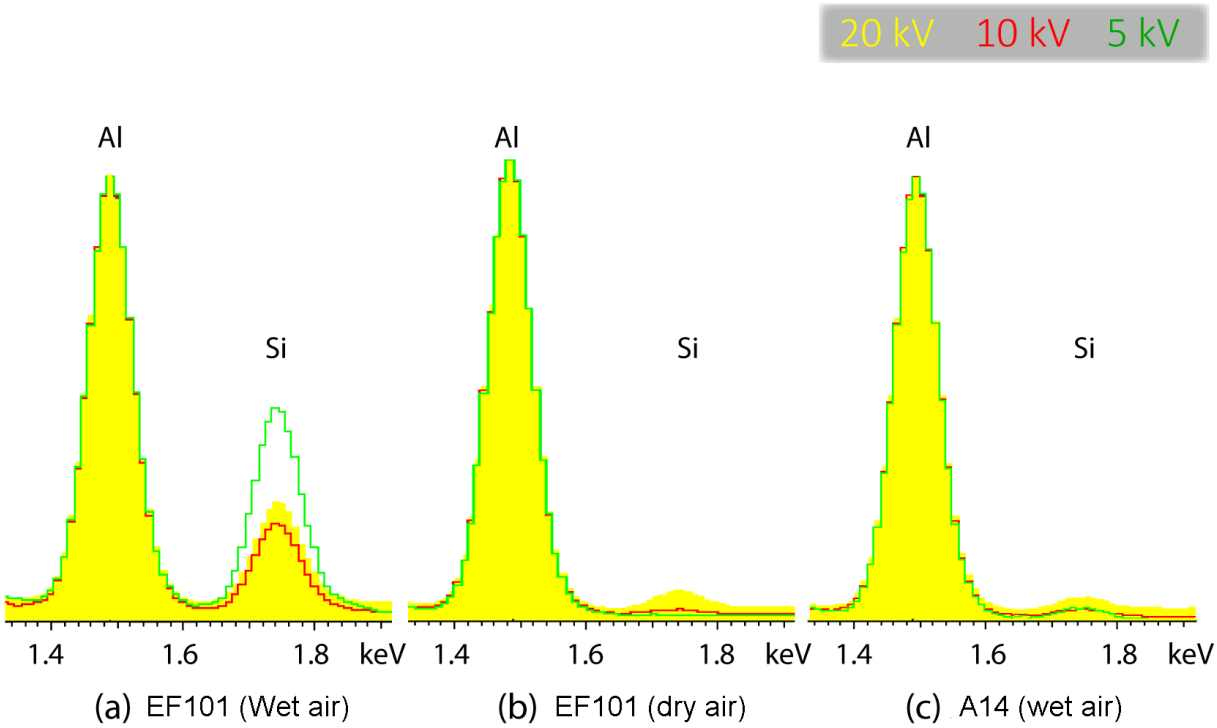

Figure 32 SEM-EDS examination of the top-views of samples of: a) EF101 exposed in wet air for 200 hours b) EF101 exposed in dry air for 200 hours; and c) Alkrothal 14 (A14) exposed in wet air for 200 hours, all at 800 °C. The two peaks indicate the intensities for aluminium and silicon normalised to aluminium for three different acceleration voltages: 5 kV, 10 kV, and 20 kV.

GI-XRD measurements were performed on the two alloys (EF101 and A14) from both the wet air and dry air exposures, to identify crystalline phases in the oxide scales, see Figure 33. The diffractograms for A14 exposed in wet and dry air, as well as for EF101 exposed in dry air are all similar, indicating that the scale consists of α-alumina and γ-alumina. The diffractogram for EF101 exposed in wet air is different. Thus, in addition to diffraction peaks for α-alumina and γ-alumina, there are additional peaks in the 2θ interval of 15-42°. These additional peaks can be assigned to two phases: mullite ($Al_2(Al_{2+2x}Si_{2-2x})O_{10-x}$) and tridymite ($SiO_2$). Some unidentified peaks were also obtained. Both mullite and tridymite are usually formed at temperatures higher than 800 °C. The mechanisms for the formation of these phases in the presence of oxygen and water vapour are not known.

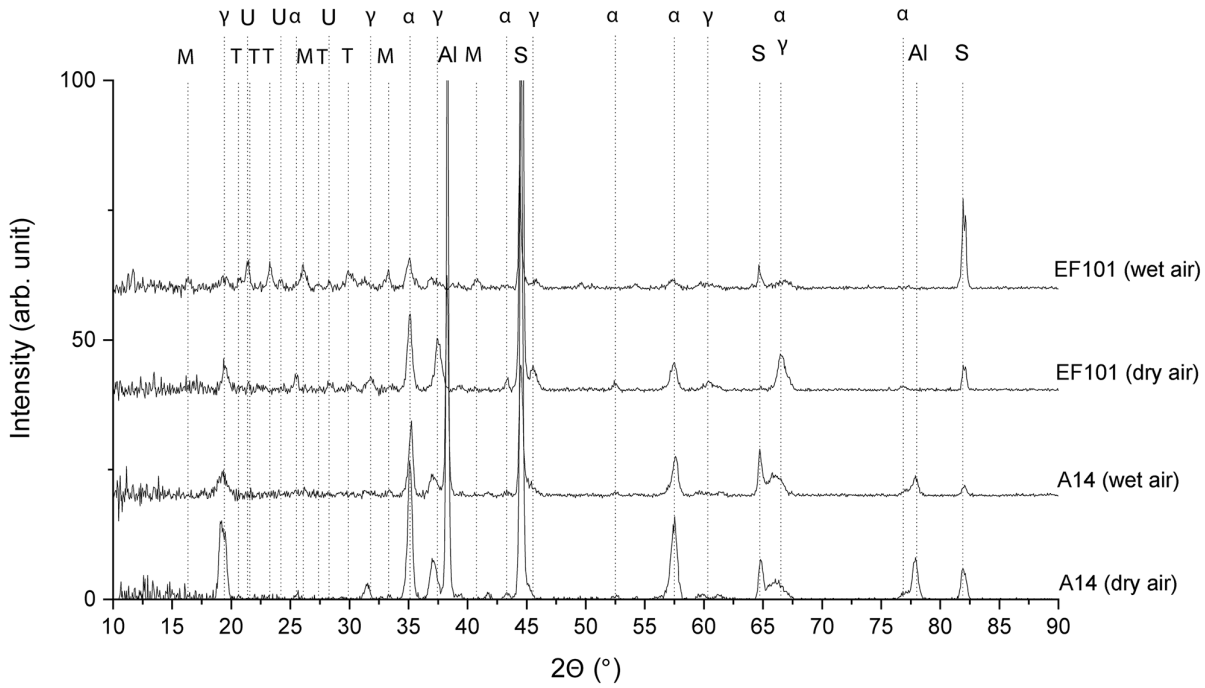

Figure 33 XRD patterns of the A14 and EF101 coupons exposed in dry and wet air at 800 °C. The peaks are labelled as follows: (M) mullite, (T) tridymite, (Al) metallic aluminium from the mounting of the specimen, (S) substrate, (γ) γ-alumina, (α) α-alumina, (U) unidentified peak.

9.1.2.2 Oxide formation at 600 °C

The relatively low temperature of 600 °C prevents the transient aluminas from transforming into α-alumina, so the alloy relies on the protective properties of these transient aluminas to avoid rapid oxidation of Fe-oxides. The establishment of transient alumina scales can be hindered by evaporation of $CrO_2(OH)_2$, as reported in an earlier study [17]. EF101 has a relatively low chromium concentration but it contains silicon, which has been observed to facilitate the formation of a protective transient alumina scale [17]. To examine if EF101 can form a protective transient alumina scale, exposures were performed in air and air + 40% water at 600 °C. The results (see **Paper II**) show that EF101 is able to form a protective transient alumina scale at 600 °C. Thus, rapid growth of Fe-oxides only occurs at a few surface sites, always close to RE-particles, see Figure 34 where the dark area around the bright RE-particles consists of Fe-oxide. The nodules formed in both dry and wet air but were slightly more frequent in wet air. It can also be observed in Figure 34 that the Fe-oxide nodules are of similar size after 20 hours and 200 hours. This indicates that the nodules form during the early stage of oxide formation, and that no further growth occurs after 20 hours. This is probably due to the formation of a healing alumina layer at the alloy/nodule interface. Figure 35 presents one of these Fe-oxide nodules after exposure in air + 40% water vapour for 200 hours, whereby an Al-rich oxide can be observed at the alloy/nodule interface. Figure 35 also shows the base oxide, which was too thin to be subjected to further examination.

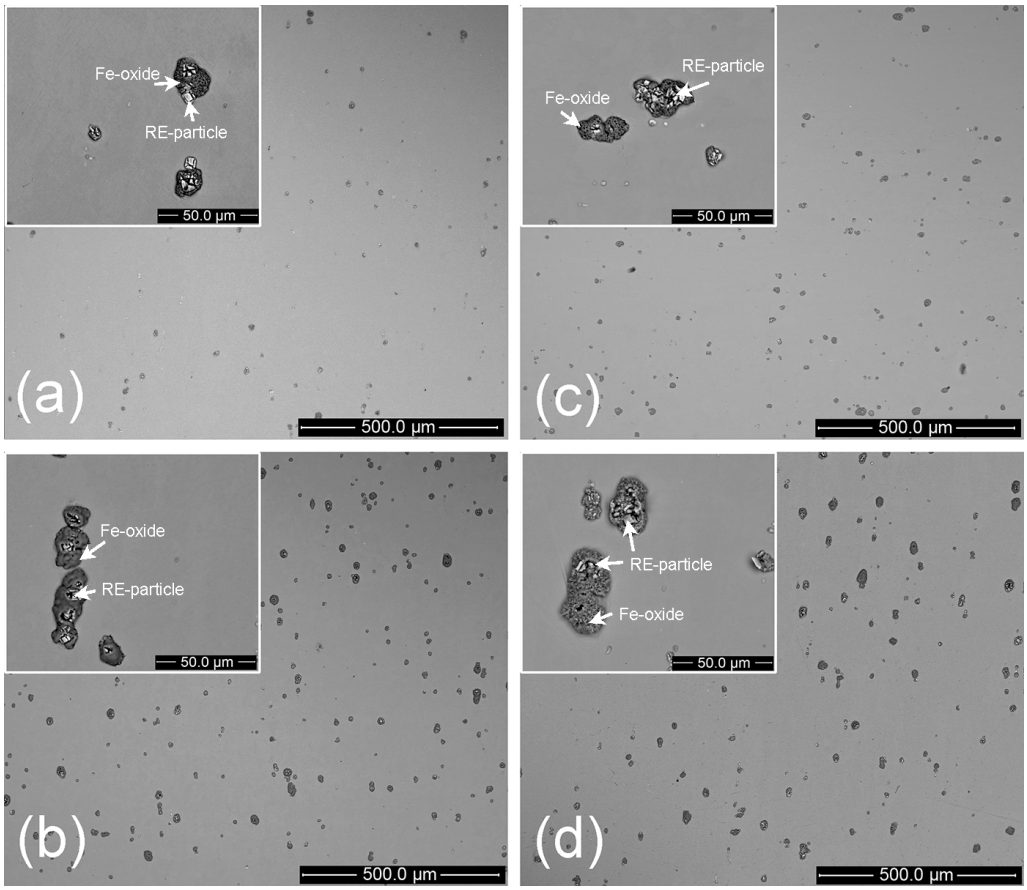

Figure 34 Top-view images of EF101 samples exposed at 600 °C to: **a)** dry air for 20 hours; **b)** wet air for 20 hours; **c)** dry air for 200 hours; and **d)** wet air for 200 hours.

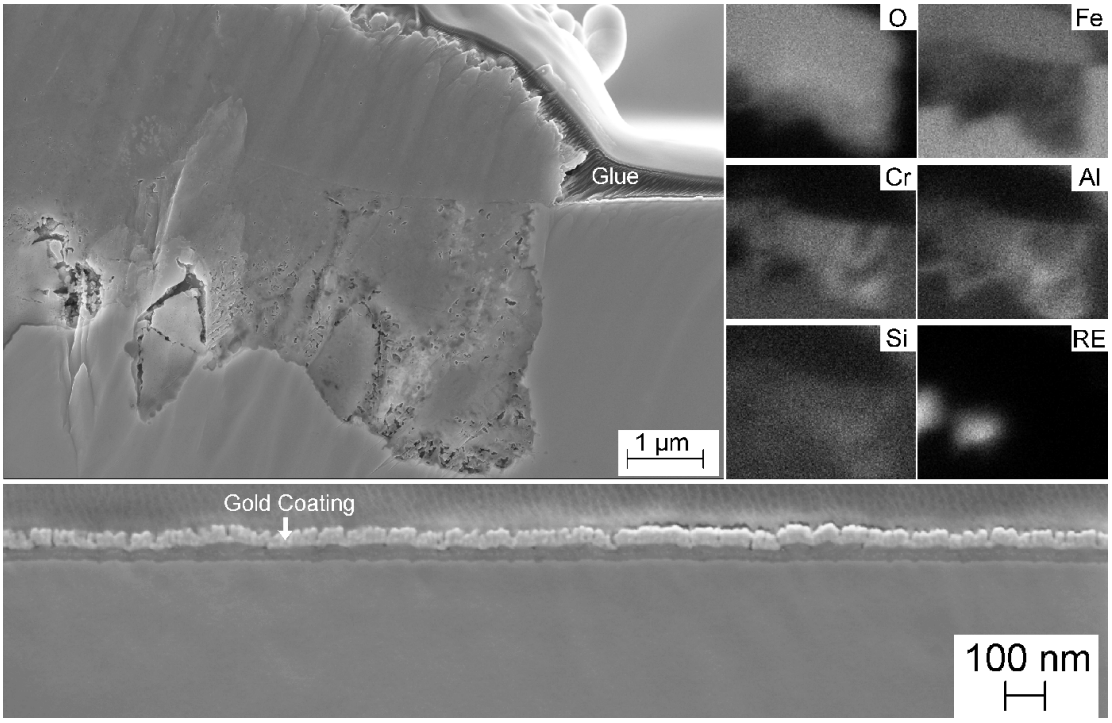

Figure 35 Cross-sectional image showing EF101 after exposure in wet air for 200 hours at 600 °C. The top image shows the area at a Fe-oxide nodule. The lower image shows the base oxide.

9.1.2.3 *Evaporation of chromium*

Alumina-forming alloys are expected to experience low levels of chromium evaporation due to the low concentration of chromium in the outer part of the oxide scale. Using the 'denuder' technique, the levels of Cr-evaporation from two alumina-forming FeCrAl alloys were measured. The alloys studied were A14 and the Si-containing EF101. The results, which are presented in Figure 36, show that both FeCrAl alloys exhibit low but measurable levels of Cr-evaporation. It can be seen that EF101 exhibits lower Cr-evaporation than A14. It is suggested that in the case of EF101, the presence of silica in the scale reduces the rate of transport of chromium ions across the scale.

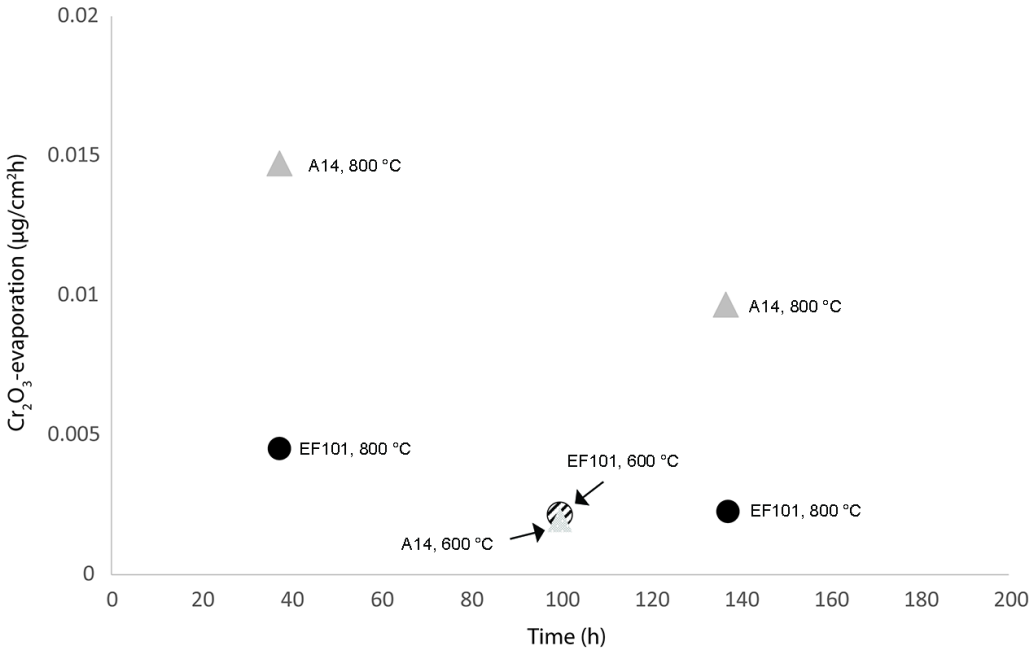

Figure 36 Chromium evaporation rate as a function of time during exposure in air + 40% H_2O. The gas flow velocities were 11.8 cm/s at 800 °C and 9.8 cm/s at 600 °C.

9.2 Low oxygen activity and high water concentration

Exposures were performed at low oxygen activity in a mixture of water vapour (20%) and H_2 (20%) in argon at 800 °C. In this environment, water is the only oxidant and not all of the oxides that can be formed by the alloy components are stable; for instance, the different Fe-oxides and NiO do not form spontaneously under these conditions (see Figure 11). Figure 37 shows the microstructures following the exposure of alloys 310H, 600, EF101 and APTM for 168 hours at 800 °C in this environment (for a more comprehensive description, see **Paper V**). The results show that 310H suffers relatively rapid oxidation with signs of break-away of the protective Cr-rich oxide scale. This can be compared to the corresponding experiment performed in air, where the oxidation rates are lower. Higher oxidation rates when H_2O is the oxidant rather than O_2 have been reported previously [97, 99, 119], although the underlying mechanisms are unclear. A possible explanation for this could be hydrogen pick-up by the

material. It has been proposed that hydrogen reduces chromium diffusivity along the alloy grain boundaries, thereby retarding the supply of chromium to the oxide scale and impairing the formation of a protective chromia scale [125].

For Alloy 600, on the other hand, the oxidation rate is lower in the 20% H_2O + 20% H_2 + Ar environment than in air. This is suggested to be due to the fact that NiO forms spontaneously in air. The presence of a NiO external layer in contact with the alloy results in a higher oxygen solubility in the alloy and a faster oxidation rate [157]. In the 20% H_2O + 20% H_2 + Ar environment, NiO does not form, which means that a protective chromia scale is able to form, resulting in a lower oxidation rate.

The FeCrAl alloys that were exposed in this environment all formed continuous alumina scales. The alumina scales formed were about twice as thick as those formed after exposure to high-oxygen activity environments. A possible explanation for this is the mechanism described earlier [57], which proposed that in the presence of water with no oxygen, water is transported through the alumina scale by hydroxides in the alumina grain boundaries, resulting in a faster oxidation rate.

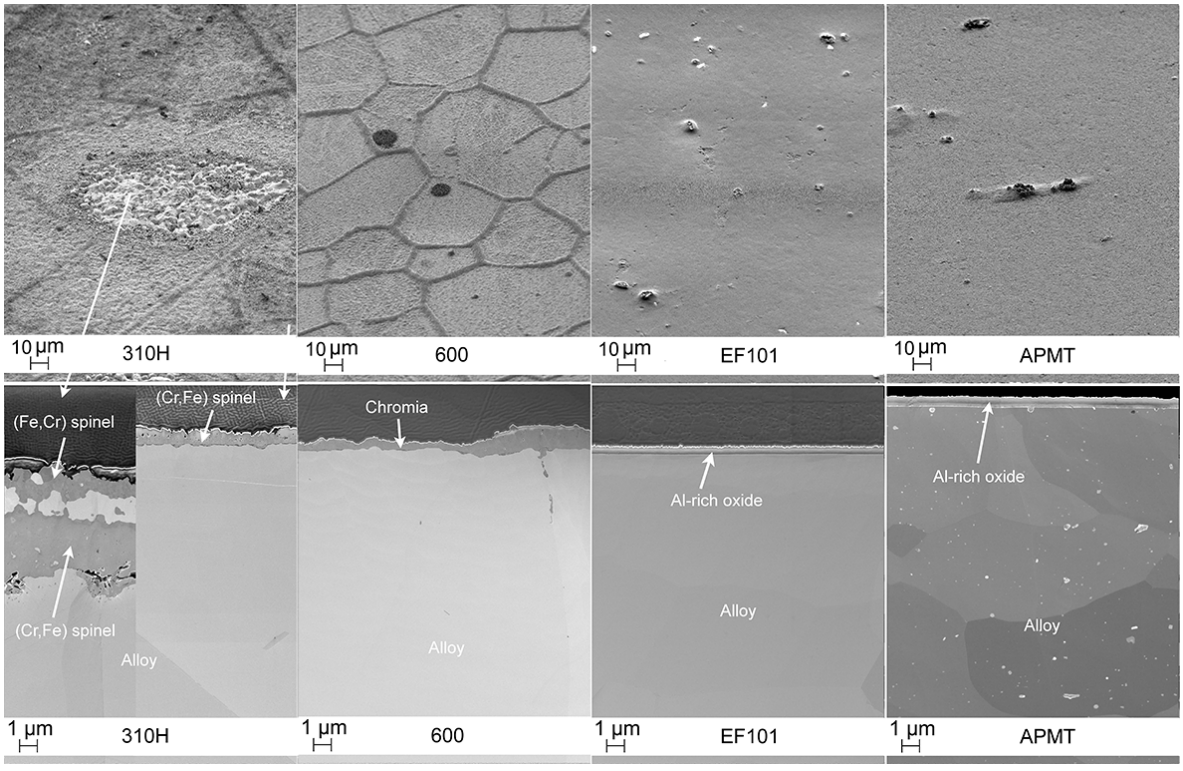

Figure 37 SE-SEM images showing Alloys 310H, 600, EF101 and APMT exposed in 20% H_2O + 20% H_2 + Ar at 800 °C for 168 hours.

9.3 Low oxygen activity and high nitrogen concentration

If the oxygen activity is even lower than the level described in Section 9.2, it might be insufficient for chromia scale formation. A chromia-forming alloy that is lacking a protective

oxide for this reason readily reacts with other elements present in the environment. Thus, if the activity of nitrogen is high, nitrogen enters the alloy and nitride precipitates can form. In contrast, the presence of an oxide scale is expected to decrease the rate of nitridation. The degree of nitrogen pick-up by the alloy depends on the oxide scale formed and the chemical composition of the alloy.

9.3.1 Nitridation in the presence of an oxide scale

By performing exposures in environments that contain 95% N_2 and 5% H_2 and two slightly different concentrations of H_2O at 900 °C, it was possible to obtain two very similar environments. In one of these, chromia formed spontaneously (Environment H) but not in the other (Environment L), see Figure 38 and Table 2 for more detailed exposure conditions. Through this small variation of H_2O content it was possible to study how effective a chromia scale is at preventing nitridation.

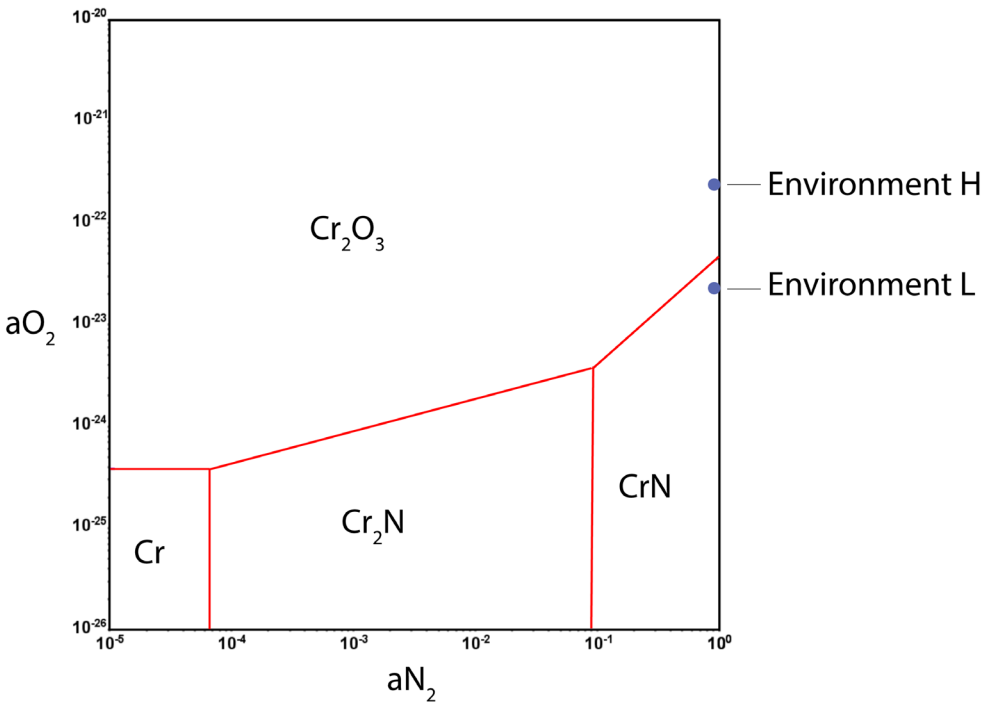

Figure 38 Cr, N, O stability diagram at 900 °C. The positions of Environment H and Environment L are indicated.

Figure 39 shows five chromia-forming austenitic alloys and one alumina-forming ferritic alloy after 168 hours of exposure in Environment H at 900 °C. All the alloys formed continuous external oxide scales in this environment. The austenitic alloys have all formed chromia scales. The two Si-containing 'MA'-alloys have additionally formed silica layers at the metal/oxide interface. In the case of 253 MA, the silica layer is continuous, while it is discontinuous for 353 MA. For 353 MA, a layer of metal is present between the chromia and the silica layers. In all the austenitic alloys, precipitates of Cr_2N are observed, indicating that nitrogen has

penetrated the oxide scale. The alumina-forming alloy EF101 has formed an external alumina scale, and no nitrides are observed in the metal. See **Paper III** for more details of the results.

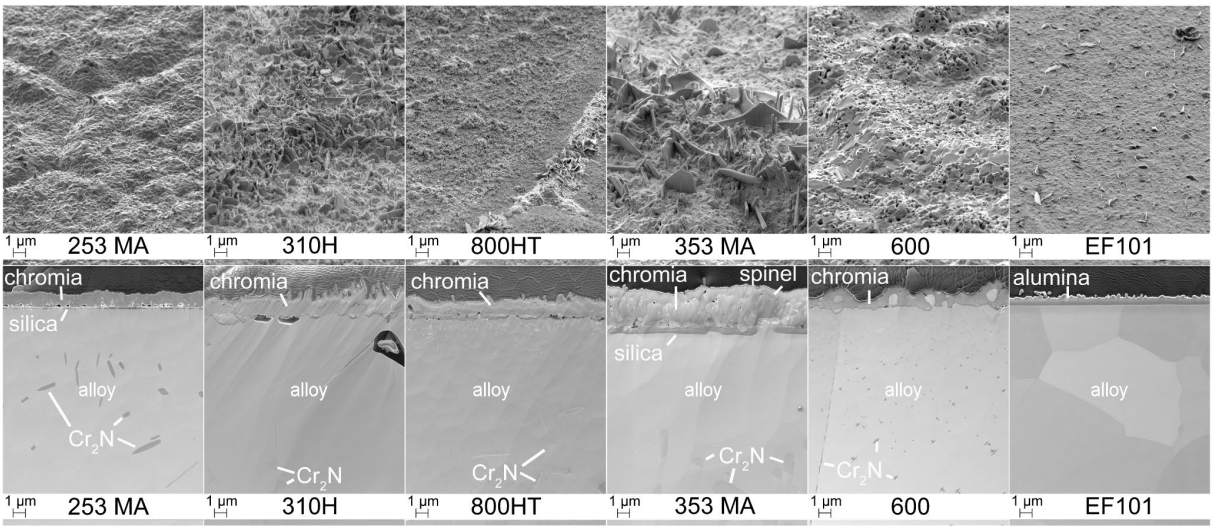

Figure 39 SEM-SE images showing a 50° tilted top-view (top) and cross-sectional view (bottom) of the six alloys exposed for 168 hours at 900 °C in Environment H.

Figure 40 shows the same alloys after exposure in Environment L for 168 hours at 900 °C. In this case, no chromia scale is detected on the alloy surfaces. The only surface oxides are discontinuous silica layers for 253 MA and 353 MA, and an alumina scale for EF101. All the austenitic alloys show nitride precipitates, both on the alloy surface and within the metal. The extent of nitride precipitation observed after exposure is much greater in Environment L than in Environment H. For the alumina-forming alloy EF101, a continuous external alumina scale is present on the alloy surface and no nitride precipitates are observed in the metal, indicating that the alumina scale has prevented nitridation. This is in line with previous studies that have reported that alumina is not permeable to nitrogen [14, 144].

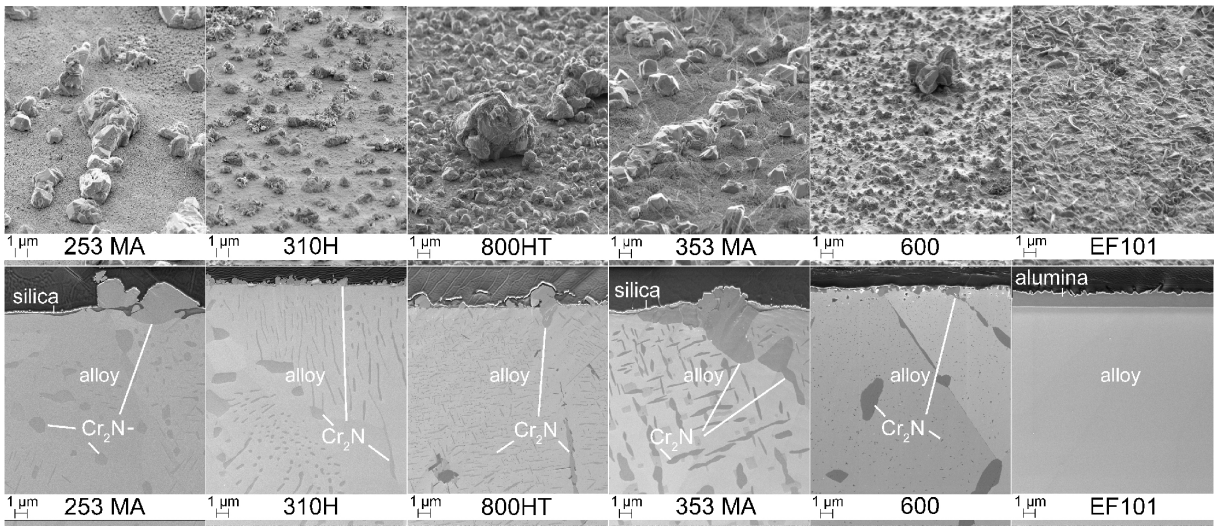

Figure 40 SEM-SE images showing a 50° tilted top-view (top) and cross-sectional view (bottom) of the six alloys exposed for 168 hours at 900 °C in Environment L.

The mass changes due to oxidation and nitridation during the exposures are presented in Figure 41. In Environment L, the only substantial mass gain due to oxidation is registered for EF101, which forms an alumina scale. For the other alloys, the mass gain is the result of nitridation (except for the small mass gains due to silica formation seen for 253 MA and 353 MA). A clear trend can be observed in that the alloys with higher nickel content show lower mass gains due to nitridation. This is in agreement with previous studies [129], and is likely an effect of the reported decrease in the solubility of nitrogen with increasing nickel concentration [128]. In contrast, the mass gain due to oxidation was substantial in Environment H. By calculating the mass change due to oxidation and subtracting that from the total mass change, the mass gain due to nitridation can be compared to the corresponding value in Environment L, see Table 3. Table 3 also shows a calculation of the reduction in nitridation caused by the presence of a chromia surface layer, by comparing the net nitrogen pick-up in the two environments. The reduction of nitridation is in the range of 65-91%. The results indicate that an oxide scale consisting of both chromia and silica layers, as in the case of the two 'MA'-alloys, provides a better barrier to nitridation than when chromia is present by itself. The alumina-forming alloy EF101 shows no sign of nitridation in the two environments, with all of the mass gain being assigned to the formation of external alumina scales. The small difference in mass gain between the two environments is believed to be due to subtle variations in the exposure conditions.

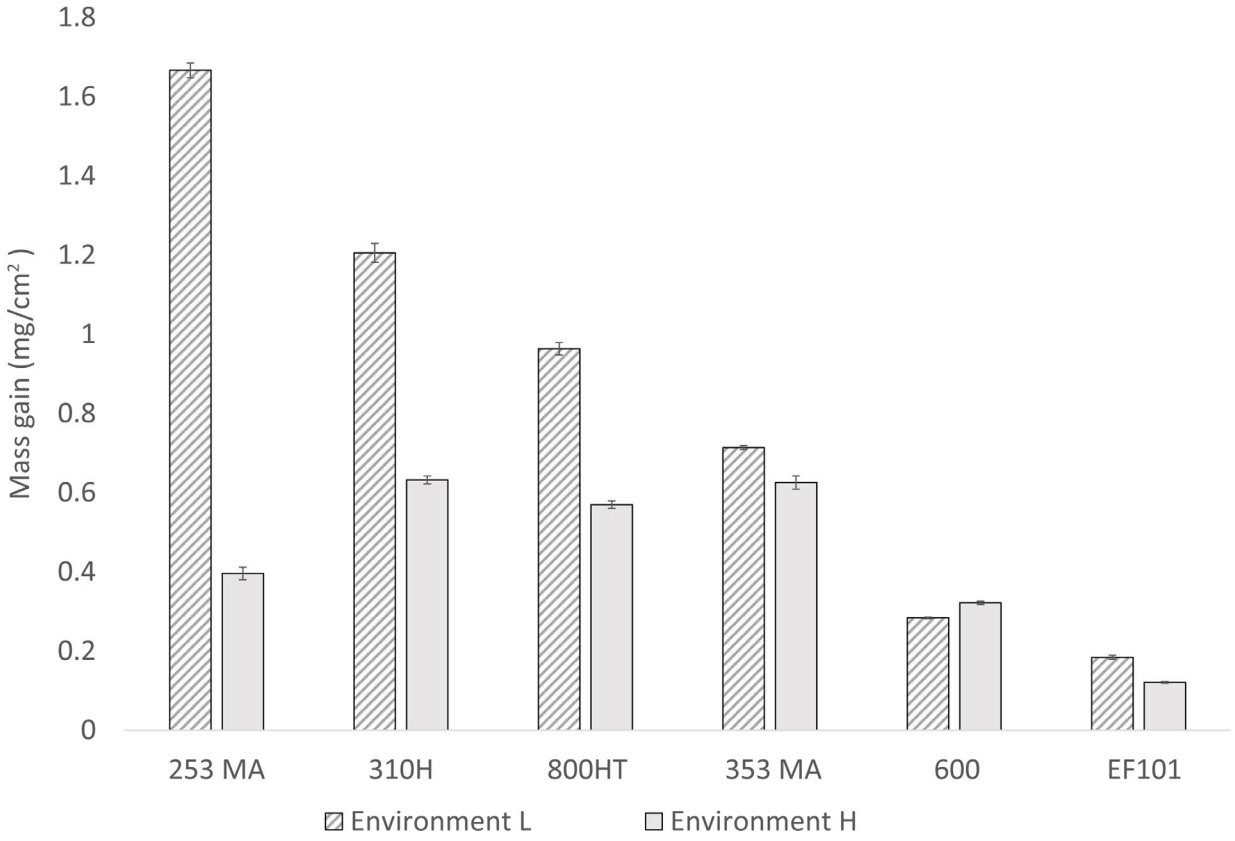

Figure 41 Mass gains of the six alloys after exposure for 168 hours at 900 °C in Environment L and Environment H. The nickel concentration in the alloy increases from left to right for 253 MA, 310H, 800HT, 353 MA and 600.

Table 3 Measured mass gains and the mass gains attributed to oxygen in the oxide scale (calculated from the measured scale thickness) for the six alloys after exposure in the two environments. The nitrogen pick-up equals the total mass gain minus the mass of oxygen in the oxide layer. The decrease in nitrogen pick-up due to the presence of a surface chromia layer is also presented.

	Environment L (mg/cm^2)			**Environment H (mg/cm^2)**			**Reduction in nitrogen pick-up in Environment H**
Alloy	Measured mass gain	Mass of oxygen in oxide	Nitrogen pick-up	Measured mass gain	Mass of oxygen in oxide	Nitrogen pick-up	
253 MA	1.667	0.03	1.64	0.396	0.19	0.21	87%
310H	1.205	0	1.21	0.632	0.22	0.41	66%
800HT	0.963	0	0.96	0.570	0.26	0.31	68%
353 MA	0.713	0.03	0.68	0.626	0.57	0.06	91%
600	0.284	0	0.284	0.322	0.22	0.10	65%
EF101	0.184	0.23	0	0.120	0.13	0	n/a

Samples that were exposed in the two different environments were further examined by GD-OES, in order to obtain the nitrogen profiles into the alloys, see Figure 42. With the exception of EF101, all of the alloys exhibited higher concentrations of nitrogen and greater nitridation depth after exposure in Environment L, as compared to exposure in Environment H. This is in

good agreement with the gravimetric results shown in Table 3. As expected, the GD-OES analysis showed no evidence of nitridation of the alumina-forming alloy EF101 in either of the two environments. The GD-OES nitrogen profiles were integrated to compare the levels of nitrogen in the alloys after exposure in the two environments. The results are presented in Table 4 as the reduction of nitridation caused by the presence of an external chromia layer. The results are in good agreement with the gravimetric results, showing a reduction in the range of 50-95%. Similar to the gravimetric results, the GD-OES analysis showed a greater reduction of nitridation for the two 'MA'-alloys than for the chromia-forming alloys. This indicates that a duplex scale, consisting of an outer layer of chromia and inner silica layer, is more efficient at preventing nitridation than a single chromia scale. The observation that alloy 253 MA underwent significant nitridation in Environment L, where a silica layer was detected, indicates that a single silica layer does not protect against nitridation. In the case of 253 MA exposed in Environment H, where a chromia layer was sitting directly on a continuous silica layer, the chromia scale contained a significant number of pores and some spallation of the chromia was observed, indicating poor adherence between the silica and chromia scales. This is in agreement with the results of previous studies [158].

EF101 forms continuous alumina scales in both environments, showing no evidence of nitridation. In previous studies of alumina forming-alloys at 900 °C, it has been observed that alumina is impermeable to nitrogen, and that nitrogen pick-up in FeCrAl-alloys occurs in areas where the alumina is not continuous, for instance at large RE inclusions [144]. The lack of evidence of nitrogen pick-up by EF101 in this thesis, therefore, indicates that the alloy has formed a continuous alumina scale with no macro defects that would allow nitrogen to enter the alloy. The alumina barrier layer evidently formed during the nitriding exposure, with the source for oxygen being the traces of water present in the gas. The lack of evidence of nitrogen ingress also means that, in spite of the scarcity of water (10 ppm), the protective alumina layer must have formed in the early stages of the experiment. The present results are in line with **Paper V** in which three FeCrAl alloys, APMT, EF101 and EF100, were subjected to a strongly nitriding environment at 800 °C. A microstructural investigation showed a number of large RE particles (>5μm) in APM, while no such large particles were detected in EF101 or EF100. The study showed that APMT suffered local nitridation, while EF100 and EF101 showed no signs of nitridation.

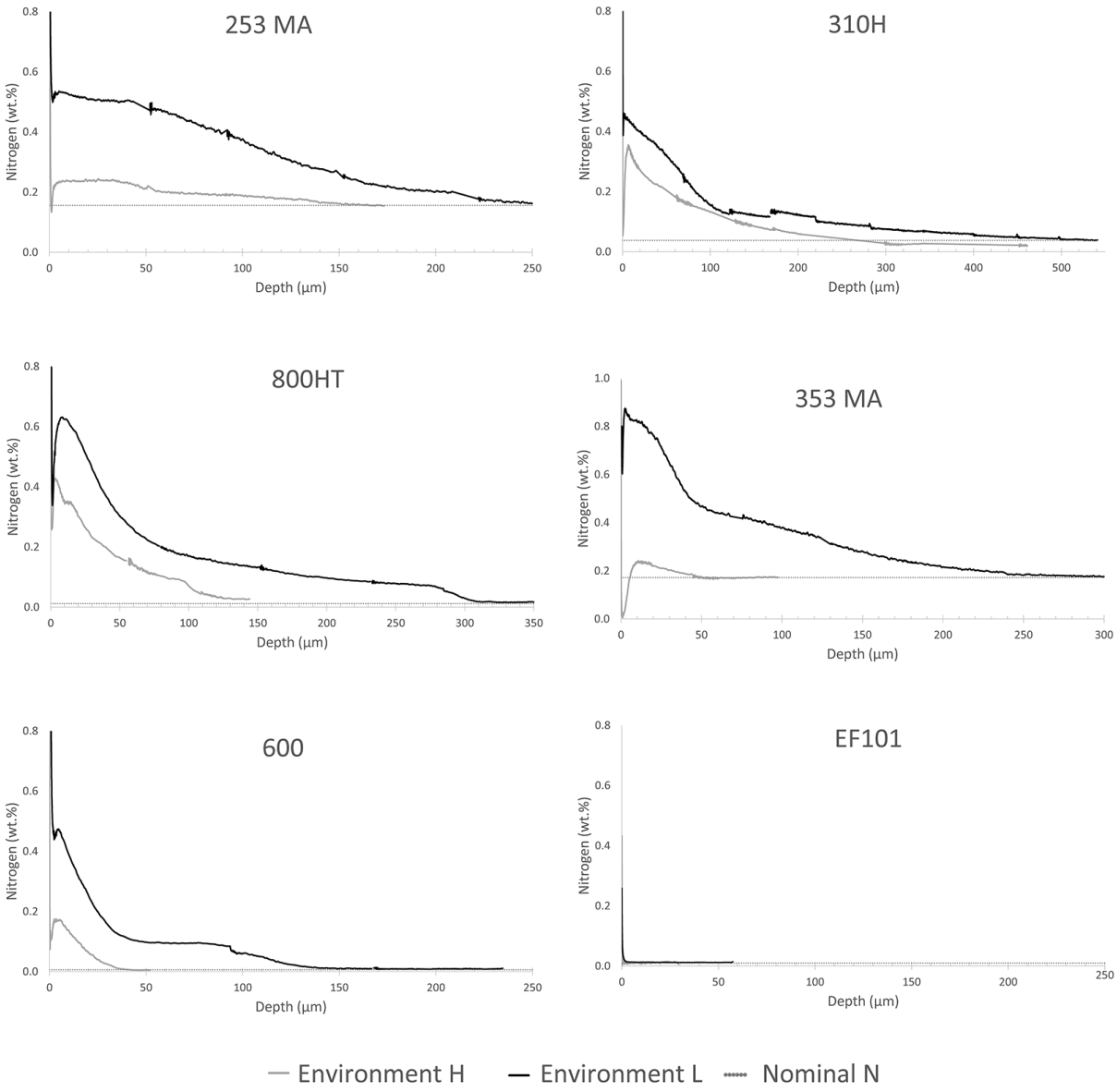

Figure 42 GD-OES nitrogen depth profiles after exposures for 168 hours in Environment H and L at 900 °C, plotted together with the nominal nitrogen concentration. Note that the absolute depth of analysis may be 2-4 times greater than the indicated depth.

Table 4 Relative reduction of nitrogen pick-up in Environment H compared to Environment L, from the GD-OES analysis.

	Reduction in nitrogen pick-up measured by GD-OES
Alloy	
253 MA	83%
310H	50%
800HT	61%
353 MA	95%
600	75%
EF101	n/a

The results show that the presence of a surface chromia layer decreases alloy nitridation and that chromia is permeable to nitrogen. However, it is not clear how nitrogen penetrates the chromia scale. The formed chromia scales were continuous with no macro defects being observed, indicating that nitrogen penetrates the chromia scale itself. In an attempt to detect nitrogen in the oxide scale, an APT study was performed on Alloy 600 that was exposed in Environment H at 900 °C for 168 hours. The results of this examination are presented in Figure 43, together with an image of the oxide scale and an indication of the position in the scale of the APT specimen. The APT measurement shows an area with multiple chromia oxide grains and one spinel oxide grain ($MnCr_2O_4$). Nitrogen was detected in the spinel grain, and quantification indicated a nitrogen concentration of >200 at. ppm. In contrast, nitrogen was not detected in the chromia oxide grains or in the corresponding grain boundaries. The APT study also showed that titanium segregates and diffuses along the oxide grain boundaries.

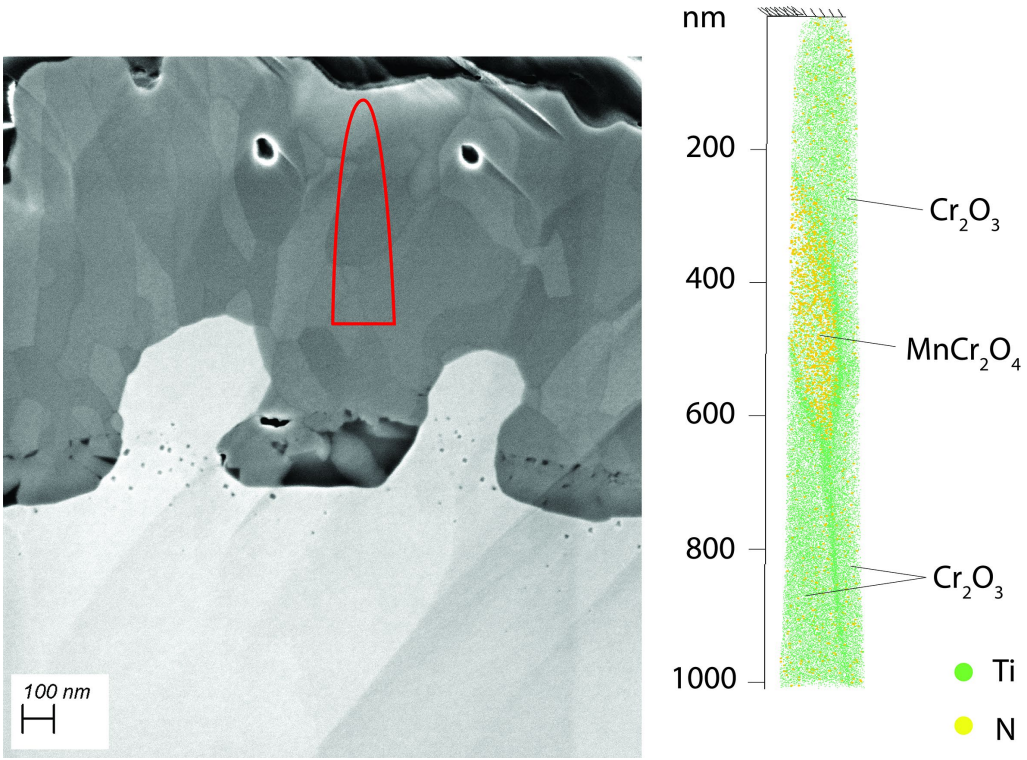

Figure 43 APT examination of the oxide scale formed on Alloy 600 after exposure in Environment H at 900 °C for 168 hours. The left SEM-SE image shows the oxide scale and indicates (red area) from where the APT specimen was extracted. The right-hand side of the figure shows the results of the APT measurements.

9.3.2 Time-resolved study of nitridation at 1100 °C

Exposures at 1100 °C were performed to study the kinetics of nitridation and the situation when nitridation reaches equilibrium. The oxygen activity during the exposure was too low ($4*10^{-21}$) for chromia to form. Three exposure times were used: 1 day (24 hours), 1 week (168 hours), and 3 weeks (504 hours). The results are described in detail in **Paper IV.** The mass gains after exposures are presented in Figure 44. It is noteworthy that the mass gains of both 253

MA and Alloy 600 stay constant between 1 week and 3 weeks of exposure. This indicates that the nitridation of the alloys has reached equilibrium already after 1 week. For 353 MA, a small increase in mass is observed between 1 week and 3 weeks of exposure, implying that, in this case, nitridation has not reached equilibrium after one week. The slower attainment of equilibrium is attributed to the higher concentration of chromium in 353 MA, as compared to 253 MA and Alloy 600. This allows for the formation of more chromium nitride precipitates in 353 MA. In addition, during the initial 24 hours of exposure, the nitridation rate is highest for 253 MA. This is in agreement with the results of a previous study [129], and is attributed to the comparatively low concentration of nickel in this alloy, which facilitates higher nitrogen solubility and faster diffusion into the sample interior.

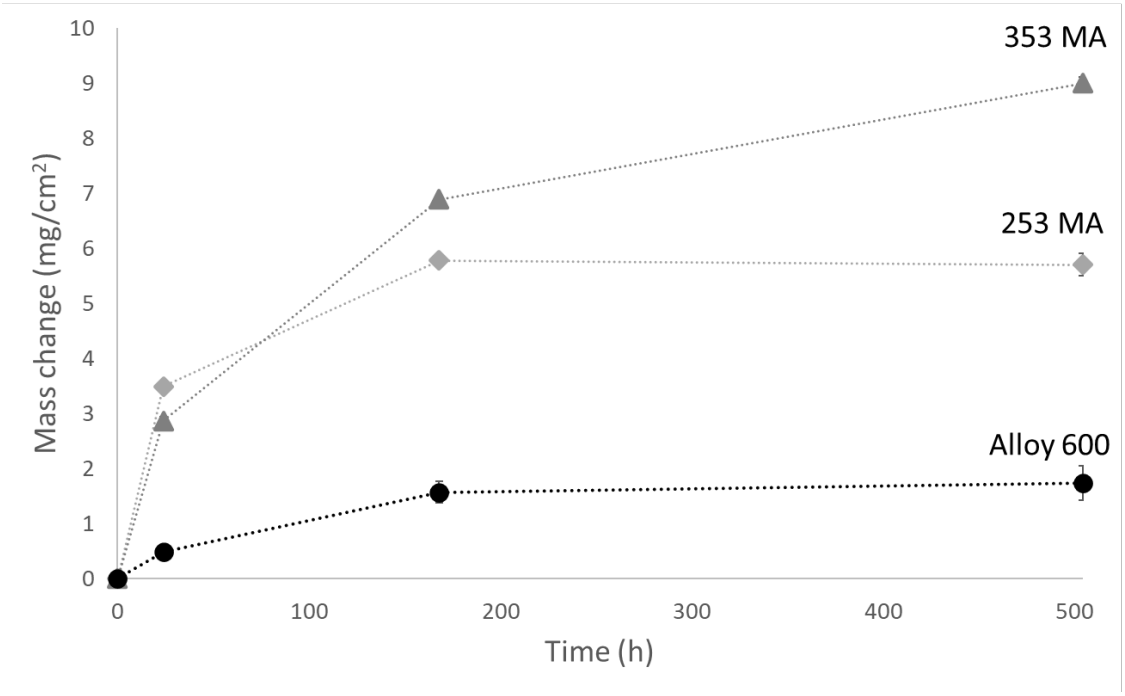

Figure 44 Mass change due to nitrogen pick-up as a function of exposure time in a nitriding environment at 1100 °C.

Figure 45 shows cross-sections and EPMA line-scans through the sample thickness of 353 MA coupons after 1 week and 3 weeks of nitridation. In agreement with the gravimetric data in Figure 44, the EPMA results show that equilibrium is not reached after 1 week. However, the flat nitrogen and chromium profiles acquired after 3 weeks indicate that nitridation has reached equilibrium at this stage. At equilibrium, the chromium concentration measured in the solid solution is 14.6 at.%, corresponding to 13.7 wt.%, while the nitrogen concentration is 0.26 at.%, corresponding to 0.066 wt.%.

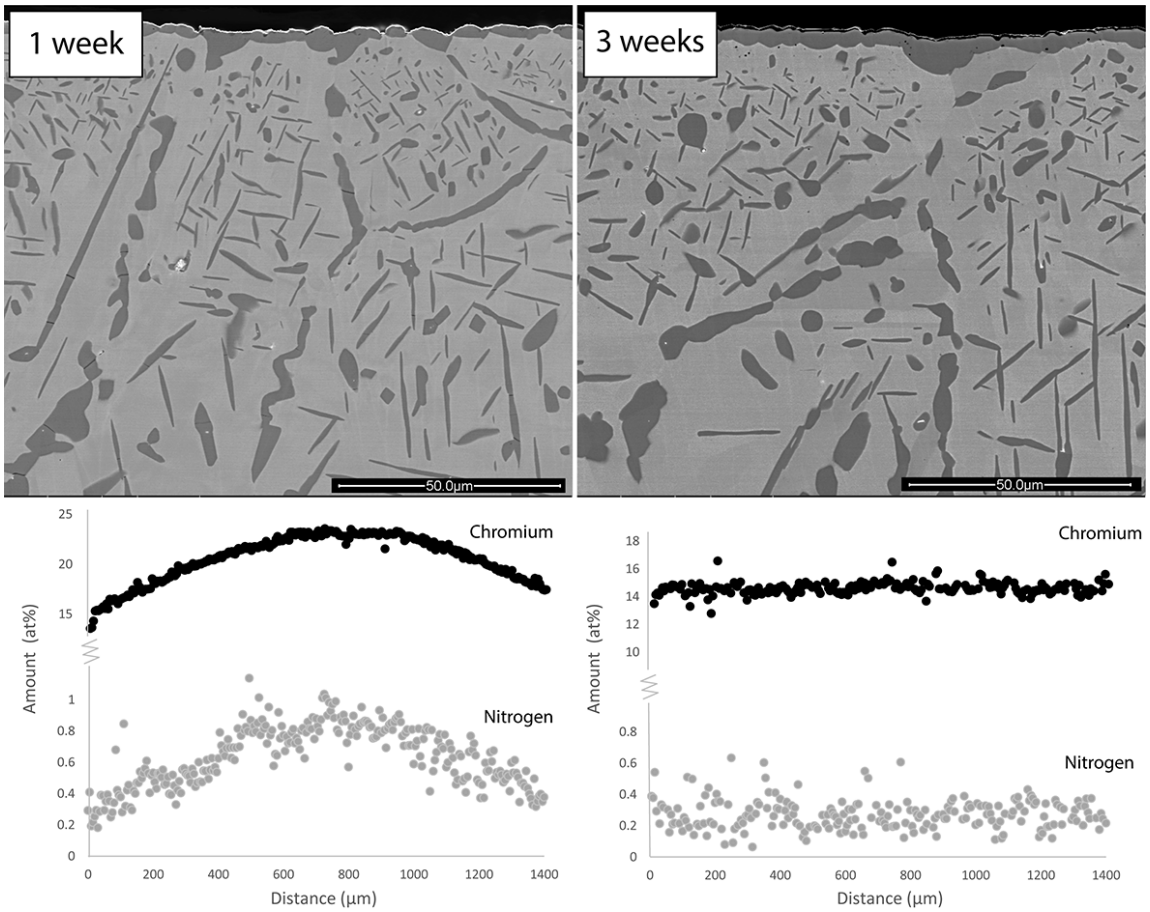

Figure 45 Top: SEM-BSE images of 353 MA after 1 week and 3 weeks of exposure at 1100 °C in a nitriding environment. Bottom: EPMA line-scans in the matrix showing the chromium and nitrogen concentrations through the alloy coupons.

Figure 46 shows the microstructures of 253 MA samples exposed for 1 week and 3 weeks, together with the EPMA line-scans through the sample. For 253 MA, it can be stated, in accordance with the mass gain results, that equilibrium is reached already after 1 week. The equilibrium concentration of chromium in the solid solution is 17.2 at.% (16.3 wt.%) and that of nitrogen is 1.4 at.% (0.36 wt.%).

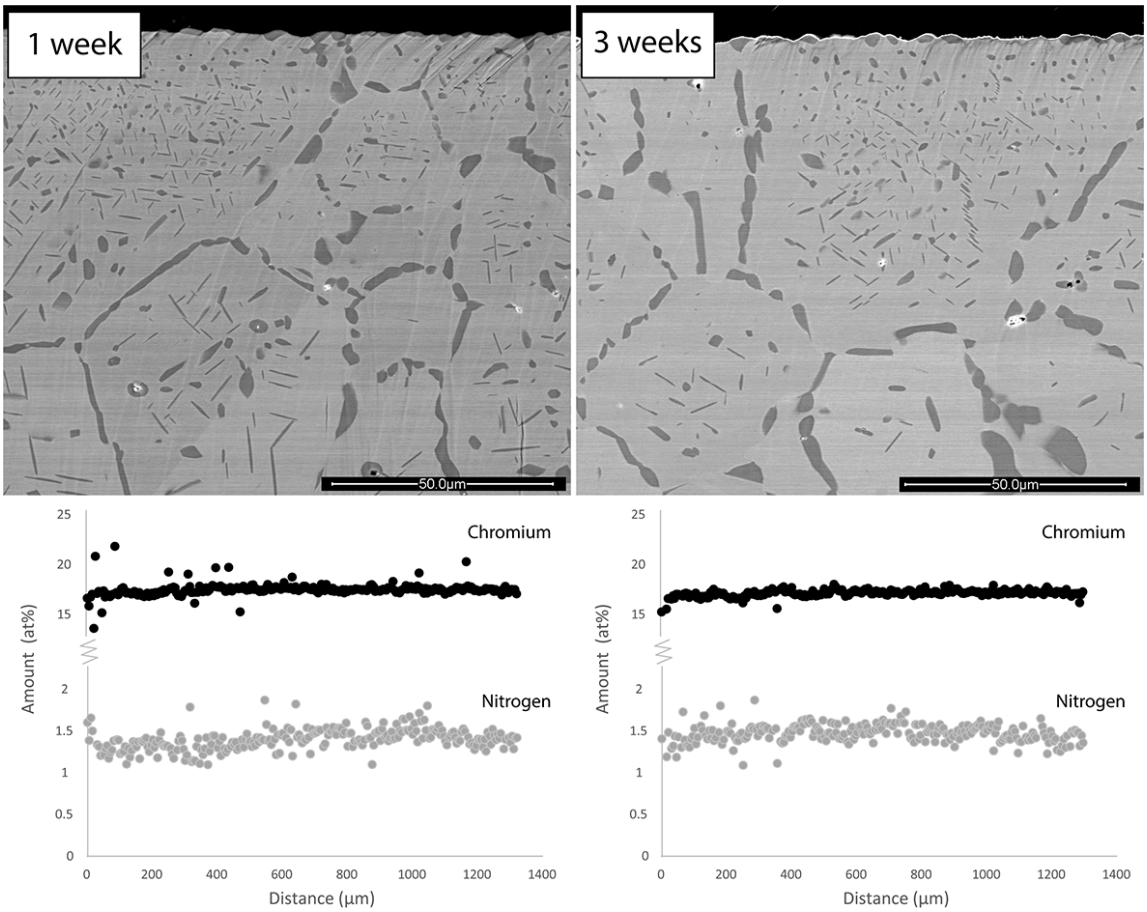

Figure 46 Top: SEM-BSE images of 253 MA after 1 week and 3 weeks of exposure at 1100 °C in a nitriding environment. Bottom: EPMA line-scans in the matrix showing the chromium and nitrogen concentrations through the alloy coupons.

Figure 47 shows cross-sectional images of Alloy 600 together with the EPMA line-scans of chromium and nitrogen through the sample after exposure after 1 and 3 weeks of nitridation. The shapes of the EPMA curves reveal that equilibrium is achieved for Alloy 600 already after 1 week of exposure. The amount of chromium in the solid solution after 3 weeks is about 18.4 at.%, corresponding to 16.5 wt.%, while the concentration of nitrogen is about 0.19 at.%, corresponding to 0.047 wt.%. This means that the chromium concentration in the alloy after exposure is almost the same as before exposure (16.7 wt.%). Furthermore, a continuous Al-rich surface scale is observed after 3 weeks. This is noteworthy, given that the aluminium concentration in the alloy is only 0.14 wt.%. The formation of the oxide scale is not considered to influence the nitridation of the alloy coupon since the nitridation reaction appears to have reached equilibrium already after 1 week of exposure, before a continuous alumina scale had formed on the surface.

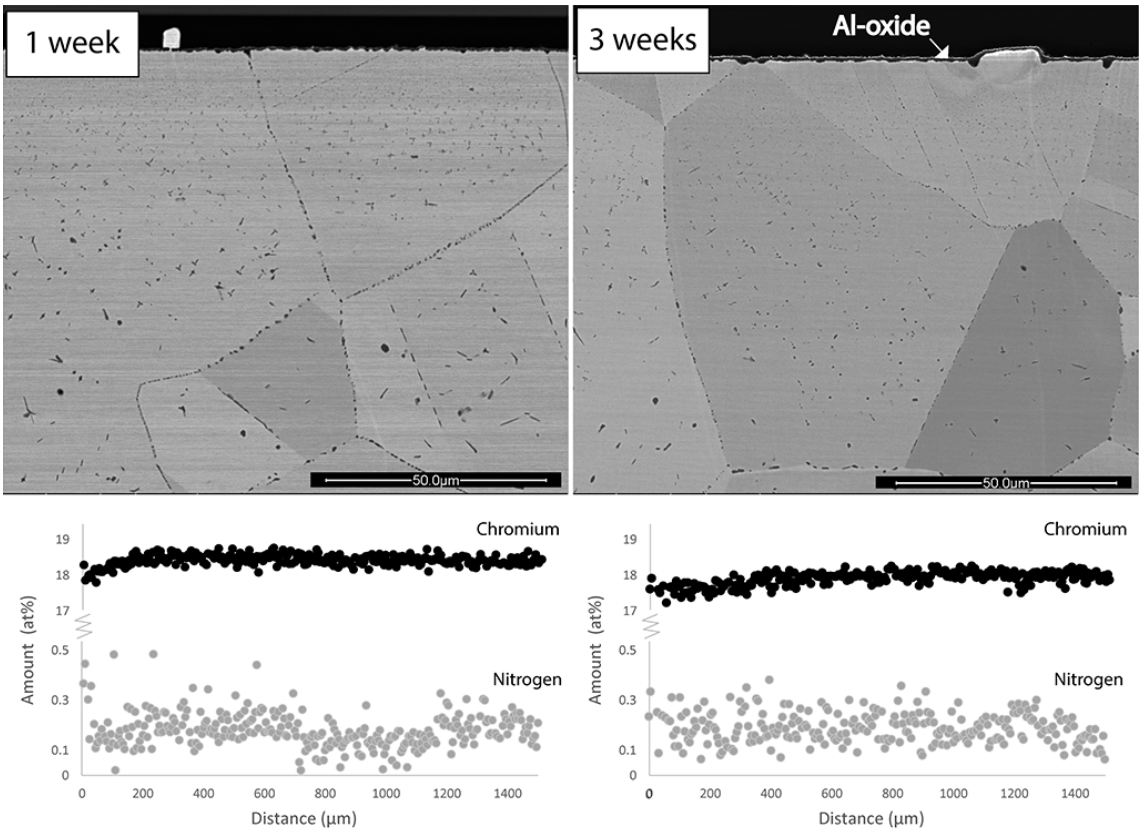

Figure 47 Top: SEM-BSE images of Alloy 600 after 1 week and 3 weeks of exposure at 1100 °C in a nitriding environment. Bottom: EPMA line-scans in the matrix showing the chromium and nitrogen concentrations through the alloy coupons.

Upon closer examination of the precipitates formed in 253 MA and Alloy 600, it becomes evident that the nitrides formed are different phases, see Figure 48. In 253 MA, the hexagonal $Cr_{2-x}Fe_xN$ is present, while in Alloy 600 the cubic $Ti_{1-x}Cr_xN$ is present. Thus, the results show that the composition of Alloy 600 is apparently beneficial under the experimental conditions, minimizing nitride precipitation. Since the experimental evidence indicates that the nitridation reaction is close to equilibrium at the end of the exposure, the different extent of nitride precipitation in the three alloys must be due to differences in chromium activity. Thus, the non-appearance of Cr_2N in Alloy 600 indicates a relatively low chromium activity in that alloy. This is in line with Mazandarany et al. [159] who report that for NiCr systems, the chromium activity exhibits a negative deviation from ideality. The same authors report that additions of nickel to FeCr alloys (9-30 wt.% Cr) result in an increased chromium activity. The latter result is in line with the observation that the concentration of chromium in the alloy matrix at the end of the exposure (at equilibrium) is lower for 353 MA than for 253 MA.

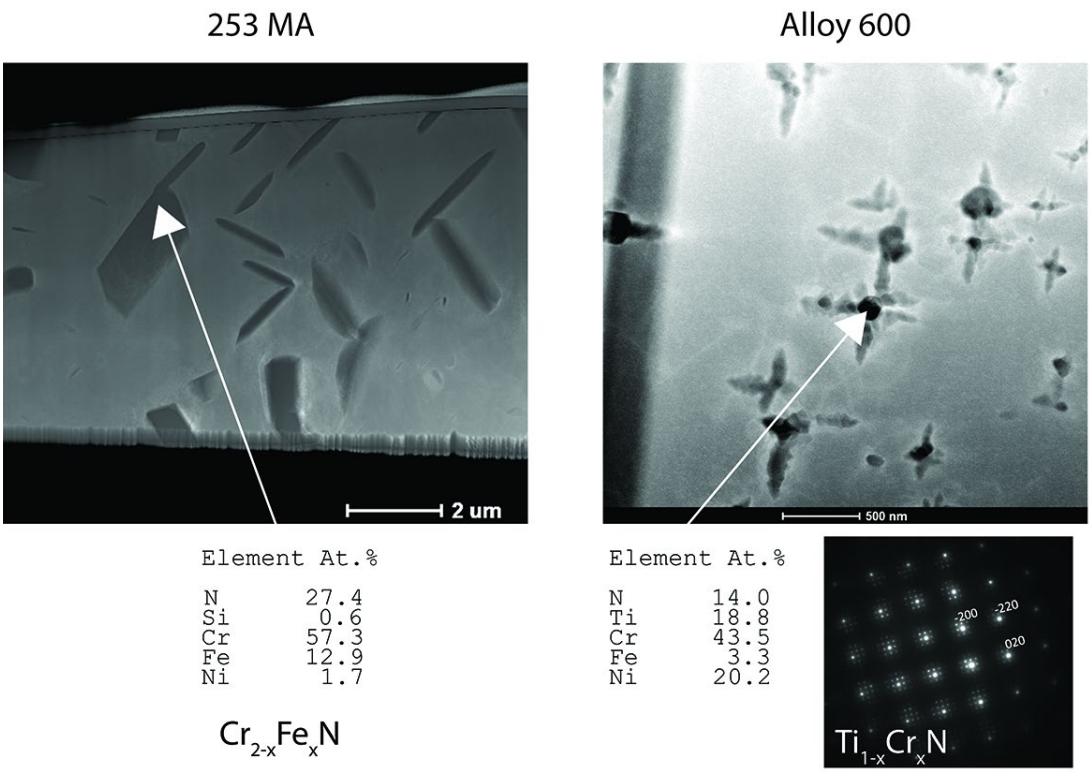

Figure 48 STEM HAADF images of 253 MA and Alloy 600 showing nitride precipitates after exposure for 1 week at 1100 °C. The EDS analysis shows that the nitrides in 253 MA are $Cr_{2-x}Fe_xN$. The CBED patterns together with the EDS analysis show that the precipitates in Alloy 600 are $Ti_{1-x}Cr_xN$.

10 SUMMARY

10.1 HIGH OXYGEN ACTIVITY

Chromia-forming alloys

The results showed the influence of the nickel and chromium concentrations in the alloys and how the supply of chromium to the oxide scale influences the evolution of the oxide scale at 800 °C. Alloy 600 has a high concentration of nickel and a relatively low concentration of chromium; it forms an externa scale consisting of mainly NiO and forms chromia only at the alloy grain boundaries where the diffusion rate of chromium is higher. Due to the formation of NiO, the rate of chromium evaporation was relatively low. The rapid growth of NiO leads to high oxidation rates and hinders the formation of a chromia scale. Over time, a layer of chromia is formed at the oxide/metal interface.

For Alloy 690, the evolution of the oxide scale was studied as a function of gas flow velocity, at 800 °C. At low flow velocity, a chromia scale was present during the 200 hour long exposure and the alloy substrate was able to supply chromium to the chromia scale without a change in the mechanism of oxidation. However, when the rate of $CrO_2(OH)_2$ evaporation increased due to increased gas flow velocity, the resulting chromium depletion of the alloy substrate caused nickel oxidation to start. Subsequently, the formation of an external NiO layer caused the evaporation rate to decrease rapidly. Eventually, a secondary, protective chromia layer was formed at the oxide/metal interface.

Alumina-forming alloys

The ferritic FeCrAl alloys studied had different concentrations of aluminium, chromium and silicon. All the alloys formed slow-growing, protective, Al-rich oxide scales in the environments investigated. Chromium volatilisation was very low in all cases. Interestingly, the Si-containing FeCrAl alloy formed an oxide scale that contained a lot of silicon in the outer part. Over time, this scale appeared to separate into the following regions: 1) an outer region with almost pure SiO_2 (identified as tridymite by XRD); 2) a middle oxide layer that was rich in both silicon and aluminium (identified as mullite by XRD); and 3) an inner layer of alumina. This layered structure was only observed in an environment that contained both oxygen and water. The presence of silicon in the outer part of the oxide scale resulted in an even lower chromium volatilisation compared to a scale consisting of only alumina. After oxidation in dry air, silicon was not detected in the oxide scale. Silicon was not detected in the scale of a FeCrAl with no added silicon after oxidation in oxygen and water, showing that the silicon in the scale does not originate from the fused quartz reaction tube. The ability of the relatively chromium- and aluminium-lean EF101 to form a protective Al-rich oxide scale also at 600 °C is attributed to the silicon added.

10.2 LOW OXYGEN ACTIVITY

Chromia-forming alloys

Exposures in 95% N_2 and 5% H_2 at 900 °C were performed in such a way that the traces of water vapour present were either above or below the threshold for chromia to form on the alloy surface. This enabled an investigation of how effective a chromia scale is in preventing nitridation. In one of the environments, designated H, the oxygen activity was just sufficient for a chromia scale to form, while in the other environment, designated L, the oxygen activity was insufficient for a chromia scale to form. Side-by-side comparisons using both gravimetry and GD-OES showed that the formation of a chromia scale reduced the amount of nitridation by 50-95%. The presence of a duplex oxide scale that contained both chromia and silica was especially effective in protecting against nitrogen ingress.

In order to learn more about how nitrogen penetrates a chromia scale, an attempt was made to identify nitrogen in the oxide scale using APT. The study detected >200 at. ppm of nitrogen in the $MnCr_2O_4$ spinel grains in the scale. However, no evidence of nitrogen was found in the chromia grains or in the chromia grain boundaries.

Time-resolved exposures were carried out on three chromia-forming alloys at 1100 °C in a nitriding environment, where the oxygen activity was insufficient for chromia to form. After 3 weeks of exposure, alloy nitridation had reached equilibrium. The results showed that 353 MA, having the highest chromium concentration, formed the highest amount of chromium nitrides, whereas Alloy 600, having the lowest chromium concentration, formed the lowest level of nitride precipitates. The different extent of nitridation of the three alloys is attributed to the differences in chromium activity. The beneficial nitridation behaviour of Alloy 600 is thus connected to its relatively low chromium activity.

At both 900 °C and 1100 °C it was found that the nitridation rate decreased with increasing nickel concentration. For the exposures at 1100 °C this can be observed by examining the degree of nitridation after the first 24 hours, at which point the nitridation is far from equilibrium. After 24 hours, the alloy with highest mass gain due to nitridation is 253 MA, which contains the lowest concentration of nickel.

Alumina-forming alloys

The results show that defect-free alumina scales are impermeable to nitrogen under the experimental conditions. This is evident from the GD-OES measurements of EF101 exposed in a nitriding environment at 900 °C. It was evident that no or very limited nitrogen was able to enter the alloy before an alumina scale was formed. Nitridation of an alumina-forming alloy instead depends on defects in the alumina scale. In this work, macro defects at large RE-

particles are shown to be points-of-entry for nitrogen into the alloy. In the case of APMT with much larger RE-particles than EF100 and EF101, severe nitridation was observed.

11 FUTURE WORK

This chapter describes the most relevant topics that could be explored in future work, which were no investigated in this thesis due to time or resource limitations.

11.1 HIGH OXYGEN ACTIVITY

- For Alloy 690, it would be interesting to study how the formation of NiO is triggered by factors such as alloy grain size, longer exposures times, temperatures, and varying chromium concentration. It would also be interesting to study the protectiveness of a scale that consists of a NiO 'cap layer' as the outer part and a highly protective chromia as the inner part.
- For EF101 alloyed with silicon, it would be interesting to study how silicon is incorporated into the oxide scale. This could be accomplished using more advanced microscopy, e.g., more TEM examinations, APT examinations of the scale to determine how silicon and aluminium are located in the scale, and computational simulations.

11.2 LOW OXYGEN ACTIVITY

- The mechanism by which nitrogen penetrates the chromia scale warrants further examination. In the current APT examination, there was overlapping between the Ti-containing species and N-containing species, which made the identification and quantification of nitrogen difficult. By studying an alloy system without titanium or by exposing the alloy in an environment with only O-18 and/or N-15, the quantification of nitrogen could be made easier.
- It would also be interesting to perform time-resolved studies in the two environments (H and L) to see if the nitridation rate decreases with oxide thickness.
- The alumina-forming alloys that formed an alumina scale without any macro-defects were shown to stop nitridation completely. However, the exposures were performed in an iso-thermal manner and for short times. Therefore, it would be interesting to examine how these alloys perform under more-realistic application conditions. For instance, thermal cycling together with longer exposure time. This could potentially trigger break-down of the alumina scale, and it would then be interesting to see if the alloy is able to heal the alumina scale without picking up nitrogen.

REFERENCES

1. *IPCC, 2021: Climate Change 2021: The Physical Science Basis. Contribution of Working Group I to the Sixth Assessment Report of the Intergovernmental Panel on Climate Change [Masson-Delmotte, V., P. Zhai, A. Pirani, S.L. Connors, C. Péan, S. Berger, N. Caud, Y. Chen, L. Goldfarb, M.I. Gomis, M. Huang, K. Leitzell, E. Lonnoy, J.B.R. Matthews, T.K. Maycock, T. Waterfield, O. Yelekçi, R. Yu, and B. Zhou (eds.)]. Cambridge University Press. In Press*.
2. *Carbon cycle greenhouse gases*. 2022-01-04]; Available from: https://gml.noaa.gov/ccgg/index.html.
3. *Emissions by sector*. 2022-01-04]; Available from: https://ourworldindata.org/emissions-by-sector.
4. Snavely, C.A. and C.L. Faust, *STUDIES ON THE STRUCTURE OF HARD CHROMIUM PLATE.* Journal of the Electrochemical Society, 1950. **97**(3): p. 99-108.
5. Zheng, X.G. and D.J. Young, *HIGH-TEMPERATURE CORROSION OF CR2O3-FORMING ALLOYS IN CO-CO2-N-2 ATMOSPHERES.* Oxidation of Metals, 1994. **42**(3-4): p. 163-190.
6. Young, D.J., et al., *Penetration of protective chromia scales by carbon.* Scripta Materialia, 2014. **77**: p. 29-32.
7. Asteman, H., et al., *Indication of Chromium Oxide Hydroxide Evaporation During Oxidation of 304L at 873 K in the Presence of 10% Water Vapor.* Oxidation of Metals, 1999. **52**(1): p. 95-111.
8. Asteman, H., J.E. Svensson, and L.G. Johansson, *Effect of water-vapor-induced Cr vaporization on the oxidation of austenitic stainless steels at 700 and 900 degrees C - Influence of Cr/Fe ratio in alloy and Ce additions.* Journal of the Electrochemical Society, 2004. **151**(3): p. B141-B150.
9. Ebbinghaus, B.B., *Thermodynamics of gas phase chromium species: The chromium oxides, the chromium oxyhydroxides, and volatility calculations in waste incineration processes.* Combustion and Flame, 1993. **93**(1): p. 119-137.
10. Opila, E.J., et al., *Theoretical and Experimental Investigation of the Thermochemistry of CrO2(OH)2(g).* The Journal of Physical Chemistry A, 2007. **111**(10): p. 1971-1980.
11. Schütze, M., D. Renusch, and M. Schorr, *Chemical-mechanical failure of oxide scales on 9% Cr steels in air with H2O.* Materials at high temperatures, 2005. **22**(1-2): p. 113-120.
12. Evans, H., A. Donaldson, and T. Gilmour, *Mechanisms of breakaway oxidation and application to a chromia-forming steel.* Oxidation of Metals, 1999. **52**(5): p. 379-402.
13. Chen, X., *Chromium deposition and poisoning of cathodes of solid oxide fuel cells–a review.* International Journal of Hydrogen Energy, 2014. **39**(1): p. 505-531.
14. Geers, C., et al., *Properties of Alumina/Chromia Scales in N-2-Containing Low Oxygen Activity Environment Investigated by Experiment and Theory.* Oxidation of Metals, 2017. **87**(3-4): p. 321-332.
15. Lai, G.Y., *High temperature corrosion of engineering alloys.* 1990.
16. Martinz, H.P., et al., *Carburization of high temperature PM-materials.* Materials and Corrosion-Werkstoffe Und Korrosion, 1998. **49**(4): p. 246-251.
17. Eklund, J., et al., *The influence of silicon on the corrosion properties of FeCrAl model alloys in oxidizing environments at 600 degrees C.* Corrosion Science, 2018. **144**: p. 266-276.

18. Birks, N., G.H. Meier, and F.S. Pettit, *Introduction to the high temperature oxidation of metals*. 2006: Cambridge University Press.
19. Van Wylen, G., R. Sonntag, and C. Borgnakke, *Fundamentals of Classical Thermodynamics, John Willey & Sons.* Inc, 1994.
20. Bordenet, B., *Influence of novel cycle concepts on the high-temperature corrosion of power plants.* Materials and Corrosion-Werkstoffe Und Korrosion, 2008. **59**(5): p. 361-366.
21. Salmenoja, K., M. Hupa, and R. Backman, *Laboratory studies on the influence of gaseous HCl on superheater corrosion*. Impact of Mineral Impurities in Solid Fuel Combustion, ed. R.P. Gupta, T.F. Wall, and L. Baxter. 1999. 513-523.
22. Stanger, R., et al., *Oxyfuel combustion for CO2 capture in power plants.* International Journal of Greenhouse Gas Control, 2015. **40**: p. 55-125.
23. Pettersson, J., et al., *A pilot plant study of the effect of alkali salts on initial stages of the high temperature corrosion of alloy 304L*, in *High Temperature Corrosion and Protection of Materials 6, Prt 1 and 2, Proceedings*, P. Steinmetz, et al., Editors. 2004. p. 965-972.
24. Pettersson, J., et al., *The effects of KCl, K2SO4 and K2CO3 on the high temperature corrosion of a 304-type austenitic stainless steel.* Oxidation of metals, 2011. **76**(1): p. 93-109.
25. Liu, K., C. Song, and V. Subramani, *Hydrogen and syngas production and purification technologies*. 2009: John Wiley & Sons.
26. Wang, Y., et al., *A review of polymer electrolyte membrane fuel cells: Technology, applications, and needs on fundamental research.* Applied Energy, 2011. **88**(4): p. 981-1007.
27. Stambouli, A.B. and E. Traversa, *Solid oxide fuel cells (SOFCs): a review of an environmentally clean and efficient source of energy.* Renewable & Sustainable Energy Reviews, 2002. **6**(5): p. 433-455.
28. Falk-Windisch, H., J.E. Svensson, and J. Froitzheim, *The effect of temperature on chromium vaporization and oxide scale growth on interconnect steels for Solid Oxide Fuel Cells.* Journal of Power Sources, 2015. **287**: p. 25-35.
29. Jiang, S.P. and X. Chen, *Chromium deposition and poisoning of cathodes of solid oxide fuel cells – A review.* International Journal of Hydrogen Energy, 2014. **39**(1): p. 505-531.
30. Aphale, A.N., et al., *Oxidation Behavior and Chromium Evaporation From Fe and Ni Base Alloys Under SOFC Systems Operation Conditions.* Jom, 2019. **71**(1): p. 116-123.
31. Ochoa, G.V., Y.E. Cardenas, and A.A. Arrieta, *Mapping the research on gasification to syngas production using scientometry analysis from 2007 to 2017.* Chemical Engineering Transactions, 2018. **65**: p. 181-186.
32. Bakker, W., *High temperature corrosion in gasifiers.* Materials Research, 2004. **7**: p. 53-59.
33. Jeon, J. and S.J. Kim, *Recent progress in hydrogen flammability prediction for the safe energy systems.* Energies, 2020. **13**(23): p. 6263.
34. Ellison, T.L., R.H. Shay, and K.R. Berger, *Selecting atmosphere compositions for bright annealing stainless.* Metal progress, 1983. **123**(7): p. 37-44.
35. States, S.S.I.o.t.U., et al., *Design Guidelines for the Selection and Use of Stainless Steel*. 1993: Specialty Steel Industry of the United States.
36. Rebak, R., *Crystallinne alloys: nickel*. 2013. 197-218.

37. Kim, I.S., et al., *Effect of microstructural characteristics on the low cycle fatigue behaviors of cast Ni-base superalloys.* Materials Characterization, 2015. **106**: p. 375-381.
38. Pike, L. *Development of a fabricable gamma-prime (γ') strengthened superalloy*. in *Proceedings of The 11th International Symposium on Superalloys*. 2008.
39. Pint, B.A., J. Leibowitz, and J.H. DeVan, *The effect of an oxide dispersion on the critical Al content in Fe-Al alloys.* Oxidation of Metals, 1999. **51**(1-2): p. 181-197.
40. Stott, F.H., G.C. Wood, and J. Stringer, *THE INFLUENCE OF ALLOYING ELEMENTS ON THE DEVELOPMENT AND MAINTENANCE OF PROTECTIVE SCALES.* Oxidation of Metals, 1995. **44**(1-2): p. 113-145.
41. Grobner, P.J., *The 885° f (475° c) embrittlement of ferritic stainless steels.* Metallurgical Transactions, 1973. **4**(1): p. 251-260.
42. Spear, W.S. and D.H. Polonis, *INTERSTITIAL PRECIPITATION IN FE-CR-AL ALLOYS.* Metallurgical and Materials Transactions a-Physical Metallurgy and Materials Science, 1994. **25**(6): p. 1135-1146.
43. Ejenstam, J., et al., *Microstructural stability of Fe-Cr-Al alloys at 450-550 degrees C.* Journal of Nuclear Materials, 2015. **457**: p. 291-297.
44. Lim, J., I.S. Hwang, and J.H. Kim, *Design of alumina forming FeCrAl steels for lead or lead–bismuth cooled fast reactors.* Journal of Nuclear Materials, 2013. **441**(1): p. 650-660.
45. Guan, S.W., J. Corkum, and W. Smeltzer, *OXIDATION BEHAVIOR OF FE-AL-SI ALLOYS AT 1073-K AND 1173-K*. High Temperature Corrosion of Advanced Materials and Protective Coatings, ed. Y. Saito, B. Onay, and T. Maruyama. 1992. 75-82.
46. Asokan, V., et al., *The influence of Si on the primary protection of lean FeCrAl model alloys in O-2 and O-2+ H2O at 600 degrees C-A microstructural investigation.* Corrosion Science, 2021. **179**.
47. Tomaszewicz, P. and G.R. Wallwork, *OBSERVATIONS OF NODULE GROWTH DURING THE OXIDATION OF PURE BINARY IRON ALUMINUM-ALLOYS.* Oxidation of Metals, 1983. **19**(5-6): p. 165-185.
48. Tomaszewicz, P. and G.R. Wallwork, *THE OXIDATION OF HIGH-PURITY IRON-CHROMIUM-ALUMINUM ALLOYS AT 800-DEGREES-C.* Oxidation of Metals, 1983. **20**(3-4): p. 75-109.
49. Boggs, W.E., *OXIDATION OF IRON-ALUMINUM ALLOYS FROM 450 DEGREES TO 900 DEGREES C.* Journal of the Electrochemical Society, 1971. **118**(6): p. 906-&.
50. Zhang, Z.G., et al., *Criteria for the formation of protective Al2O3 scales on Fe-Al and Fe-Cr-Al alloys.* Corrosion Science, 2006. **48**(3): p. 741-765.
51. Whittle, D.P. and J. Stringer, *IMPROVEMENTS IN HIGH-TEMPERATURE OXIDATION RESISTANCE BY ADDITIONS OF REACTIVE ELEMENTS OR OXIDE DISPERSIONS.* Philosophical Transactions of the Royal Society a-Mathematical Physical and Engineering Sciences, 1980. **295**(1413): p. 309-+.
52. Pint, B., *On the formation of interfacial and internal voids in α-Al 2 O 3 scales.* Oxidation of Metals, 1997. **48**(3): p. 303-328.
53. Naumenko, D., B.A. Pint, and W. Quadakkers, *Current thoughts on reactive element effects in alumina-forming systems: in memory of John Stringer.* Oxidation of Metals, 2016. **86**(1): p. 1-43.
54. Rahmel, A. and M. Schutze, *MECHANICAL ASPECTS OF THE RARE-EARTH EFFECT.* Oxidation of Metals, 1992. **38**(3-4): p. 255-266.

55. Tolpygo, V.K. and H.J. Grabke, *The effect of impurities on the alumina scale growth: An alternative view.* Scripta Materialia, 1997. **38**(1): p. 123-129.
56. Sigler, D.R., *Adherence behavior of oxide grown in air and synthetic exhaust gas on Fe-Cr-Al alloys containing strong sulfide-forming elements: Ca, Mg, Y, Ce, La, Ti, and Zr.* Oxidation of metals, 1993. **40**(5): p. 555-583.
57. Mortazavi, N., et al., *Interplay of water and reactive elements in oxidation of alumina-forming alloys.* Nature Materials, 2018. **17**(7): p. 610-+.
58. Kofstad, P., *High temperature corrosion.* Elsevier Applied Science Publishers, Crown House, Linton Road, Barking, Essex IG 11 8 JU, UK, 1988., 1988.
59. Young, D.J., *High temperature oxidation and corrosion of metals*. Vol. 1. 2008: Elsevier.
60. *The Ellingham diagram*. [Cited 2019-09-05]; Available from: https://doitpoms.ac.uk/tlplib/ellingham_diagrams/ellingham.php.
61. Wagner, C., *Beitrag zur theorie des anlaufvorgangs.* Zeitschrift für physikalische Chemie, 1933. **21**(1): p. 25-41.
62. Pujilaksono, B., et al., *Oxidation of Binary FeCr Alloys (Fe-2.25Cr, Fe-10Cr, Fe-18Cr and Fe-25Cr) in O-2 and in O-2 + H2O Environment at 600 degrees C.* Oxidation of Metals, 2011. **75**(3-4): p. 183-207.
63. Asteman, H., et al., *Influence of Water Vapor and Flow Rate on the High-Temperature Oxidation of 304L; Effect of Chromium Oxide Hydroxide Evaporation.* Oxidation of Metals, 2000. **54**(1): p. 11-26.
64. Huczkowski, P., et al., *Effect of gas flow rate on oxidation behaviour of alloy 625 in wet air in the temperature range 900–1000 °C.* Materials and Corrosion, 2017. **68**(2): p. 159-170.
65. Kofstad, P., *Defects and transport properties of metal oxides.* Oxidation of Metals, 1995. **44**(1): p. 3-27.
66. Deal, B.E. and A. Grove, *General relationship for the thermal oxidation of silicon.* Journal of applied physics, 1965. **36**(12): p. 3770-3778.
67. Jones, D.A., *Principles and Prevention of Corrosion, 2nd.* Ed. Upper Saddle River, NY: Prentice Hall, 1996: p. 168-198.
68. Sutton, A.P., *Interfaces in crystalline materials.* Monographs on the Physice and Chemistry of Materials, 1995: p. 414-423.
69. Gleeson, B., *Corrosion and Environmental Degradation of Materials, V. II.* Materials Science and Technology, 2000. **19**: p. 174-228.
70. Paidassi, J., *Contribution à l'étude de l'oxydation du fer dans l'air dans l'intervalle 700-1250° C.* Revue de métallurgie, 1957. **54**(8): p. 569-585.
71. Larsson, H., et al., *Oxidation of iron at 600 C–experiments and simulations.* Materials and corrosion, 2017. **68**(2): p. 133-142.
72. Kofstad, P., *Nonstoichiometry, diffusion, and electrical conductivity in binary metal oxides.* 1972.
73. Nagai, H., S. Ishikawa, and K.-i. Shoji, *Electrical conductivity of sintered Cr2O3 with Fe2O3.* Transactions of the Japan Institute of Metals, 1985. **26**(1): p. 44-51.
74. Kofstad, P. and K. Lillerud, *On high temperature oxidation of chromium II. Properties of and the oxidation mechanism of chromium.* Journal of the electrochemical society, 1980. **127**(11): p. 2410-2419.
75. Lillerud, K. and P. Kofstad, *On high temperature oxidation of chromium I. Oxidation of annealed, thermally etched chromium at 800–1100 C.* Journal of the electrochemical society, 1980. **127**(11): p. 2397-2410.

76. Young, E.W.A., J.H. Gerretsen, and J.H.W. de Wit, *The Oxygen Partial Pressure Dependence of the Defect Structure of Chromium(III)Oxide.* Journal of The Electrochemical Society, 1987. **134**(9): p. 2257-2260.
77. Gleeson, B., *1.09 - Thermodynamics and Theory of External and Internal Oxidation of Alloys*, in *Shreir's Corrosion*, B. Cottis, et al., Editors. 2010, Elsevier: Oxford. p. 180-194.
78. Chen, G.F. and H.Y. Lou, *Predicting the oxide formation of Ni-Cr-Al alloys with nano-sized grain.* Materials Letters, 2000. **45**(5): p. 286-291.
79. Wood, G., et al., *The identification of thin healing layers at the base of oxide scales on FeCr base alloys.* Corrosion science, 1969. **9**(9): p. 659-671.
80. Jonsson, T., et al., *Influence of H2O(g) on the oxide microstructure of the stainless steel 353MA at 900 degrees C in oxygen.* Journal of the Electrochemical Society, 2007. **154**(11): p. C603-C610.
81. Bennett, M., J. Desport, and P. Labun, *Transverse microstructure of an oxide scale formed on a 20% Cr–25% Ni–niobium stabilized stainless steel.* Proceedings of the Royal Society of London. A. Mathematical and Physical Sciences, 1987. **412**(1842): p. 223-230.
82. Issartel, C., H. Buscail, and S. Mathieu, *Influence of atmosphere on high-temperature oxidation of Fe-Cr-Si model alloy.* Materials and Corrosion-Werkstoffe Und Korrosion, 2019. **70**(8): p. 1410-1415.
83. Stott, F., G. Wood, and J. Stringer, *The influence of alloying elements on the development and maintenance of protective scales.* Oxidation of metals, 1995. **44**(1): p. 113-145.
84. Bennett, M.J., J.A. Desport, and P.A. Labun, *Analytical electron microscopy of a selective oxide scale formed on 20% Cr-25% Ni-Nb stainless steel.* Oxidation of Metals, 1984. **22**(5): p. 291-306.
85. Adachi, T. and G. Meier, *Oxidation of iron-silicon alloys.* Oxidation of metals, 1987. **27**(5): p. 347-366.
86. Oishi, Y. and W. Kingery, *Self‐diffusion of oxygen in single crystal and polycrystalline aluminum oxide.* The Journal of Chemical Physics, 1960. **33**(2): p. 480-486.
87. Heuer, A., *Oxygen and aluminum diffusion in α-Al2O3: how much do we really understand?* Journal of the European Ceramic Society, 2008. **28**(7): p. 1495-1507.
88. Sadique, S.E., et al., *High-Temperature Oxidation Behavior of Iron–Chromium–Aluminum Alloys.* Oxidation of Metals, 2000. **54**(5): p. 385-400.
89. Liu, F., et al., *TEM investigation of the oxide scales formed on a FeCrAlRE alloy (Kanthal AF) at 900 degrees C in dry O-2 and O-2 with 40% H2O.* Materials at High Temperatures, 2005. **22**(3-4): p. 521-526.
90. Asteman, H., *Water Vapour induced active oxidation of stainless steel.* 2002.
91. Asteman, H., J.-E. Svensson, and L.-G. Johansson, *Oxidation of 310 steel in H2O/O2 mixtures at 600 C: the effect of water-vapour-enhanced chromium evaporation.* Corrosion Science, 2002. **44**(11): p. 2635-2649.
92. Asteman, H., J.E. Svensson, and L.G. Johansson, *The high temperature oxidation of marginal chromia formers in an oxygen/water vapor mixture; The influence of flow rate*. High Temperature Corrosion and Materials Chemistry, ed. M. McNallan, et al. Vol. 99. 2000, Pennington: Electrochemical Society Inc. 127-134.
93. Bailey, J., *Volatile Cr contamination reduction in atmospheric pressure chemical vapor deposition systems by selective alloy oxidation.* Journal of the Electrochemical Society, 1997. **144**(10): p. 3568-3571.

94. Bhowmick, S., et al., *ASSESSMENT OF CHROMIUM EVAPORATION FROM CHROMIA AND ALUMINA FORMING ALLOYS*, in *Advances in Solid Oxide Fuel Cells Vii*, N.P. Bansal, et al., Editors. 2011. p. 115-124.
95. Deodeshmukh, V.P., *Long-Term Performance of High-Temperature Foil Alloys in Water Vapor Containing Environment. Part I: Oxidation Behavior.* Oxidation of Metals, 2013. **79**(5): p. 567-578.
96. Ehlers, J., et al., *Enhanced oxidation of the 9%Cr steel P91 in water vapour containing environments.* Corrosion Science, 2006. **48**(11): p. 3428-3454.
97. Essuman, E., et al., *Enhanced internal oxidation as trigger for breakaway oxidation of Fe–Cr alloys in gases containing water vapor.* Scripta Materialia, 2007. **57**(9): p. 845-848.
98. Henry, S., et al., *Characterization of Chromia Scales Grown on Pure Chromium in Different Oxidizing Atmospheres.* Materials at High Temperatures, 2000. **17**(2): p. 231-234.
99. Hooshyar, H., et al., *The Effect of H-2 and H2O on the Oxidation of 304L-Stainless Steel at 600 A degrees C: General Behaviour (Part I).* Oxidation of Metals, 2016. **85**(3-4): p. 321-342.
100. Hultquist, G., B. Tveten, and E. Hörnlund, *Hydrogen in Chromium: Influence on the High-Temperature Oxidation Kinetics in H2O, Oxide-Growth Mechanisms, and Scale Adherence.* Oxidation of Metals, 2000. **54**(1): p. 1-10.
101. Jönsson, T., et al., *Microstructural investigation of the effect of water vapour on the oxidation of alloy 353 MA in oxygen at 700 and 900 degrees C.* Materials at High Temperatures, 2005. **22**(3-4): p. 231-243.
102. Meschter, P.J., E.J. Opila, and N.S. Jacobson, *Water Vapor-Mediated Volatilization of High-Temperature Materials*, in *Annual Review of Materials Research, Vol 43*, D.R. Clarke, Editor. 2013. p. 559-588.
103. Michalik, M., et al., *Effect of water vapour on growth and adherence of chromia scales formed on Cr in high and low PO2-environments at 1000 and 1050 degrees C.* Materials at High Temperatures, 2005. **22**(3-4): p. 213-221.
104. Pujilaksono, B., et al., *Paralinear oxidation of chromium in O(2)+H(2)O environment at 600-700 degrees C.* Oxidation of Metals, 2008. **70**(3-4): p. 163-188.
105. Stanislowski, M., et al., *Chromium vaporization from high-temperature alloys I. Chromia-forming steels and the influence of outer oxide layers.* Journal of the Electrochemical Society, 2007. **154**(4): p. A295-A306.
106. Stanislowski, M., et al., *Chromium vaporization from alumina-forming and aluminized alloys.* Solid State Ionics, 2008. **179**(40): p. 2406-2415.
107. Saunders, S., M. Monteiro, and F. Rizzo, *The oxidation behaviour of metals and alloys at high temperatures in atmospheres containing water vapour: A review.* Progress in materials science, 2008. **53**(5): p. 775-837.
108. Panas, I., et al., *Chromic acid evaporation upon exposure of Cr2O3(S) to H2O(g) and O-2(g) - mechanism from first principles.* Chemical Physics Letters, 2004. **383**(5-6): p. 549-554.
109. Froitzheim, J., et al., *Investigation of Chromium Volatilization from FeCr Interconnects by a Denuder Technique.* Journal of The Electrochemical Society, 2010. **157**(9): p. B1295-B1300.
110. Tedmon, C., *The effect of oxide volatilization on the oxidation kinetics of Cr and Fe‐Cr alloys.* Journal of the Electrochemical Society, 1966. **113**(8): p. 766-768.

111. Sachitanand, R., et al., *Evaluation of the oxidation and Cr evaporation properties of selected FeCr alloys used as SOFC interconnects.* International Journal of Hydrogen Energy, 2013. **38**(35): p. 15328-15334.
112. Froitzheim, J., et al., *Long term study of Cr evaporation and high temperature corrosion behaviour of Co coated ferritic steel for solid oxide fuel cell interconnects.* Journal of Power Sources, 2012. **220**: p. 217-227.
113. Trebbels, R., T. Markus, and L. Singheiser, *Investigation of Chromium Vaporization From Interconnector Steels With Spinel Coatings.* Journal of Fuel Cell Science and Technology, 2009. **7**(1): p. 011013-011013-6.
114. Stanislowski, M., et al., *Reduction of chromium vaporization from SOFC interconnectors by highly effective coatings.* Journal of Power Sources, 2007. **164**(2): p. 578-589.
115. Tomas, M., et al., *Cu-Based Coatings for IT-SOFC Applications.* ECS Transactions, 2019. **91**(1): p. 2291.
116. Grolig, J.G., et al., *Copper based conversion coatings on ferritic stainless strip steel as solid oxide fuel cell interconnects: oxidation performance and chromium evaporation.* ECS Transactions, 2013. **57**(1): p. 2339.
117. Wei, P., M.R. Bateni, and A. Petric, *Conversion of copper and manganese metallic films to spinel coating.* Journal of Materials Science, 2012. **47**(13): p. 5205-5215.
118. Essuman, E., et al., *The effect of water vapor on selective oxidation of Fe-Cr alloys.* Oxidation of Metals, 2008. **69**(3-4): p. 143-162.
119. Zurek, J., et al., *Growth and adherence of chromia based surface scales on Ni-base alloys in high- and low-pO(2) gases.* Materials Science and Engineering a-Structural Materials Properties Microstructure and Processing, 2008. **477**(1-2): p. 259-270.
120. Åkermark, T. and G. Hultquist, *Oxygen exchange in oxidation of an Fe-20Cr-10Al alloy in∼ 10 mbar O 2/H 2 O-gas mixtures at 920° C.* Oxidation of metals, 1997. **47**(1): p. 117-137.
121. Nakai, M., et al., *Correlation of high-temperature steam oxidation with hydrogen dissolution in pure iron and ternary high-chromium ferritic steel.* ISIJ international, 2005. **45**(7): p. 1066-1072.
122. Yang, Z., et al., *Oxidation behavior of ferritic stainless steels under SOFC interconnect exposure conditions.* Journal of the Electrochemical Society, 2004. **151**(12): p. B669.
123. Rufner, J., et al., *Oxidation behavior of stainless steel 430 and 441 at 800 C in single (air/air) and dual atmosphere (air/hydrogen) exposures.* International Journal of Hydrogen Energy, 2008. **33**(4): p. 1392-1398.
124. Alnegren, P., et al., *Severe dual atmosphere effect at 600 C for stainless steel 441.* Journal of Power Sources, 2016. **301**: p. 170-178.
125. Gunduz, K.O., et al., *The effect of hydrogen on the breakdown of the protective oxide scale in solid oxide fuel cell interconnects.* Corrosion Science, 2021. **179**: p. 109112.
126. Opila, E.J., et al., *Predicting oxide stability in high-temperature water vapor.* Jom, 2006. **58**(1): p. 22-28.
127. Götlind, H., et al., *The Effect of Water Vapor on the Initial Stages of Oxidation of the FeCrAl Alloy Kanthal AF at 900 °C.* Oxidation of Metals, 2007. **67**(5): p. 251-266.
128. Wriedt, H. and O. Gonzalez, *The solubility of nitrogen in solid iron-nickel alloys near 1000-degrees-C.* Transactions of the metallurgical society of AIME, 1961. **221**(3): p. 532-535.
129. Tjokro, K. and D.J. Young, *COMPARISON OF INTERNAL NITRIDATION REACTIONS IN AMMONIA AND IN NITROGEN.* Oxidation of Metals, 1995. **44**(3-4): p. 453-474.

130. Rosenqvist, T., *Principles of extractive metallurgy*. 2004: Tapir academic press.
131. Brady, M.P. and P. Sachenko, *Effects of Fe on the oxidation/internal nitridation behavior and tensile properties of Cr and oxide dispersion ductilized Cr.* Scripta Materialia, 2005. **52**(9): p. 809-814.
132. Udyavar, M. and D.J. Young, *Precipitate morphologies and growth kinetics in the internal carburisation and nitridation of Fe-Ni-Cr alloys.* Corrosion Science, 2000. **42**(5): p. 861-883.
133. Soleimani-Dorcheh, A. and M.C. Galetz, *Oxidation and Nitridation Behavior of Cr-Si Alloys in Air at 1473 K.* Oxidation of Metals, 2015. **84**(1-2): p. 73-90.
134. Kubaschewski, O., *Metallurgical thermochemistry.* International Series on Material Science and Technology, 1977. **24**: p. 478.
135. Taneichi, K., et al., *Oxidation or nitridation behavior of pure chromium and chromium alloys containing 10 mass% ni or Fe in atmospheric heating.* Materials Transactions, 2006. **47**(10): p. 2540-2546.
136. Douglass, D.L., *Anomalous behavior during internal oxidation and nitridation.* JOM, 1991. **43**(11): p. 74-79.
137. Jacobsen, C.J.H., et al., *Catalyst Design by Interpolation in the Periodic Table: Bimetallic Ammonia Synthesis Catalysts.* Journal of the American Chemical Society, 2001. **123**(34): p. 8404-8405.
138. Zheng, X.G. and D.J. Young, *High temperature reaction of chromium with multi-oxidant atmospheres*, in *High Temperature Corrosion and Protection of Materials 4, Pts 1 and 2*, R. Streiff, et al., Editors. 1997. p. 567-574.
139. Seybolt, A. and D. Haman, *OXIDATION-NITRIFICATION OF CHROMIUM AT 1000 DEGREES C.* Transactions of the Metallurgical Society of AIME, 1964. **230**(6): p. 1294-&.
140. Royer, L., et al., *On the Oxidation and Nitridation of Chromium at 1300 C.* Oxidation of metals, 2010. **74**(1): p. 79-92.
141. Michalik, M., et al., *Effects of water vapour on the high temperature nitridation of chromium.* Materials and Corrosion-Werkstoffe Und Korrosion, 2014. **65**(3): p. 260-266.
142. Jönsson, B. and C. Svedberg, *Limiting factors for Fe-Cr-Al and NiCr in controlled industrial atmospheres*, in *High Temperature Corrosion and Protection of Materials 4, Pts 1 and 2*, R. Streiff, et al., Editors. 1997. p. 551-557.
143. Barnes, J.J. and G.Y. Lai, *FACTORS AFFECTING THE NITRIDATION BEHAVIOR OF FE-BASE, NI-BASE, AND CO-BASE ALLOYS IN PURE NITROGEN.* Journal De Physique Iv, 1993. **3**(C9): p. 167-174.
144. Mortazavi, A.N., et al., *Exploring failure modes of alumina scales on FeCrAl and FeNiCrAl alloys in a nitriding environment.* Acta Materialia, 2020. **201**: p. 131-146.
145. Jahns, K., et al., *Formation of corrosion pockets in FeNiCrAl at high temperatures investigated by 3D FIB-SEM tomography.* Materials and Corrosion-Werkstoffe Und Korrosion, 2020. **71**(11): p. 1774-1782.
146. Jönsson, B. and C. Svedberg. *Limiting Factors for Fe-Cr-Al and NiCr in Controlled Industrial Atrmospheres*. in *Materials science forum*. 1997. Trans Tech Publ.
147. Veskovíc-Bukudur, S., et al., *HIgH teMperature corroSIon of coMMercIal fecral alloyS (KantHal af) In nItrogen gaS.* Journal of Mining and Metallurgy, Section B: Metallurgy, 2019. **55**(1): p. 55-55.

148. Barrer, R.M., *89. The mechanism of activated diffusion through silica glass.* Journal of the Chemical Society (Resumed), 1934: p. 378-386.
149. Johnson, J. and R. Burt, *The passage of hydrogen through quartz glass.* JOSA, 1922. **6**(7): p. 734-738.
150. Orloff, J., M. Utlaut, and L. Swanson, *Applications of focused ion beams*, in *High Resolution Focused Ion Beams: FIB and its Applications*. 2003, Springer. p. 205-290.
151. Goldstein, J.I., et al., *Scanning electron microscopy and X-ray microanalysis*. 2017: Springer.
152. Williams, D.B. and C.B. Carter, *The Transmission Electron Microscope*, in *Transmission Electron Microscopy: A Textbook for Materials Science*. 1996, Springer US: Boston, MA. p. 3-17.
153. Bluhm, H., *4 - X-ray photoelectron spectroscopy (XPS) for in situ characterization of thin film growth*, in *In Situ Characterization of Thin Film Growth*, G. Koster and G. Rijnders, Editors. 2011, Woodhead Publishing. p. 75-98.
154. Miller, M.K. and R.G. Forbes, *The local electrode atom probe*, in *Atom-Probe Tomography*. 2014, Springer. p. 229-258.
155. Fournier-Salaün, M.-C. and P. Salaün, *Quantitative determination of hexavalent chromium in aqueous solutions by UV-Vis spectrophotometer.* Central European Journal of Chemistry, 2007. **5**(4): p. 1084-1093.
156. Götlind, H., et al., *The effect of water vapor on the initial stages of oxidation of the FeCrAl alloy Kanthal AF at 900 degrees C.* Oxidation of Metals, 2007. **67**(5-6): p. 251-266.
157. Gesmundo, F. and F. Viani, *Transition from internal to external oxidation for binary alloys in the presence of an outer scale.* Oxidation of metals, 1986. **25**(5): p. 269-282.
158. Evans, H.E., et al., *Influence of silicon additions on the oxidation resistance of a stainless steel.* Oxidation of Metals, 1983. **19**(1): p. 1-18.
159. Mazandarany, F. and R. Pehlke, *Thermodynamic properties of solid alloys of chromium with nickel and iron.* Metallurgical Transactions, 1973. **4**(9): p. 2067-2076.